

AIRBORNE SYNTHETIC APERTURE RADAR IMAGES OF
AN UPWELLING FILAMENT

A THESIS SUBMITTED TO THE GRADUATE DIVISION OF THE
UNIVERSITY OF HAWAII IN PARTIAL FULFILLMENT OF THE
REQUIREMENTS FOR THE DEGREE OF

MASTER OF SCIENCE
IN
OCEANOGRAPHY
DECEMBER 2003

By

David L. Johnson

Thesis Committee:


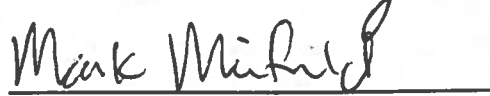
Pierre Flament, Chairperson
Eric Firing
Mark Merrifield

© Copyright
by
David L. Johnson

We certify that we have read this thesis and that, in our opinion, it is satisfactory in scope and quality as a thesis for the degree of Master of Science in Oceanography.

THESIS COMMITTEE


Chairperson

ACKNOWLEDGMENTS

I would like to thank my committee for their support and their significant scientific input, and my adviser in particular, as the results of this work reflect to a great extent his design for the SAR investigation.

ABSTRACT

The Cape Mendicino upwelling filament was imaged in 1989 using the NASA/JPL AIRSAR multiband Synthetic Aperture Radar (SAR) and NOAA AVHRR thermal and optical radiometry. To first order, SAR images of the ocean are solely dependent on the surface wave field, but they ultimately reflect the synergy of a vast number of geophysical processes. The complexity of surface wave processes leaves a large gap between the information contained in SAR images, and our ability to describe them without conjectures. Investigated here are features associated with thermal fronts, vortices, geostrophic jets, and internal waves. SAR spectra suggest infragravity waves aligned with the wind swell. Cross jet SAR profiles were investigated in detail; comparison with results from a simple model suggest that some processes not included in the simulation are dominating in physical environment. Band dependent asymmetry of the profiles is consistent with convergence and accumulation of surfactants; band independent location of the peaks suggests that such convergence may be a jet driven process. The band independent position of humps in the profiles suggests critical reflection of strongly imaged intermediate ($\lambda > \lambda_{\text{Bragg}}$) waves or alternately a persistent and complex jet velocity profile. Apparently anomalously high damping of longer Bragg waves at some jet orientations is inconsistent with historical measurements of the modulus of elasticity of ocean surfactants and might indicate the hyperconcentration of surfactants within a zone of strong convergence. Net changes in radar cross-section across some sections of the jet could indicate a number a wave or current processes, which are discussed.

TABLE OF CONTENTS

Acknowledgments	iii
Abstract	iv
Chapter 1 Introduction	1
Chapter 2 Principles of SAR Ocean Imaging	5
Chapter 3 Data and Processing	14
Chapter 4 AVHRR Images	21
Chapter 5 AIRSAR Images and Derivatives	32
5.1 Southern and Near-shore Regions	33
5.2 Filament Core, Hammerhead Front, and Northern Branch	34
5.3 Southern Filament Branch	37
5.4 Jet Profiles	40
5.5 Long Gravity Wave Spectra	45
Chapter 6 Discussion: Inferring Jet Structure from Multi-band SAR Profiles	94
Chapter 7 Conclusions	96
Appendix A A Numerical Simulation of Jet Induced Wave Field Modulation and the Predicted SAR Signature	99
Appendix B Subresolution Inferences	119
References	122

CHAPTER 1

INTRODUCTION

In September of 1989 a multiband synthetic aperture radar (SAR) survey of an upwelling filament visible in AVHRR thermal images near Cape Mendicino, California was conducted using the JPL C (5.28 GHz), L (1.20 GHz), and P (0.44 GHz) band instrument AIRSAR, onboard the NASA DC-8 platform. The layout of the survey is shown in figure 1; there is a 38 hour time lag between this AVHRR image and the SAR images, the surface being obscured by clouds at the time of SAR imaging. The filament is horn shaped, and incorporates a mesoscale dipole, with vortices of ~50 km diameter. A second filament is seen to the south near Point Arena, and a mesoscale anticyclone of ~200 km diameter lies between them. Small scale O(km) structures are ubiquitous.

Radar images illuminate structures which modulate the surface wave spectrum. The dominant processes are hydrodynamic modulation within spatially varying currents, which appear as positively modulated (bright) and negatively modulated (dark) features, and wave damping by surfactants, which appear only as dark features. An overview of the theory of SAR imaging of ocean processes is presented in chapter 2.

The phenomenon of Ekman-driven upwelling occurring from late spring to early fall is well understood. The enhanced coupling of the atmosphere above the inversion to the ocean during the upwelling season is explained by the model of Beardsley et al. (1987). In this model, seasonally intensified cycles of diurnal heating and cooling over the coast

drive cross-shore flow, forcing entrainment of high momentum offshore winds into the North Pacific Sub-tropical High subsidence depressed inversion. This entrainment erodes and further depresses the inversion near the coast, resulting in a tilted inversion and a southward atmospheric geostrophic jet. Turbulence generated by the shear mixes and destratifies the marine layer, allowing momentum to be transferred to the ocean surface. The induced Ekman currents are constrained by the boundary condition of the coast, leading to upwelling of cold high salinity waters, and sharp temperature, salinity, and density fronts inducing geostrophic jets (Huyer 1984).

A combination of orographic wind variations (Winant et al. 1988; Ramp et al. 1991; Abbot and Barksdale 1991), topographic boundary conditions (Haidvogel et al. 1991), undulating instabilities of jets (Pierce et al. 1991; and Allen et al. 1991), and advection within the vortex field (the vortex field itself resulting from the first three processes) (Strub, 1991), results in mesoscale filaments visible at $O(10 \text{ km})$ resolution. These filaments extend $O(400 \text{ km})$ into the ocean, have a typical along-coast spacing of $O(200 \text{ km})$, (see the CZCS chlorophyll image, figure 17 of Strub et al. 1991).

The use of ~ 10 meter resolution SAR images (presented in chapter 5) allows the investigation of ocean structures at a scale two orders of magnitude smaller than that possible using AVHRR images (presented in chapter 4), but the difference in imaging mechanisms (e. g. Bragg scattering and Doppler imaging versus e. g. blackbody emission and ray-path imaging) means that the SAR-illuminated structures will not simply be zoomed versions of the structures seen through the AVHRR. SAR imaging of the ocean is complex, due: (1) to the strong synergy of atmospheric and oceanic processes,

(2) to the dependence of an image on the SAR platform velocity (both speed and direction) with respect to geophysical structures, and (3) to the ambiguous nature of Doppler imaging a moving surface.

Airborne SAR images such as AIRSAR differ from satellite SAR images. AIRSAR exhibits less stability in signal than e. g. ERS-1 SAR due to the electrically noisier environment of the aircraft, and uncontrolled flight motions. The lower altitude implies a wider range of incidence angles which, while giving a wide band of surface spectral information, implies a changing relationship between image and geophysics across an image, potentially complicating interpretations.

An analysis of the images from the 1989 AIRSAR survey was carried out with the goal of detecting any significant geophysical signals; many of the images are very complex and most features elude detailed geophysical description. The southern branch of the filament contains a suspected geostrophic jet; the multi-spectral cross-front characteristics of this linear structure are described and compared to results from a simple numerical model in section 5.4. Long gravity wave spectra inferred from the SAR images are presented in section 5.5.

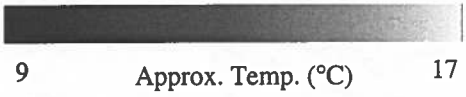


Figure 1. SAR image locations with respect to the last AVHRR thermal image of the survey region not significantly obscured by clouds (AVHRR channel 4 at JD 251, GMT 03:22 / AIRSAR SAR L band at JD 251, GMT 16:47-19:08), the line represents the aircraft track.

CHAPTER 2

PRINCIPLES OF SAR OCEAN IMAGING

Synthetic Aperture Radar imaging utilizes a moving platform where delay time, Δt , between the transmitted and reflected component of a signal gives the slant range distance of the corresponding scatterer,

$$d_{slant} = \frac{c \Delta t}{2} \quad (1)$$

and the Doppler shift between the transmitted and reflected component of a signal gives the azimuthal angle of the corresponding scatterer,

$$\sin \theta = \frac{\Delta f}{2 \frac{v_{platform}}{c} f_{radar}} \quad (2)$$

where f_{radar} is the frequency of the radar, Δf is the Doppler shift in the reflected signal, and $v_{platform}$ is the velocity of the platform; the imaging geometry is shown in figure 2. Equation 2 assumes a frozen surface. The non-static nature of the ocean surface creates at once an imaging mechanism and distortions in SAR images.

The term "Synthetic Aperture" derives from the geometrical similarity between the azimuthal resolution obtained by coherently integrating multiple pulses produced along a flight path and that obtained by using a real aperture radar with a real aperture (antenna) of length equal to the flight path. The nominal azimuthal angular resolution is given by

$$\delta\theta = \lambda/D \quad (3)$$

where D is the integration path length. The nominal range resolution

$$\delta r = c/2b \quad (4)$$

is determined by the signal bandwidth, b , of the instrument, where c is the speed of light.

For angles of incidence greater than $\sim 15^\circ$ the dominant scattering mechanism for microwave radiation from the surface of the ocean is Bragg scattering (away from zones of breaking, where specular, i. e. mirror-like, scattering can dominate), as illustrated in figure 2 of Hasselmann et al. (1985).¹

The condition for resonance is that return signals from individual scattering elements be in phase. From simple geometry, the Bragg wavelength, or surface wavelength for which the resonance condition holds, is

$$\lambda_{Bragg} = \frac{n \lambda_{radar}}{2 \sin \theta_{incidence}} \quad (5)$$

where $n=1,2,3,\dots$

The general assumption that first order ($n=1$) Bragg scattering dominates, and the contribution of higher order ($n>1$) Bragg components is negligible, may not always be valid. The typical surface wave field, roughly described by the Phillips (1958) saturation spectrum of $E \propto \omega^{-5}$, is apparently not sufficiently red for the higher order components to significantly contribute under most conditions. However, under conditions of extreme wave modulation where the spectrum is expected to deviate strongly from the Phillips spectrum, the dominance of first order scattering may give way to a more complex

¹ Bragg scattering is resonant scattering from a lattice of individual scattering elements, and is named after the discoverer of the principle in the context of x-ray scattering from a crystal lattice.

situation requiring consideration of the longer Bragg waves. Higher order Bragg scattering would be important when the current field is intense enough to exclude the lowest order Bragg components; the jets under investigation here may meet the conditions for critical reflection at the relevant wavelengths (equation A7).

At the associated Bragg wavelengths and imaging resolutions of most SAR instruments, the ocean is described by a fluctuating broad band spectrum (Hasselmann et al. 1985) where the phases of a given wavenumber component of the spectrum are uncorrelated at the scale of the radar imaging resolution, and correlated at the scale of order the wavelength. Hence, speckle in SAR images of the ocean results from the statistical fluctuation of the relative phases of scattering elements (wave groups with a high Bragg return) in the coherently integrated surface patch. It seems reasonable that this view should hold for our C band images, where there is two orders of magnitude difference between the Bragg wavelength and the imaging resolution scale, but for P band, where the corresponding difference is only one order of magnitude, its validity may be questioned.

To reduce speckle noise, multi-look images are created from the single look images. In the case of a 4-look image, a 2×2 pixel average is made. In the case of a 16-look image, a 4×4 pixel average is made. The AIRSAR SAR data used are 4-look and 16-look.

Because of the Doppler component of the SAR imaging mechanism described by equation 2, any process causing the velocity component of a scatterer in the range direction to vary in space, will cause an azimuthal displacement of the scatterer in the

image. For a propagating wave the Doppler shift is determined by the phase velocity. Quantitatively, motions with a component of their velocity, $v_{surface}$, in the range direction produce the azimuthal displacement

$$d_{azimuth} = d_{range} \sin (\Delta \theta_{azimuth}) \quad (6)$$

\Rightarrow

$$d_{azimuth} = d_{range} \frac{\Delta f_{Doppler} \lambda_{radar}}{2 v_{platform}} \quad (7)$$

The Doppler shift is given by

$$\Delta f_{Doppler} = 2 \frac{v_{surface} \sin \theta}{c} f_o \quad (8)$$

So,

$$d_{azimuth} = d_{range} \left(2 \frac{v_{surface} \sin \theta}{c} f_o \right) \frac{\lambda_{radar}}{2 v_{platform}} \quad (9)$$

Since $f_o = c/\lambda_{radar}$ we get the band independent azimuthal displacement of

$$d_{azimuth} = d_{range} \frac{v_{surface}}{v_{platform}} \sin \theta \quad (10)$$

A description of the relationship between geophysical processes and radar cross-section can be made through a modulation transfer function, or MTF, with four distinct components

$$MTF = MTF_{RAR} + MTF_v \quad (11)$$

$$MTF = (MTF_h + MTF_t + MTF_{rb}) + MTF_v \quad (12)$$

MTF_v represents velocity modulation by geophysical processes that give rise to a spatial variation in surface velocity. MTF_{RAR} represents the real aperture radar modulation

transfer function which is described by three distinct components. MTF_h represents hydrodynamic modulation by geophysical processes which affect the amplitude, wavelength, angle, or phase of the surface wave field, specifically at the Bragg wavelengths. MTF_t represents tilt modulation by geophysical processes which significantly change the surface angle from the horizontal so as to change the component of the surface spectrum which corresponds to the Bragg wavelength. MTF_{rb} represents the range bunching modulation by geophysical processes which significantly displace the surface as to change the range distance. It is this type of distortion that produces the foreshortening in SAR images of mountains.

The classes of theory relevant to MTF_h include those describing wave/wave and wave/current interaction, ocean/atmosphere interaction, wave breaking, turbulence generation and its effects on wave dissipation at the $O(\lambda_{Bragg})$ scale, microlayer generation/destruction and the effect of slicks on wave dissipation.

Oceanic structures, such as geostrophic jets, convergent fronts, plume fronts and internal waves, modulate the surface wave spectrum through mechanical (wave and current) energy conserving processes described through MTF_h . These structures can give rise to significant velocity gradients and/or surface tilt, and so contribute to MTF_{rb} , MTF_t and MTF_v as well. Such structures are imaged through both positive and negative modulation of the wave field.

The imaging of long gravity waves (swell) involves all four components of the MTF; the spectra inferred from such images can contain artifacts which arise from the

competing effects of the different imaging mechanisms (Melcheimer et al. 1998) for an example involving a radar band dependent phase change in MTF_{RAR} associated with the change in sign of $[c_g - u^*]$.

Surface turbulence generating processes lead to spectral dissipation (wavenumber dependent damping) of the surface wave spectrum and include wave breaking, rain drop splash products (which are most significant for larger drop size), and supercritical current shears. The modulation (through MTF_h) produced by these processes is always negative.

The presence of slicks of organic molecules, from oceanic or terrestrial biologic activity, or natural or anthropogenic oil seeps, will be imaged as regions of reduced surface wave spectral energy density.

Lucassen (1982) considered wave damping due to surfactants to be a process dominated by the readjustment of the subsurface flow field under capillary-gravity waves by the new constraint on the motion of the one molecule thick surface layer. Surface layers composed of surfactants (a molecule with hydrophilic and hydrophobic ends) are unlike those of a clean surface in that they support longitudinal surface waves. The resulting altered subsurface flow gives rise to significant viscous losses and hence wave damping. The important parameter for description of the longitudinal surface waves is the surface dilational modulus

$$\epsilon \equiv \frac{\partial \sigma}{\partial \ln(A)} = A \frac{\partial \sigma}{\partial A} \quad (13)$$

where σ is the surface tension and A is the area of a surface element. His results predict

even higher values of damping coefficient β/β_0 for long waves than for short waves, albeit at larger values of epsilon. Thus, the common suggestion that reduction in SAR P band cross-section is due to a secondary effect of the damping of short waves may not always be warranted.

The sources of surfactants are natural petroleum seeps, biogenic processes, which are expected to be closely related to the quantity of primary production and thus also expected to be high within the study region during the upwelling season, and anthropogenic introduction of petroleum or petroleum based oils, again high wherever there is abundant industrial shipping and manufacture, as there is in California.

The modulus of elasticity (ϵ) for a clean water surface is theoretically zero (distilled water measured at less than 0.2 mN m^{-1} by Frew and Nelson 1992). Adding a sufficient amount of organic molecules to the surface to form a one molecule thick layer gives a surface which resists expansion and contraction. In the presence of a microlayer, energy is lost from the surface wave spectrum toward molecular and thermal energy. Typical values in the literature (e. g. Frew and Nelson 1992; Wei and Wu 1992; Mass and Milgram 1998) for ϵ for natural and synthesized slicks are between 10 and 80 mN m^{-1} .

In practice the four components of the MTF are not always distinguishable and thus SAR images nearly always contain ambiguity, this is particularly true for images of surface structures with high anomalous velocities with large range components, and thus significant contribution from MTF. The ambiguity potentially can be reduced by comparing multiple SAR bands (spectrally) or by looking at the same region imaged

from different flight paths (directionally).

As longer waves are affected by deeper geophysical processes, one can view each image in C , L, and P bands, respectively, as looking progressively deeper into the ocean surface. C band sees the very surface and is most likely to be affected by slicks, P band sees the deeper layers including internal waves through direct modulation of the Bragg component, and L band sees a regime in-between. Because of the wide range of look angle ($\sim 17^\circ$ to $\sim 70^\circ$) of the AIRSAR instrument there is some overlap in λ_{Bragg} between bands.

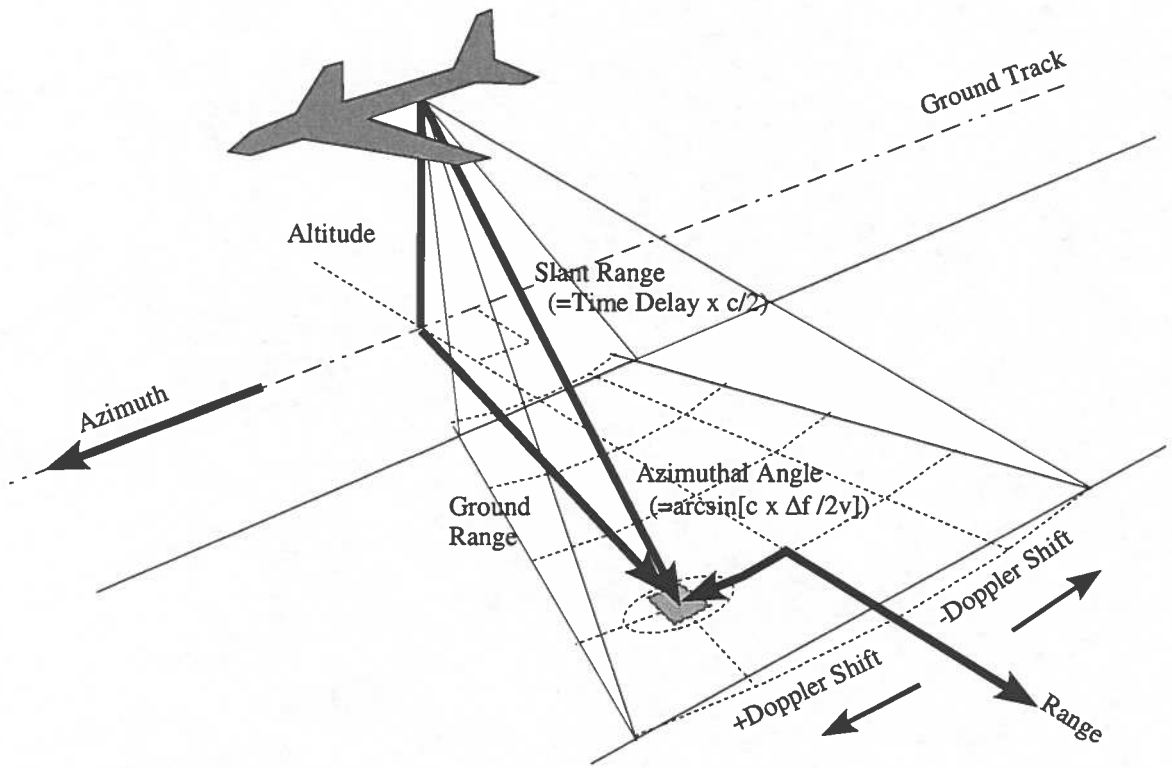


Figure 2. SAR imaging geometry.

CHAPTER 3

DATA AND PROCESSING

This investigation focused on the interpretation of NASA/JPL AIRSAR multi-band SAR images and NOAA AVHRR images. In addition, NOAA buoys provided synoptic measurements of surface wind, sea surface temperature (SST), surface salinity, and non-directional wave spectra; the locations of the NOAA buoys used in this investigation are indicated in figure 3.

AVHRR is a 5 channel passive radiometer mounted on the NOAA polar orbiting satellites, with an attitude dependent spatial resolution of approximately 1 kilometer. AVHRR channel 1 (0.5-0.7 μm) images in the visible, channel 2 (0.7-1.1 μm) in the visible and near infrared, channels 3 (3.5-3.9 μm), 4 (10.3-11.3 μm), and 5 (11.5-12.5 μm) in the thermal infrared.

The AVHRR images used in this investigation were processed using Terascan software. They were first registered (transformed to a Mercator grid) using bilinear interpolation, which avoids the introduction of artifacts that show up in the first spatial derivative of AVHRR images registered using nearest neighbor interpolation.

Images of the first and second spatial derivatives of AVHRR channel 4 were created. Granting that the salinity field and variations in hydrography prevent a quantitative interpretation, images of the first spatial derivative (roughly the surface temperature gradient) are useful for locating the most intense thermal fronts and thus likely positions

of geostrophic jets.

The NASA AIRSAR instrument can image synchronously at three radar wavelengths, C (5.670 cm), L (24.226 cm), and P (70.127 cm) bands, and can operate in HH (horizontal transmit-horizontal receive), VV (vertical transmit-vertical receive), and HV \leftrightarrow VH (cross) polarization. This investigation utilized full multi-band HH polarization data. VV polarization has a less incident angle dependent scattering cross-section (for angles less than $\sim 80^\circ$), but the scattering cross-section for HH polarization is nearly-linear with surface wave amplitude for all wave amplitudes down to a perfectly flat surface, in contrast to VV polarization which experiences a dramatic falloff as wave amplitude falls below the radar wavelength.² Thus, in the interest of being able to quantitatively compare surface wave amplitudes (not attempted here because of the wide incidence angle and low instrument stability), HH polarization is traditionally used for ocean imaging. An additional advantage of HH in this case is that the AIRSAR antennae have a more vertically focused beam (a cardioid vs. unfocused) in HH than in VV, reducing the reflected signal from the ocean surface on the opposite side of the aircraft which could give rise to ghosts (essentially a weaker superimposed mirrored image of the swath on the other side) in the SAR image.

The AIRSAR data were taken from an altitude of ~ 8200 m, with a near slant range of 8664 m, giving a near ground range of ~ 2550 m, and a minimum incidence angle of $\sim 17^\circ$. The raw AIRSAR images, as pre-processed by JPL, were in slant range coordinates. To

² This can be seen as a result of horizontally polarized radiation having a continuous scattering element determined by the crest length, which is relatively independent of amplitude, whereas vertically polarized radiation has a scattering element determined by the crest height.

obtain an image in ground range coordinates, a nearest neighbor transformation was applied in the regridding.

Two types of image product were used in this investigation, 4-look images (the images of narrower swath oriented at 128° SE along the southern edge of the Cape Mendicino filament) and 16-look images, of 6.05 m and 12.10 m along track pixel spacing, respectively. The number of looks corresponds to the number of single coherent integrations of signal (single-look images) averaged incoherently in preprocessing to produce a single image. Averaging 16 looks produces images with a pixel resolution of twice the spatial dimension as images averaging 4 looks, but with reduced speckle noise. Because of the wide range of the incident angle for the instrument, and resultant variation in mean backscatter intensity as a function of angle, the images were renormalized to the azimuthal average for a given ground slant range.

Given the fixed near range, the swath width and maximum incidence angle depends on the number of slant range pixels (1280) and pixel range resolution (3.33 m and 6.66 m for 4 and 16 look images, respectively). Thus the 4 look image swath width is ~ 10.4 km and the 16 look image swath width is ~ 14.6 km, giving maximum incidence angles of 52° and 61° , respectively. A plot of Bragg wavelengths for the AIRSAR radar wavelengths and range of incidence angles for this investigation is shown in figure 4.

For the AIRSAR instrument, 1500 pulses are coherently integrated over 2 seconds to form a single look image. The speed of the DC-8 aircraft is ~ 200 m/s, so $D \approx 400$ m. From equation 3 this gives an angular resolution of 0.008° , 0.035° , and 0.100° , for C, L,

and P bands, respectively. At a slant range distance of 8700 m this corresponds to azimuthal resolutions of ~1.2, ~5.3, and ~15.2 m. A pulse bandwidth of 20 MHz, for all bands, gives, from equation 4, a nominal range resolution of $\delta r = 7.5$ m.

The azimuthal pixel length of the data for a single look AIRSAR image is 3 meters, so a single look image in P band would contain four pixel lengths of azimuthal smearing, L band has an azimuthal resolution approximately equal to the pixel resolution, and C band integrates only a third of the azimuthal distance represented by each pixel. Single look images for all three bands incorporate a 5 pixel range smearing.

The distance that a crest of a gravity wave will propagate in time t is given by $d = c_{\text{phase}}t = \sqrt{[g/k]}t$. For the two seconds of integration time for the AIRSAR instrument this results in a smearing of 50 m for a 400 m wave, 25 m for a 100 m wave, and the wavelength of the smallest wave which can be imaged (i. e. where $d = \lambda$) is given by $\lambda_{\text{min}} = (g/2\pi)t^2 = 6.24$ m for a single look image, about twice the single look resolution and nearly equal to the 4-look resolution. Thus, a minimum imaged wavelength will not be seen in 4-look and 16-look images, but smearing will exist in images of the longer waves.

Because speckle noise is approximately 1 dB in the raw 4-look images, a filter was applied such that each pixel in the filtered image represents the unweighted average of the 9 pixel neighborhood of the 3X3 box around the pixel at that location. The speckle noise is thus reduced to 0.3 dB. A further reduction to 0.2 dB can be made by applying a filter employing a 5X5 box average. This was not done, however, because we approach

the scale of the swell and other features which we hope to resolve, and the trade-off between reduced speckle noise, and reduced resolution reaches a point of diminishing returns.

Comparisons of both land features and ships imaged in all three bands suggest that there exists a +1 pixel range bias in the 16-look P band images, in other words, the P band 16-look images are positively shifted 12 meters in the range direction relative to C and L bands. Lack of similar references for the 4-look images prevents a direct check of bias in that image product, it seems prudent to assume a bias of similar spatial dimension, thus a possible +2 pixel range bias is assumed in our 4-look P band images.

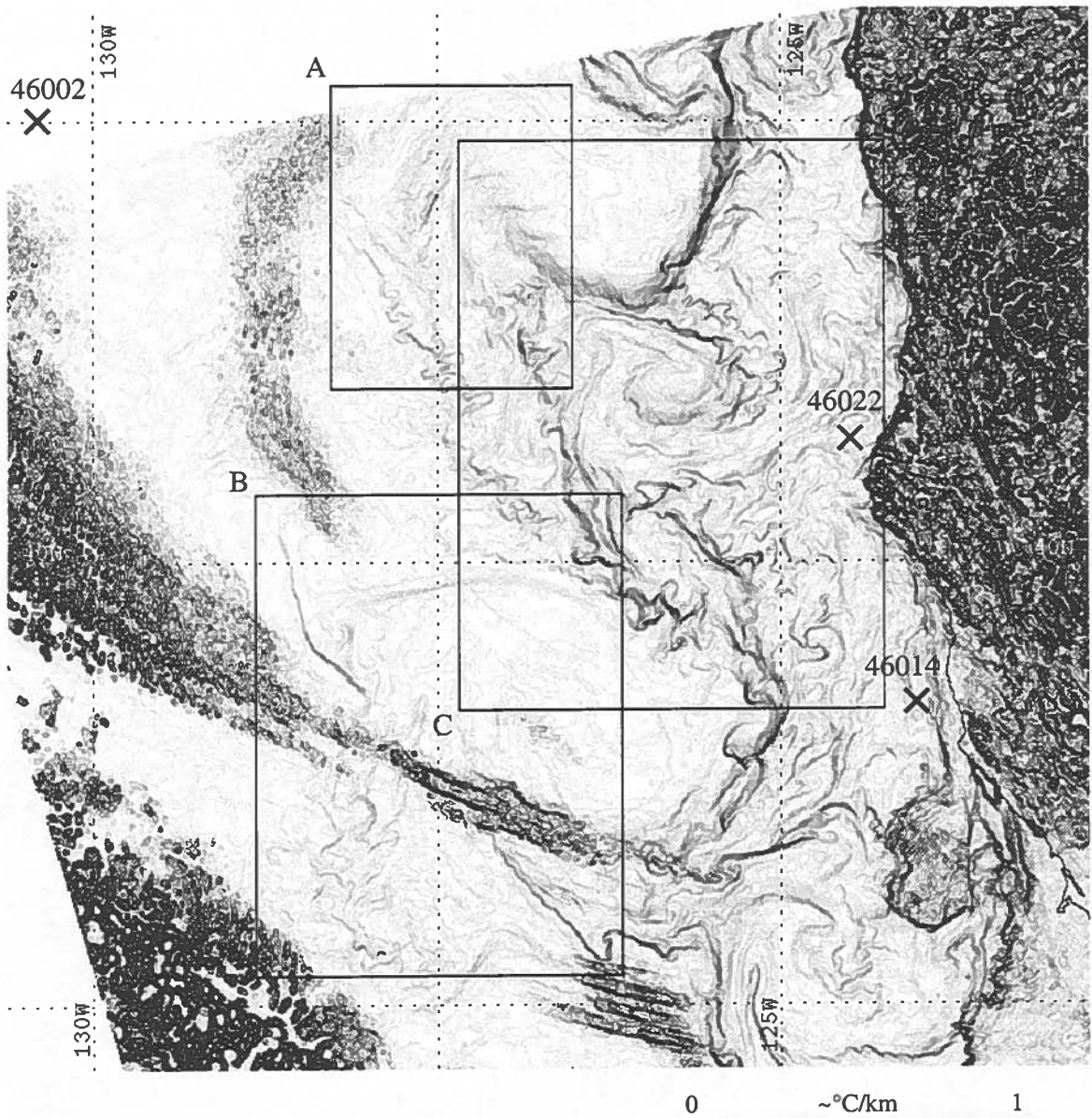


Figure 3. Spatial gradient of AVHRR channel 4 at JD 250 03:36. Detail of regions A, B and C shown in figures 9, 10, and 11, respectively. X's show NOAA buoy locations.

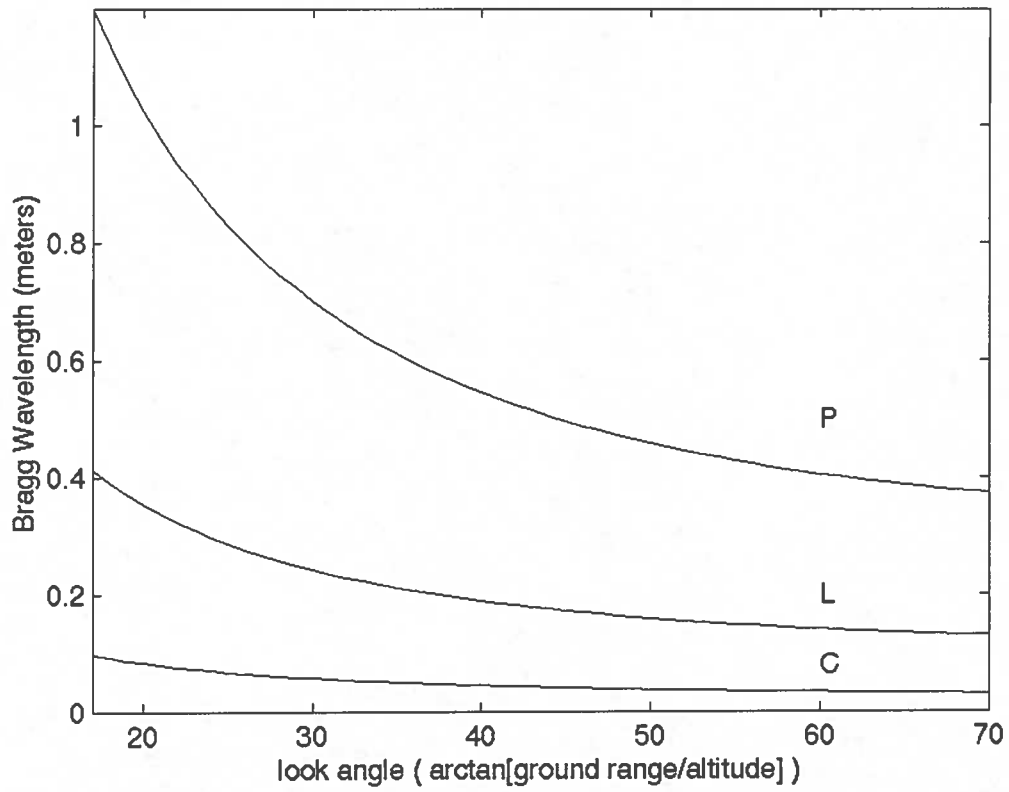


Figure 4. Bragg wavelengths for the three AIRSAR bands scattering from a level surface over the range of angles relevant to our data.

CHAPTER 4

AVHRR IMAGES

The historical correlation between filaments and the geographic features of Cape Mendicino and Point Arena is high, examples being October 1978 (Fu and Holt 1982, page 75), June 1981 (Korso and Huyer 1986, figure 1), May-July 1987 (Strub et al. 1991, figures 2, 4, and 5), and the July's of 1981 through 1986 (Strub et al. 1991, figure 15). Furthermore, Winant et al. (1988) showed that Cape Mendicino, along with Point Arena represent orographic boundary conditions capable of producing supercritical flow in the atmosphere; atmospheric flow transitions from laminar to turbulent flow and the associated change in Ekman coupling is expected to give rise to along-coast variations in transport and thus nonuniform cross-shore transport (i.e. filaments). Apparent atmospheric hydraulic jumps are visible via marine stratus at Point Conception JD 247, GMT00:06 and at Cape Mendicino JD 247, GMT 21:49 and JD 248, GMT 21:39 (figure 5). Winds aloft, as indicated by cloud motion from finer time scale AVHRR series, were northerly, consistent with historical mean surface winds.

The horn-shaped filaments and dipole seen in the images from the time of our survey are consistent with the simulations of Haidvogel et al. (1991). The significance of this consistency must be questioned though; the dipole within the Cape Mendicino filament appears to be unusual and was not apparent in any of the reviewed historical images. The 1987 Point Arena filament is very similar, sharing the horn-shaped structure of the 1989

Point Arena filament, but it was the only other example found.

Wind and sea surface temperature (SST) data from the three NOAA buoys used in this investigation are shown in figure 6. During the period preceding the SAR survey the far offshore wind field was northerly and never exceeded 10 m/s, the near-shore region experienced highly variable winds which were mean northerly and never exceeded 15 m/s; thus the inferred sign of the curl was variable but of positive mean, indicating upwelling conditions, both coastal and possibly distributed. SST at the locations of the near-shore buoys displays significant variation relative to the SST at the location of the deep-water buoy, where a $\sim 1/4^{\circ}\text{C}$ diurnal cycle is discernible. This contrast reflects both the greater vertical (buoyant) stability offshore and greater horizontal SST variation near-shore. Slack wind associated warming events at the near-shore buoys may indicate reduced wind driven vertical mixing, but much of the near-shore variation is likely due to horizontal advection, which would not be visible in the offshore temperature signal.

AVHRR visible and thermal images from JD 247, GMT 00:06 are shown in figure 7. The correlation between structures imaged in both wavelength regimes suggests associated physical processes. The boundary of the thermally imaged dipole and cyclone are outlined by positive modulation in the optical. Note that the horn-shaped part of the filament and regions of coastal upwelling also display an optical signal. Several processes could be responsible for this signal: (1) generation of marine stratus above an area of lower SST and thus lower dew point; (2) enhanced subsurface primary production due to dynamic front induced mixing and removal of a limiting nutrient condition (as well as the bringing of nutrient rich water to the photosphere); (3) sunglint due to wave modulation

by geostrophic jets; (4) sunglint due to wave damping in a region of enhanced surfactant accumulation caused by convergence and/or enhanced primary production. Based on solar and satellite look angles, mechanisms (3) and (4) would require the slope spectrum to be enhanced at $\sim 6^\circ$, tilted downward to the west. The lack of this signal at other times weighs against hypothesis 2.

Asymmetry of filaments was first noted by Flament et al. 1985; AVHRR thermal images often show sharper temperature fronts on the cyclonic than on the anticyclonic edge (see the series of images from July of each year from 1981 through 1986 shown in figure 15 of Strub et al. 1991). Flament et al. (1985) found, using tow-yo sections, that the sharp temperature front at the cyclonic boundary of a filament was salinity compensated and was not a sharp density front. Density gradients at anticyclonic fronts imply geostrophic shear. Shear instability may enhance mixing, weakening the temperature gradient at the anticyclonic fronts, relative to the cyclonic fronts, thus giving rise to the asymmetry. At the time of the AIRSAR survey the Cape Mendicino filament does not exhibit this classic structure to as great a degree as the Point Arena filament, and in all cases the occurrence corresponds to the horn-shaped parts (sharp temperature fronts indicated by arrows in figure 8).

Salinity compensation may provide an additional mechanism for the growth of filaments. Considering a straight filament, salinity compensation and reduced transport occur on the southern side, where the transport is shore-ward, but not on the northern side, where the transport is away from the coast. The resulting cross-shore transport

imbalance means that even in the absence of other forcings, the filament will grow. This mechanism requires the presence of N→S salinity gradients, consistent with the mean salinity field of the eastern North Pacific. Strong salinity fronts might be expected to form channels through which filaments should extend. One could take this further and ask if the most rapidly growing filaments should be those whose southern fronts are detectably overcompensated.

The tip of the Cape Mendicino filament ends in streamers (figure 9), possibly emanating from instabilities propagating along the north side of the filament. The streamers propagate NNW at ~0.5 m/s toward and around the tip, where they become indistinct. There is no discernible extension of the actual tip of the filament over the ~10 days of clear view inspected.

Cyclones dominate the visible small scale vortex field (figures 8-11), and a train of cyclonic vortices suggestive of instabilities is present on the sharp cyclonic front toward the tip of the Cape Mendicino filament (figure 9); these vortices are propagating at ~0.2 m/s. Well developed visible small scale vortices are rare, the best example of which is shown in figure 10. No examples of vortex merger were observed.

The SAR survey was concentrated primarily about the region of the dipole, the associated hammerhead front, and the southern branch of the Cape Mendicino filament; this region is shown in detail in figure 11. Note that the northern branch of the filament ends in a secondary hammerhead for which the associated cyclone is never observed in highly developed state.

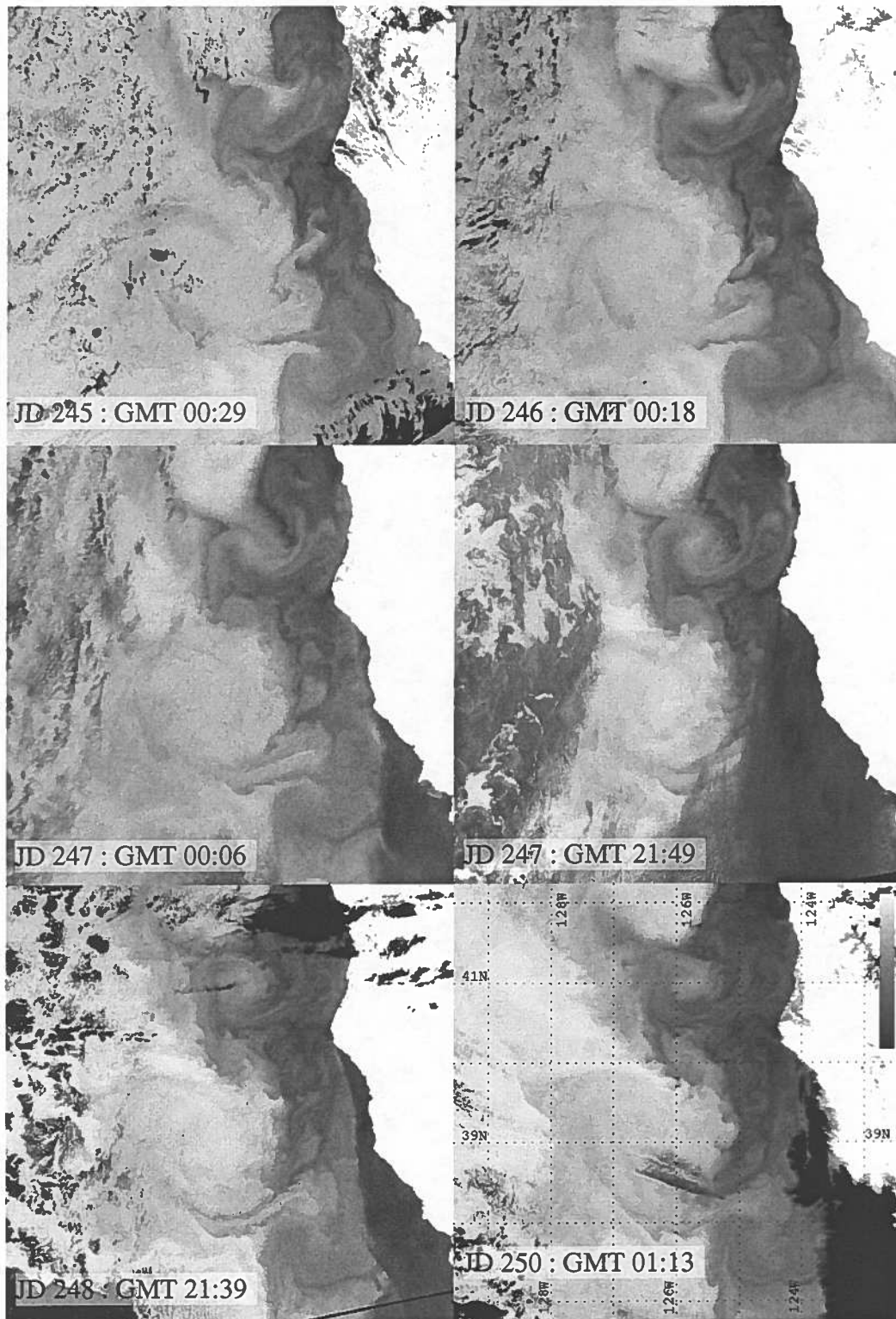


Figure 5. Time series of AVHRR channel 4 images.

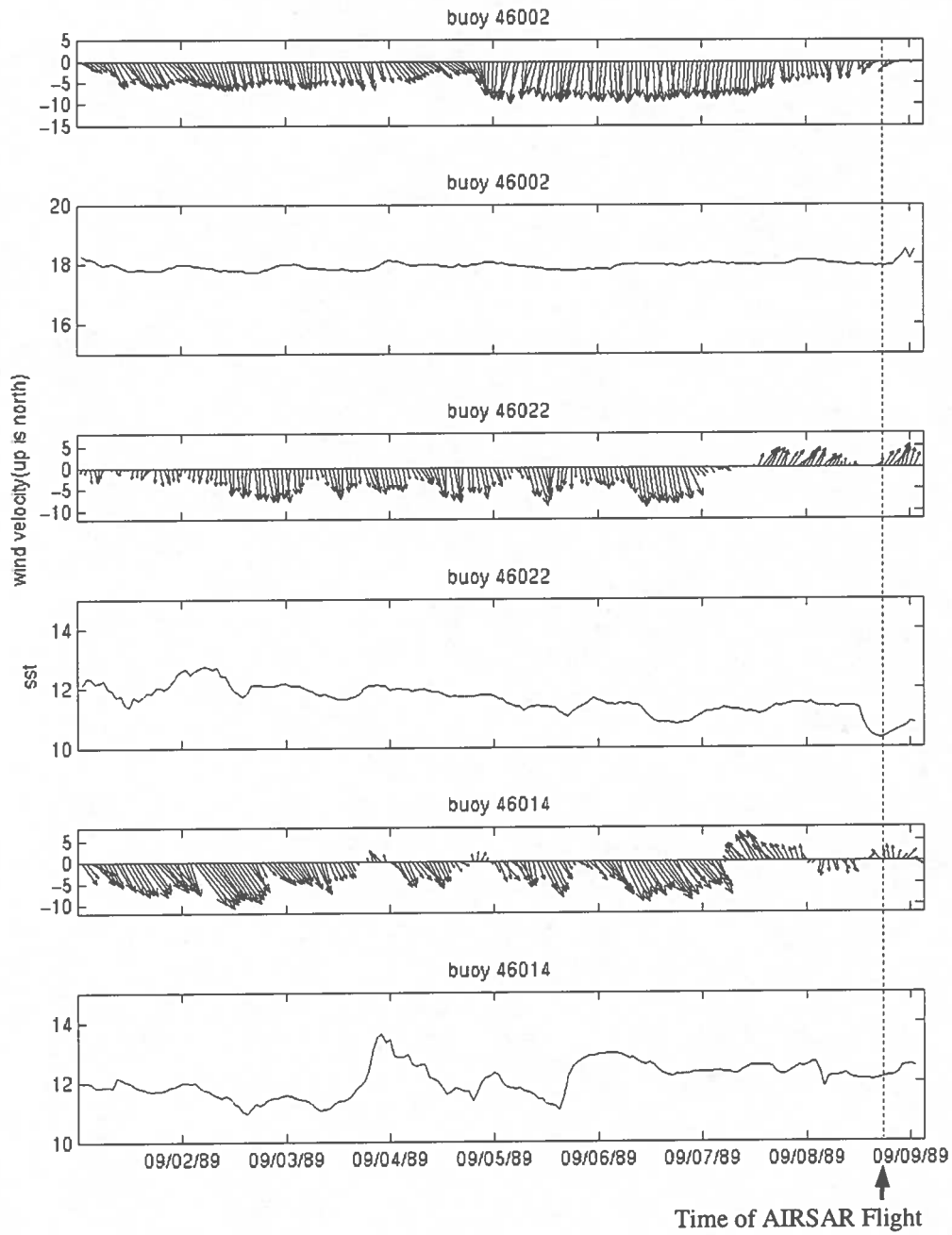


Figure 6. Wind speed and direction (up is north) and SST from JD 244 through JD 251 at NOAA buoys 46002, 46022, and 46014.

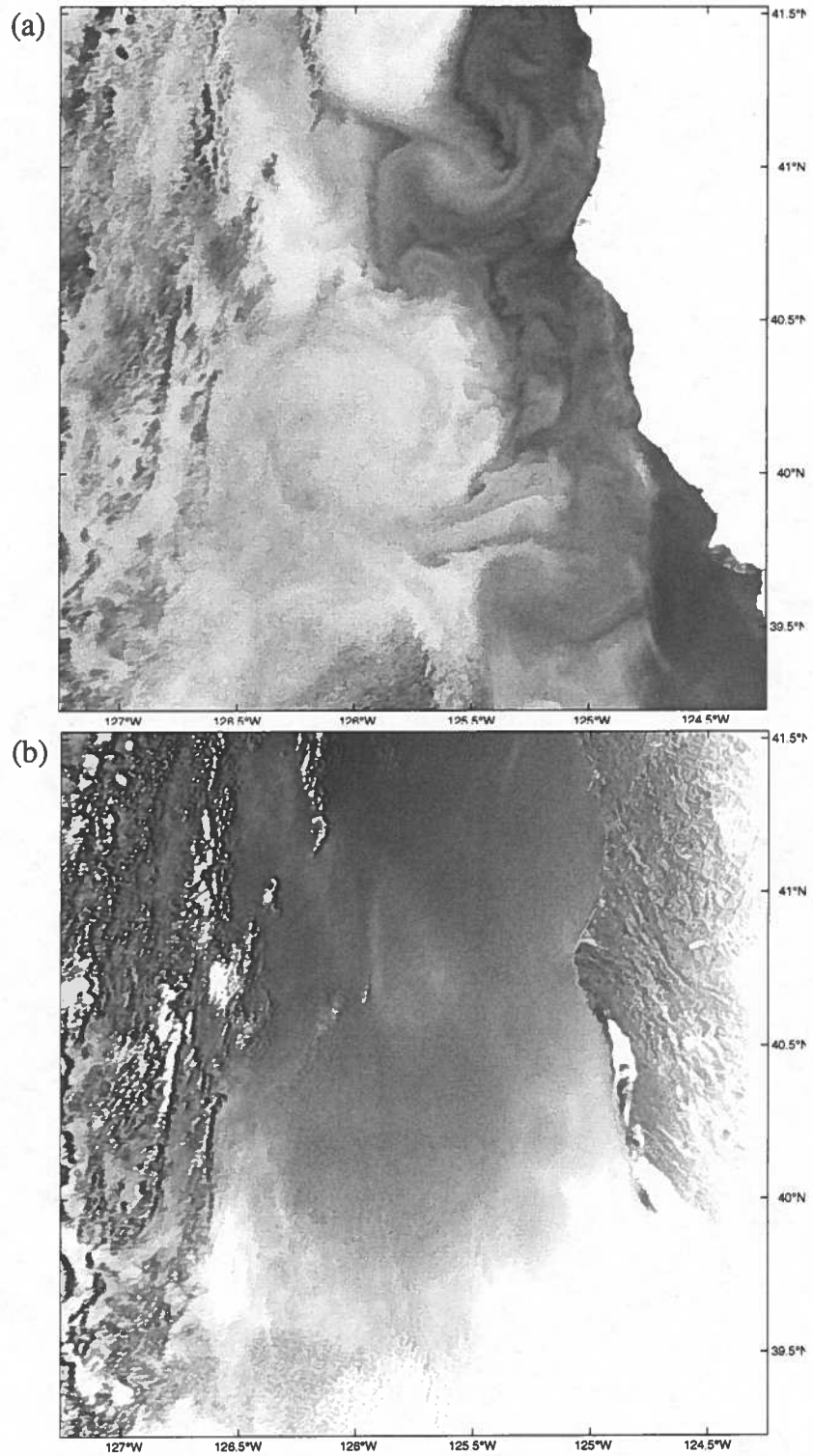


Figure 7. Visible and Near-IR signal at JD 247 GMT 00:06: (a) AVHRR channel 4 (b) AVHRR channels 1 and 2 average (channels 1 and 2 were nearly identical; the average is shown to maximize signal-to-noise). The image has been linearly detrended to remove the solar/nadir angle dependent mean reflectivity.

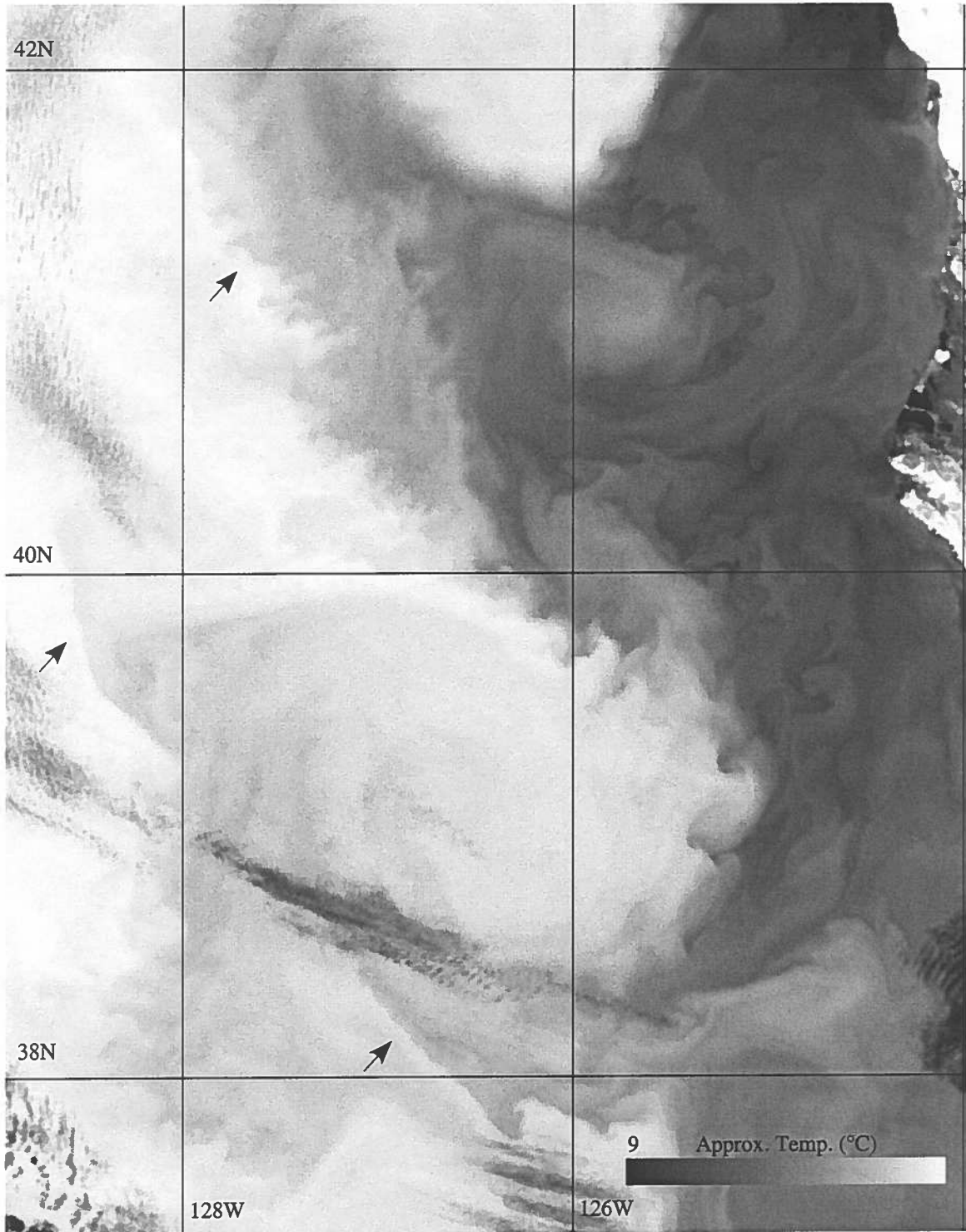


Figure 8. AVHRR channel 4 at JD 250, GMT 03:22, approximately 38 hours before the SAR flight. The arrows indicate where the filaments exhibit classical asymmetry.



Figure 9. Detail of region A (see figure 3), AVHRR channel 4 at JD 250, GMT 13:36. The apparent instability train indicated by the arrow is moving SSE at ~ 0.2 m/s.

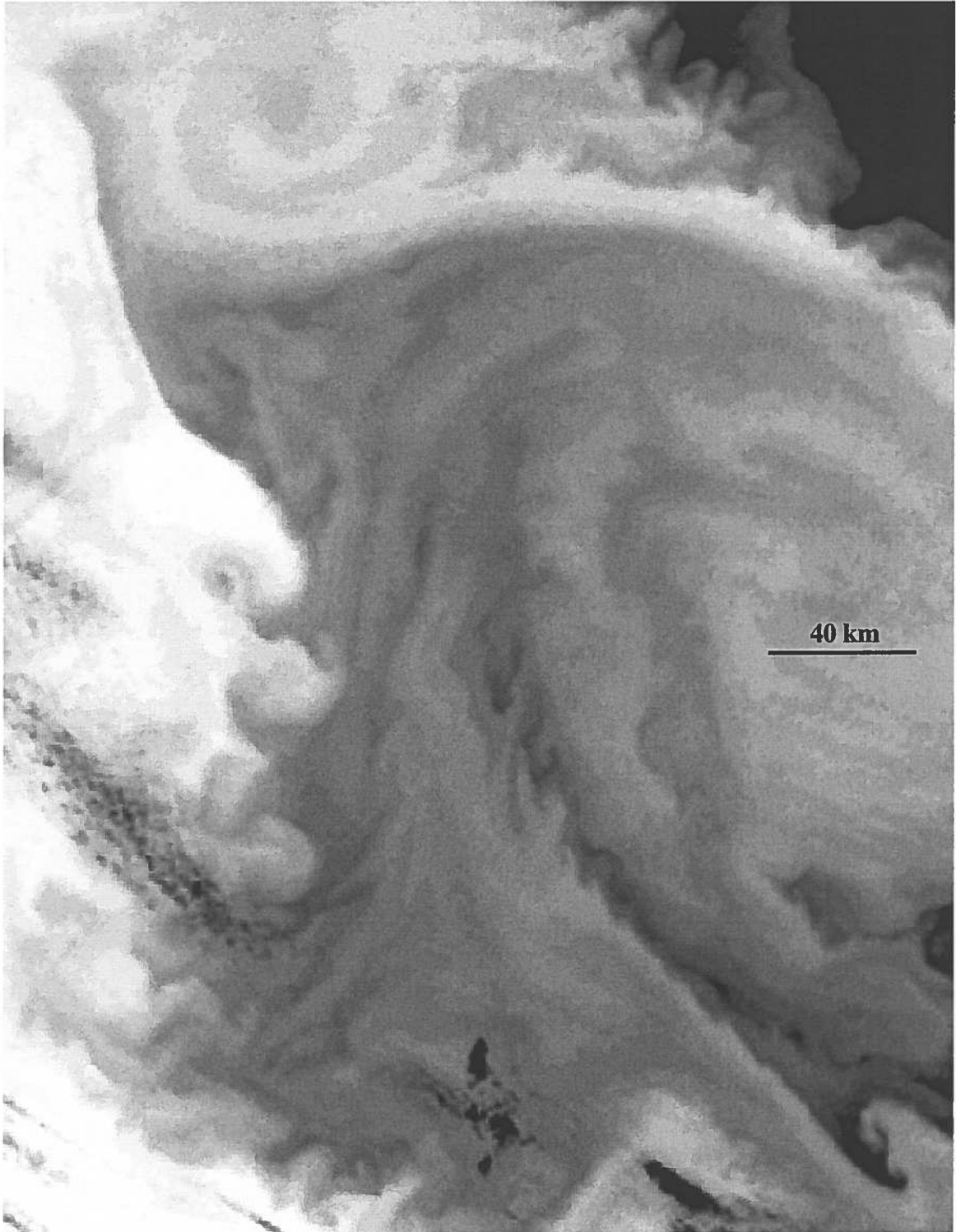


Figure 10. Detail of region B (see figure 3), AVHRR channel 4 at JD 250, GMT 13:36.

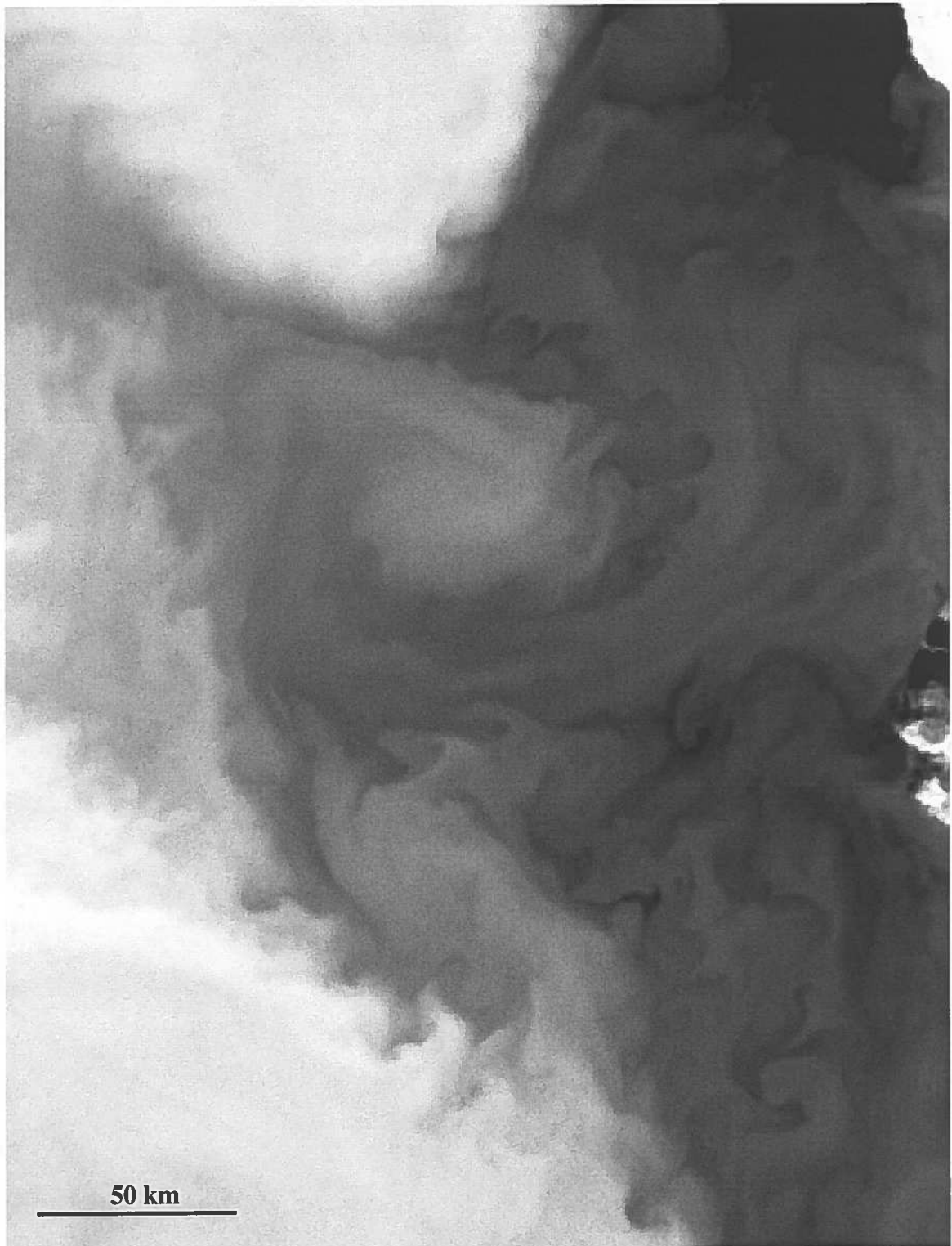


Figure 11. Detail of region C (see figure 3), AVHRR channel 4 at JD 250, GMT 03:22.

CHAPTER 5

AIRSAR IMAGES AND DERIVATIVES

The SAR images from this survey contain a vast array of features, including: (1) the relatively homogeneous periodic field associated with long surface gravity waves, (2) periodic structures with wavelengths of order the mixed layer depth which could be due to either internal waves or secondary vertical circulation, (3) periodic structures of scales exceeding the mixed layer depth implying internal waves, (4) generally anisotropic spatial variations in brightness (or texture) associated with irregular (turbulent) atmospheric and oceanic processes which either modulate the surface spectrum directly, or modulate it indirectly through the redistribution of surfactants, (5) abrupt changes in mean brightness and texture of varying atmospheric and oceanic origin, (6) localized dark linear features attributed to surfactant concentrations, and (7) highly localized bright linear signatures most likely resulting from the modulation of the surface wave field by geostrophic jets. These features delineate such structures as undulations, small-scale vortices, and ultimately the mesoscale structure of the filament itself.

For clarity, a description will be made beginning with the images of the southern region (shown in figure 13), moving to the northern region (shown in figure 12), starting at the near-shore area off Cape Mendicino, off-shore through the core of the filament (figure 14), to the hammerhead thermal front and through the northern branch (figures 15 and 16), and finally through the southern branch of the filament (figures 17-20) for which

the most detailed analysis was done. The chapter ends with a discussion of the long surface gravity wave spectra, as inferred from Fast Fourier Transforms (FFT's) of the SAR images.

5.1 Southern and Near-shore Regions

The relative abundance of dark features within the cold upwelled coastal waters (visible in figures 12 and 13) is likely due in part to the increased concentration of surfactants (and thus occurrence of slicks) in these waters expected from the enhanced primary production of an upwelling system, the abundance of natural petroleum seeps along the central California coast³, and the quantity of anthropogenic runoff. The bright features located in regions of high temperature gradient are likely the product of wave modulation occurring within strong geostrophic jets.

SAR images showing slicks appearing as assemblages of narrow strips are common; this form is assumed to reflect the product of strain which deforms (and tends to stretch) and aligns patches of surfactants, and complex flow which ultimately produces complex "fossil" shapes. A detailed quantitative investigation of this process was not pursued, but the results of Lapeyre et al. (1999) show that the relationship between the physical quantities describing two dimensional flow (strain and effective rotation) establish tracer distribution regimes that might be detectable through a subtle investigation of slick features. That the coastal waters are strain-dominated might be inferred from the variable

3 A slick was visible emanating from a known natural seep near Point Conception in an ERS-1 SAR image from the summer of 1993.

but preferred north-south or along-coast alignment of the slicks visible in figures 21-25.

Bow and stern wakes, and the latter's disruption of surfactant slicks over a width substantially larger than the width of a ship, illuminating the extent of the turbulent wake, can be seen in figures 22 and 24. Periodic structures, some with a distinct internal wave signature, which may be responsible for some of the along-coast alignment, can be seen in figures 24 and 25.

5.2 Filament Core, Hammerhead Front, and Northern Branch

Moving outward from the cape into the core of the filament (figure 14) we encounter a region of sudden transition from nearly homogeneous (speckle dominated) texture to a region of highly anisotropic N \leftrightarrow S aligned variation (figure 26). The transition location is band dependent, suggesting an atmospheric origin. Furthermore, the band dependence and form of the transition are consistent with an off-shore gust front (see pg. 106 of Fu and Holt 1982). However, alignment with a surface thermal structure of cold and probably less stable water suggests a synergy of processes giving rise to the rich texture of the offshore (and presumably low-wind) side of the suspected atmospheric front.

Moving further outward through the core, we encounter a region of large periodic brightness variation (figures 27 and 28). The orientation arcs along the apparent flow direction within the core, but may just as well be described as concentric with the mesoscale anticyclone. The rough distance of periodicity is ~300 m.

At the northeastern edge of the cyclone, SAR images reveal a structure whose

position and alignment with a temperature front casts little doubt of its origin in the thermal front (figures 29 and 30). Although there is some superficial similarity between this structure and the suspected gust front within the core (figure 26), here transition is sharper and its location is band independent, indicators that this is an oceanic (as opposed to atmospheric) signature. Correlation between temperature gradient and intensity of SAR features, both bright and dark, occurs about the entire circumference of this vortex, and it seems likely that some of the mechanisms are common, but some features seen here are unique. The brightest, outermost (w. r. t. the cyclone) line seen in all three bands appears to illuminate a structure which is acting as a wall to surfactants; this suggests the subduction of the waters within the cyclone beneath the waters of the core. Parallel to the brightest line is a second bright line adjacent to a periodic ($\sim 3\lambda$) structure of 100 m wavelength (indicated by the arrow in figure 30). This periodic structure is visible in all three bands.

About twenty kilometers to the west of the large southern branch of the filament is a short lived "V" shaped branch entrained in the mesoscale cyclone (figures 11, and 17-18). The SAR signature of this structure is, in P band, an assemblage of bright lines accompanied by abrupt change from smooth to anisotropic texture, and in C and L bands, an assemblage of dark lines without an associated change in texture (figure 31a). Both the abrupt change in texture coincident with a very sharp structure and the stronger signal at the longer wavelength suggest that the texture signal is of oceanic origin; in this case it appears that the cold water within the branch is described by greater variation in current,

not surprising as the cooler less stratified water is likely more subject to forcing from below. A second bright line, parallel to the prominent line just discussed, can be seen in all three bands; in P band it exhibits a regular periodic structure (for $\sim 1.5 \lambda$) of 80 m wavelength (figure 31b).

SAR images of the hammerhead thermal front, near $40.9^\circ \text{ N } 126.7^\circ \text{ W}$, display a large variety of features, including bright lines in P band, dark lines in L and C bands, and front associated changes in texture (figure 32). SAR images of the hammerhead front near $40.5^\circ \text{ N } 126.5^\circ \text{ W}$ display dark linear and patchy features and very anisotropic texture; periodic structures of $\sim 200 \text{ m}$ wavelength roughly aligned with the front are visible in P band (figure 33).

C and L band images of the northwest edge of the (dipole) anticyclone display at least seven regular wavelengths ($\sim 1 \text{ km}$) of roughly anticyclone-centric dark bands, likely to be the signature of internal waves (figures 34 and 35). The P band image of this area displays none of the regular periodicity at the $\sim 1 \text{ km}$ scale, but rather displays a less regular structure with some periodicity still evident at the $\sim 300 \text{ m}$ to $\sim 500 \text{ m}$ scale; superimposed on the $\sim 1 \text{ km}$ periodic structure, the organization of the slicks seen in C and L bands can be seen to conform to the structure seen in P band. The mesoscale anticyclone can be seen in time series to go through cycles of alternately drawing warm Pacific surface water from the pool just to the north or being isolated from that pool by a region of cooler upwelled water. Such changes in the makeup of surface waters capping the anticyclone will require geostrophic adjustment that could generate internal waves.

5.3 Southern Filament Branch

The southern branch of the filament (figures 11, and 17-20) contains some of the most striking and strongly illuminated of all the SAR images from this survey, including apparent front complexes of multiple (more than two) water-types, an apparent geostrophic jet with, by a factor of four, the strongest modulation of all of the linear features in the data set, cell like alignment of bright and dark linear structures, a jet associated $O(1 \text{ km})$ periodic positively illuminated structure, and possibly instability generated vortex associated curls with periodic substructures. In our description we will begin at the NW or up-filament part of this branch and move to the SE or downstream.

At the position of the second image crossing there is an apparent front complex, illuminated as an assemblage of lines whose sign of illumination (bright or dark) depends on image orientation, implying current induced wave modulation (figures 36 and 37). This structure seems to be associated with a relatively straight section of the thermally imaged southern front of this branch, and not with either of the prominent instabilities whose observed propagation velocities suggest that they will lie to either side.

Continuing downstream through the filament branch we see the very bright signature of a linear structure (figure 38) similar and possibly contiguous to the bright line at the second image crossing. A segment of this structure exhibits two parallel positively modulated lines (figure 39).

This structure continues for over 50 km and displays two cusps where the structure rapidly changes orientation (figures 40-42). The first cusp seems to correspond to the

bifurcation to two fronts (i. e. the presence of three water masses).

The dark streaks to the north of this structure probably represent the accumulation of surfactants due to surface convergence occurring in-between the mixed waters of the cyclone and the colder water of the filament. Though this would seem to be analogous to the case of the northern "V" shaped part of the cyclone (figure 31), the fact that no positive modulation is seen here suggests processes different than those occurring at the northern front of the cyclone (possibly salinity compensation leading to lack of a jet here). These slicks and the jet exhibit a cell-like structure with two strongly preferred alignments separated by an angle of $\sim 40^\circ$. A slick line can be seen through C band to become entrained in the jet (figure 46); this feature provides direct evidence that the jet has a southeastward velocity.

Profiles of the jet for the regions indicated in figure 46 are discussed in section 5.4. The alignment or near alignment of segments of this jet with the azimuthal direction of the SAR image will minimize the velocity contribution to the radar modulation. An insignificant MTF_v greatly reduces ambiguity (the inability to find a unique transformation from image to process) in the analysis of the SAR image of this structure. It also simplifies the design of a numerical simulation for predicting the form of the SAR image.

Parallel to the suspected jet, an $O(1\text{km})$ wavelength periodic structure of ~ 3 wavelengths is seen in P band (figures 42 and 43). The magnitude of the oscillation is ~ 0.5 dB and just detectable within the speckle noise in the image. Historical local

hydrographic measurements indicated that Brunt-Vaisala and interface type internal waves are supported, but the high spatial variance in stratification in this upwelling environment is expected to be highly disruptive to propagating internal waves. In the case of our jet associated structure, the jet might act as a source of energy through either adjustment or secondary flow, to a wave which is confined to the region near the jet due to a propagation velocity which nearly matches the convergence rate (standing wave), or in the case of internal waves with frequency near the Brunt-Vaisala frequency, simply a wave with zero vertical phase velocity component, which (at least in the infinite field limit) does not propagate.

Continuing downstream to the third image crossing we encounter the dark signature of a structure resembling an instability generated vortex (figures 44-46). Within this structure two periodic features can be seen, one of ~150 m wavelength (figure 46) and another of ~220 m wavelength (figure 47). South of the fourth image crossing, another vortex like structure is illuminated, this time positively (figures 48 and 49); a periodic feature of ~300 m wavelength appears to be associated with this structure.

Both SAR imaged vortex-like structures are cyclonic, $O(10 \text{ km})$ scale, and appear to match the positions (determined using time series inferred advection/propagation rates) of vortices visible through AVHRR thermal images (figure 50).

5.4 Jet Profiles

The cross-front SAR image intensity profiles for regions α , β , and γ in figure 40 are shown in figures 51-53, respectively. These regions were selected for their straightness, allowing the widest possible along-segment integration, and thus the best signal-to-noise ratio. The normalized radon transform (via Matlab) was used to produce a pseudo-average of the signal for equidistant (one pixel width) lines parallel to the jet. Through this along-jet averaging, the noise in the cross-jet profiles (due to speckle and the presently irrelevant swell signal) was diminished to less than 0.2 dB.

To first order the structure of these profiles reflects the modulation of a directional surface wave spectrum across a jet. This is what the simulation (see appendix A for details) attempts to describe; the re-adjustment processes, involving dissipation, wind generation, and the cross-spectral processes of wave-wave interaction, collectively referred to as the "relaxation" of the wave field, are neglected. The model is thus expected to deviate from the ocean environment in a band dependent way (e. g. wind input will contribute to stronger deviation at the shorter wavelengths).

In addition, the simulation exhibits some poor behavior which arises from the regridding processes (intended to reduce numerical noise), an unintended consequence of which is a "diffusive" effect on the wave spectrum. This effect may be qualitatively analogous to real processes (e. g. the effect of turbulence), but lacks the natural wavenumber dependence, and in any case no effort has been made to quantify or control this effect.

That said, the simulations are in agreement with the data in terms of positive SAR modulation for regions α and β , but not for region γ , where the simulation produces a negative SAR modulation. It was not resolved whether differences in the real and the simulated wave or current fields might be able to explain the inconsistency for region γ , though the effect of the width of the wave field angular distribution was investigated and is discussed in appendix A.

The simulations produced SAR profiles which are generally narrower than the jet velocity profile, with SAR peaks coincident with the velocity peaks. Thus, the region of significant modulation (~600 m for all bands, at all angles) suggests a jet of ~1 km in width. The velocity peak, inferred from the SAR signal maxima, especially the P band signal, which has a more direct (via less intermediate wave contribution) and reliable (being less affected by microlayer or wind) relationship to velocity, is roughly in the center of the jet.

Considering first only regions α and β , the approximate symmetry of the P band profile suggests an approximate symmetry in the jet velocity profile. Given a symmetric velocity profile, the asymmetric form of the C and L band signals seems to indicate a process other than wave modulation taking place near the center of the velocity peak.

Since the form of the C and L band profiles on the northwest side of the jet most closely resembles that of the P band profiles, it is reasonable to assume that we are dealing with a wind wave field emanating from that direction; this is consistent with the wind data from the off-shore buoy. The more "exponential" increase seen near the peak

in the shorter bands, particularly C band, is likely due to the influence of intermediate wave modulation, whose effect on the short waves through non-linear terms is expected to grow non-linearly with amplitude.

It is just to the lee of the jet velocity maximum (for region α , ~ 12 m or approximately equal to the suspected P band range bias; for region β , ~ 30 m, questionably significant given the low signal to noise near the P band peak) that the "other" process takes hold, rapidly (within 30 m for C band; within 36 m for L band) attenuating the shortest waves while passing the longer waves. It can be seen that to the lee of the zone of attenuation, the rate of negative modulation with distance is approximately equivalent to the rate of positive modulation on the windward side, lending further support for a symmetric jet.

The low-pass attenuation of the waves is consistent with damping due to a surfactant slick with a modulus of elasticity between ~ 20 and ~ 80 mN/m (see figure 1 in Lucassen 1982), within the range of historical direct measurements.

Wave breaking or critical reflection are not likely explanations for the sudden fall-off in the shorter wavelength signals; in either case, positive modulation would still be expected to occur until the velocity peak, giving rise to a sawtooth profile. To reconcile the data with these mechanisms would require a coincident breaking/reflection location and jet velocity peak.

In region γ all three radar bands share the character of gradual increase followed by rapid fall seen in the C and L band signals in regions α and β . The significant damping at P band λ_{Bragg} suggests a modulus of elasticity outside and above the commonly measured

range. From figure 1 in Lucassen (1982) that value would seem to exceed 100 mN/m. If this is true, then we likely have a non-equilibrium surfactant state, where the rate of convergence and rate of surfactant influx (a visible slick entrainment source can be seen upstream) are sufficient to overcome the molecular forces causing spreading.

The consistent presence of a slick adjacent to the velocity peak begs a physical explanation. That the highest density gradients, and thus the jet velocity maxima, are likely to be maintained by convergence seems reasonable; however, given this "convergence driven" mechanism, a jet with historical analogs of O(100 m) depth would be expected to display less coincidence between velocity peak and convergence.

An alternative "jet driven" mechanism proposed by Flament and Armi (2000), where the inflection in the second derivative of the horizontal velocity drives a secondary flow and convergence to the right of the velocity peak can be shown to result from the Navier-Stokes equation with constant eddy viscosity. Alternately, or in tandem with this process, the shears, both vertical and horizontal, are likely to give rise to a spatial variation in K_H and K_V that by itself (without the velocity inflection) might give rise to convergence.

In contrast to region α , where there is no net leeward decrease in P band signal across the jet, there is an approximately 1 dB net reduction in P band signal across the jet in region β . The simulation results for region β predict no such reduction for this range of geometries, however, this characteristic could be concealed by the spectral "diffusion" inherent to the simulation (discussed above), which is also responsible for the leeward increase in signal produced by the simulation for region α .

Possible explanations for the leeward decrease in the SAR signal for region β include: (1) a net velocity change across the jet where southwest flow is higher on the northeast side of the jet, (2) a current field with significant convergence, (3) critical reflection losses at the Bragg wavenumber or significant intermediate wave components (which need not have the same propagation direction as the Bragg waves), or (4) the dominance of relaxation process such as a significant net cross-spectral transfer from wavelengths O(P band λ_{Bragg}) taking place as the wave field propagates across the jet.

Critical reflection losses near P band λ_{Bragg} , will be zero for the nearly orthogonal orientation of the jet in region α , but for the $\sim 12^\circ$ orientation of the jet in region β , a jet with a core velocity exceeding ~ 2 m/s would give rise to critical reflection (equation A7). A core velocity of this magnitude is not far outside historical measurements.

Cross-spectral transfer is expected to be enhanced in the interior of the jet, where wave amplitudes are significantly higher, increasing the non-linear coupling terms.

The simulation for region β , if modified to describe scenario (1), is expected to reproduce the form seen in the data, however, the same is expected for region α , where the higher lee-ward SAR signal in the model for the symmetric jet case is inconsistent with its analytical form, making such a comparison somewhat insubstantial.

Secondary features which can be observed include:

(1) Humps are discernible windward of the peaks in the C and L band profiles (in all three regions) ending ~ 60 m before the peak. Two possible explanations have been considered: (1) critical reflection (as described by equation A7) and, (2) a persistent

complex jet velocity profile. If (1), then the band independence of the feature suggests the critical reflection of a significant intermediate scale wave (which again, need not have the same propagation direction as the Bragg waves), as opposed to that of the associated C and L band Bragg wavelengths.

(2) in region β , to the lee of the negative modulation influence of the jet, the restoration (direct wind driven) of the wave field about L band λ_{Bragg} to equilibrium (pre-jet values), from approximately 1 dB below equilibrium, occurs over a distance of ~ 0.5 km. Near C band λ_{Bragg} , apparently the regeneration scale is small enough that negative modulation below the wind generated equilibrium by the shear levels existent in this jet is impossible.

5.5 Long Gravity Wave Spectra

The SAR image spectra for the region of the Cape Mendicino filament show peaks at $\sim 0.047 \text{ m}^{-1}$ ($\lambda \sim 130 \text{ m}$) and $\sim 15^\circ$ NNW with a spread of $\sim 0.02 \text{ m}^{-1}$ and $\sim 40^\circ$. Within this envelope, the structure fluctuates with peaks arising and vanishing at scales less than 3 km, or persisting for more than 30 km. An intriguing twin peak form is recurrent and most pronounced in the coastal zone near the cape. Spectra from the coastal zone near Point Arena show the absence of a northerly signal consistent with shielding from the cape. No spatial variation consistent with a signature of modulation by the flow field was resolved.

A representative spectrum from a low resolution image near the southern branch of

the filament is shown in figure 54. A lower wave number peak at $\sim 0.017 \text{ m}^{-1}$ ($\lambda \sim 370 \text{ m}$) directionally aligned with the swell is common in these spectra. Such a peak could potentially be an artifact of the SAR imaging processes, resulting from the swell beat imaged through a non-linear MTF; however, non-directional wave data from the NOAA buoys corroborate this as a surface wave signal (figure 55). Raw, high-passed (illuminating the $\sim 130 \text{ m}$ wind swell), and low-passed (illuminating the $\sim 370 \text{ m}$ waves) spectra, and their associated images, from a high resolution image near the southern branch of the filament, are shown in figure 56-58.

The $\sim 15 \text{ s}$ ($\sim 370 \text{ m}$) surface wave spectral peak is at precisely the wave number (direction and magnitude) expected for waves extracting their energy from the $\sim 9 \text{ s}$ ($\sim 130 \text{ m}$) swell through non-linear processes involving the beats arising from the 0.02 m^{-1} spread in the dominant swell:

$$k_{\text{beat}} = |k_{\text{short}} - k_{\text{long}}| \quad (14)$$

Long gravity waves of origin in this generation mechanism are called infragravity waves.

Seeking a storm source for the $\sim 15 \text{ s}$ wave energy, in the northern hemisphere tropics the most probable storm source would be tropical storm Narda, which ultimately fails as a source due to position, heading, and marginal winds. Excluding an unaccessed region near Antarctica, there were no other candidate storms. Given the large waning 15 s tropical storm attributed signal detected at the near-shore buoys no more than 24 hours earlier, the SAR spectra signal could be attributed to the reflection maintained storm-wave background.

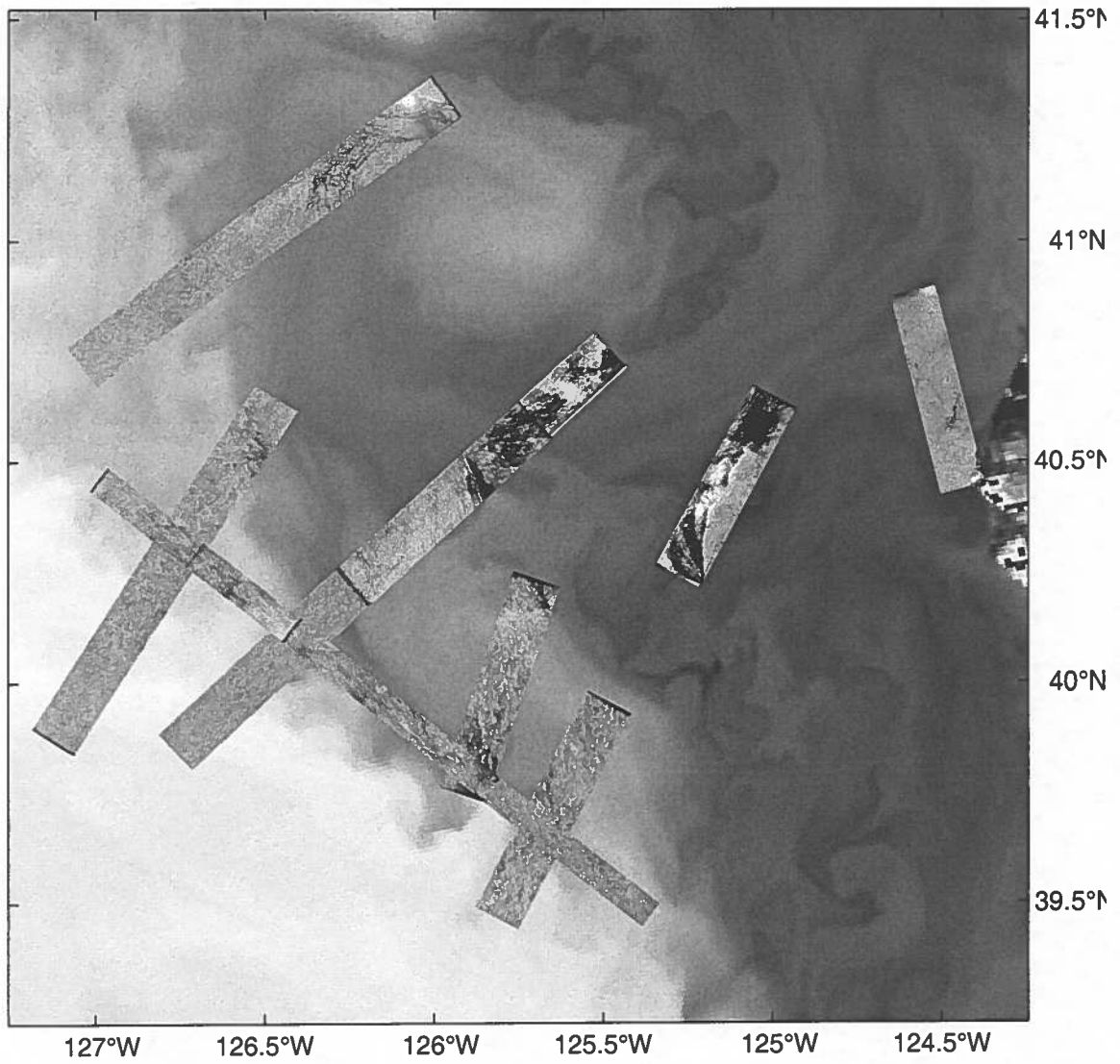


Figure 12. Northern region of SAR survey focusing on the Cape Mendicino filament, AVHRR channel 4 at JD 250, GMT 03:22 / AIRSAR L band.

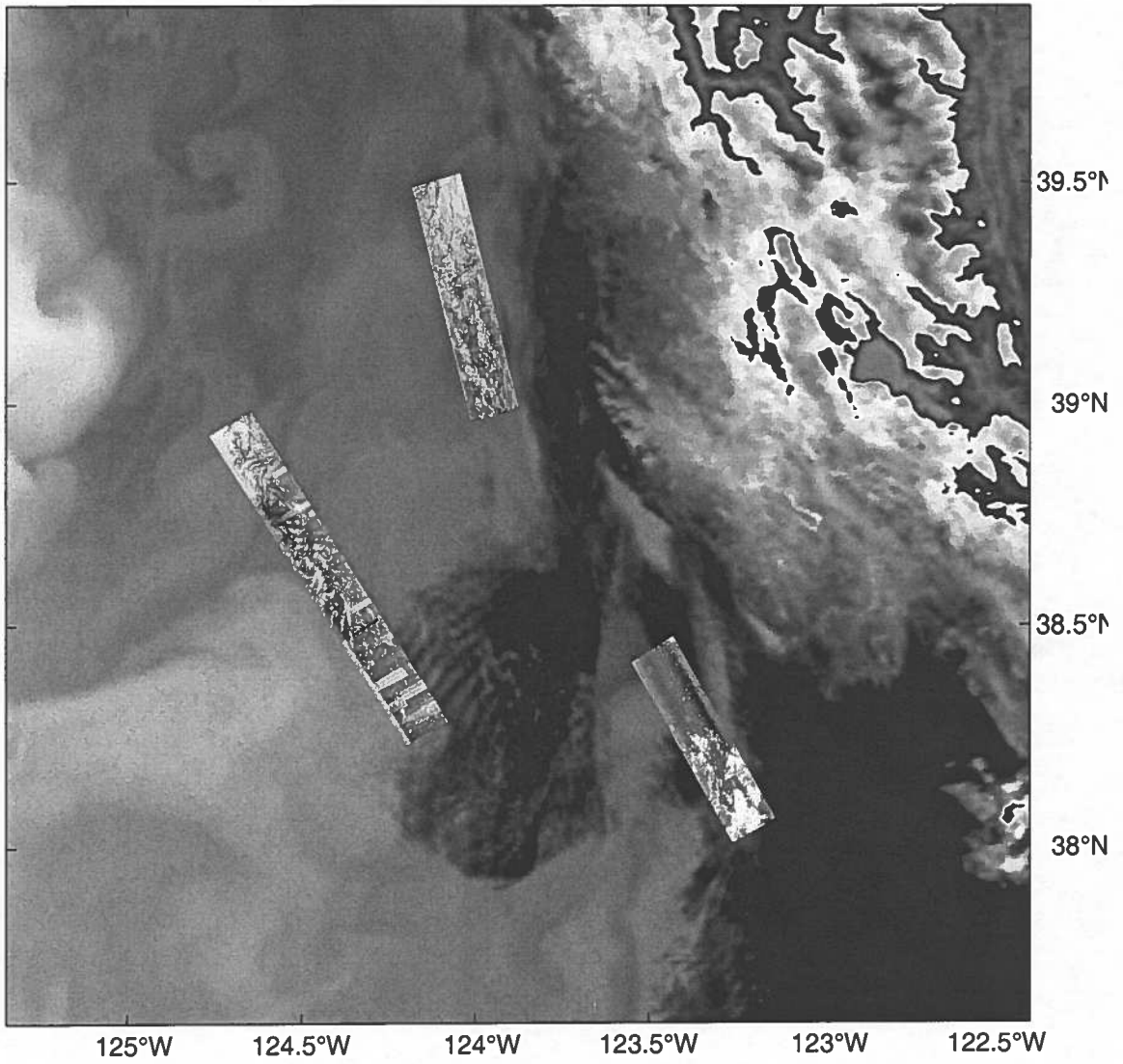


Figure 13. Southern region of SAR survey, AVHRR channel 4 at JD 250, GMT 03:22 / AIRSAR L band.

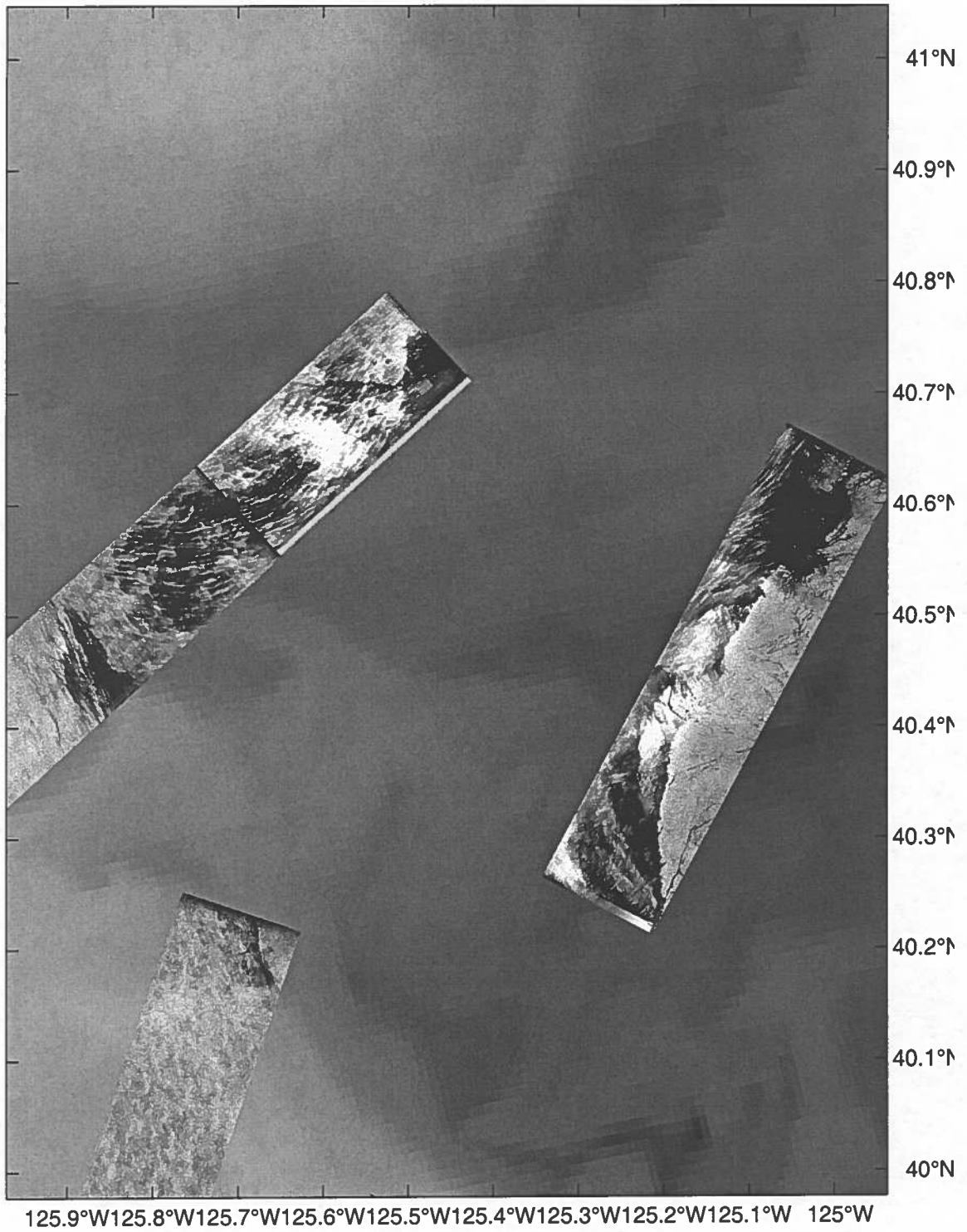
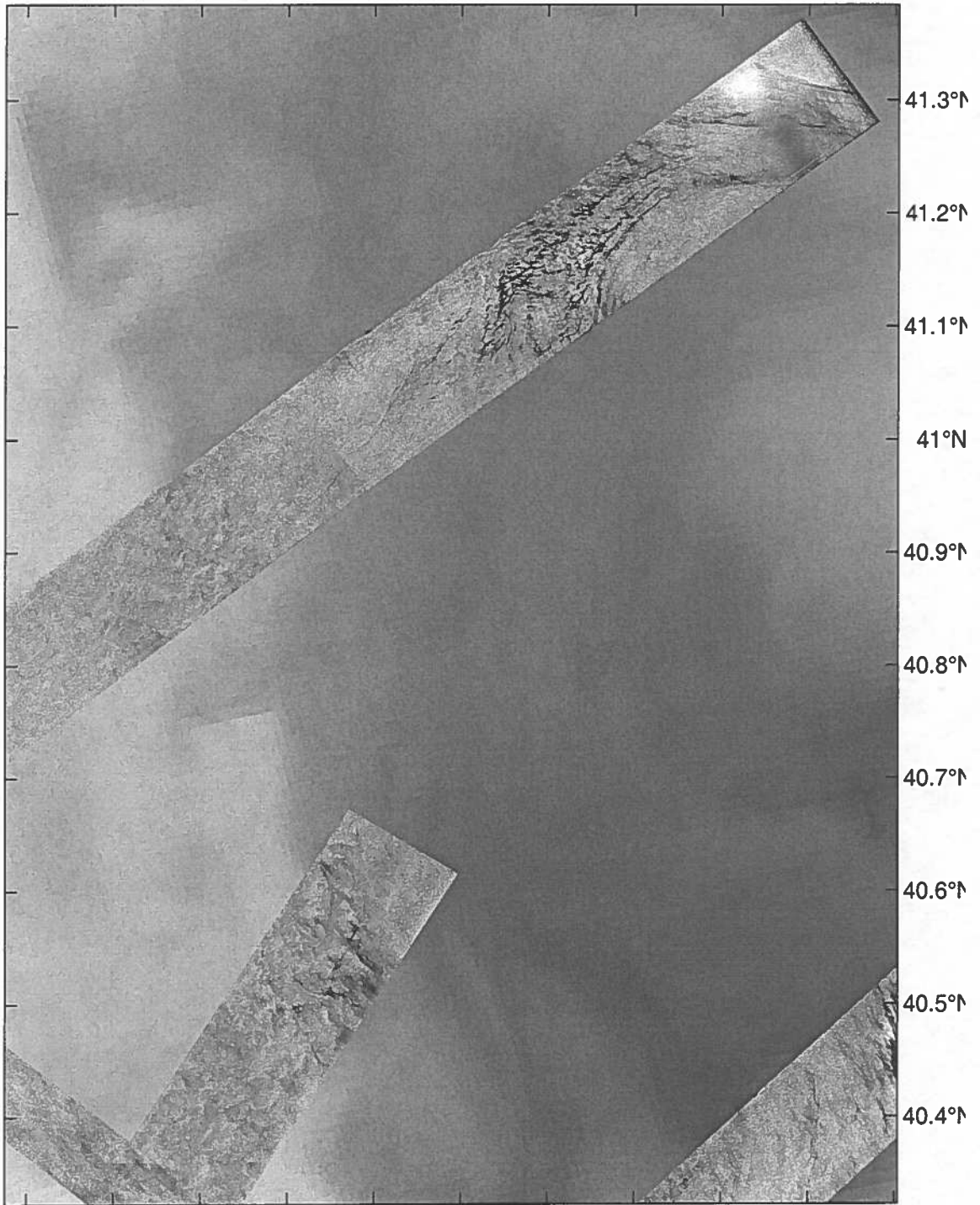


Figure 14. Core of the filament, AVHRR channel 4 at JD 250, GMT 03:22 / AIRSAR L band.



26.9°W126.8°W126.7°W126.6°W126.5°W126.4°W126.3°W126.2°W126.1°W 126°W 125.9°W

Figure 15. Northern branch and center of hammerhead front of the filament, AVHRR channel 4 at JD 250, GMT 03:22 / AIRSAR L band.

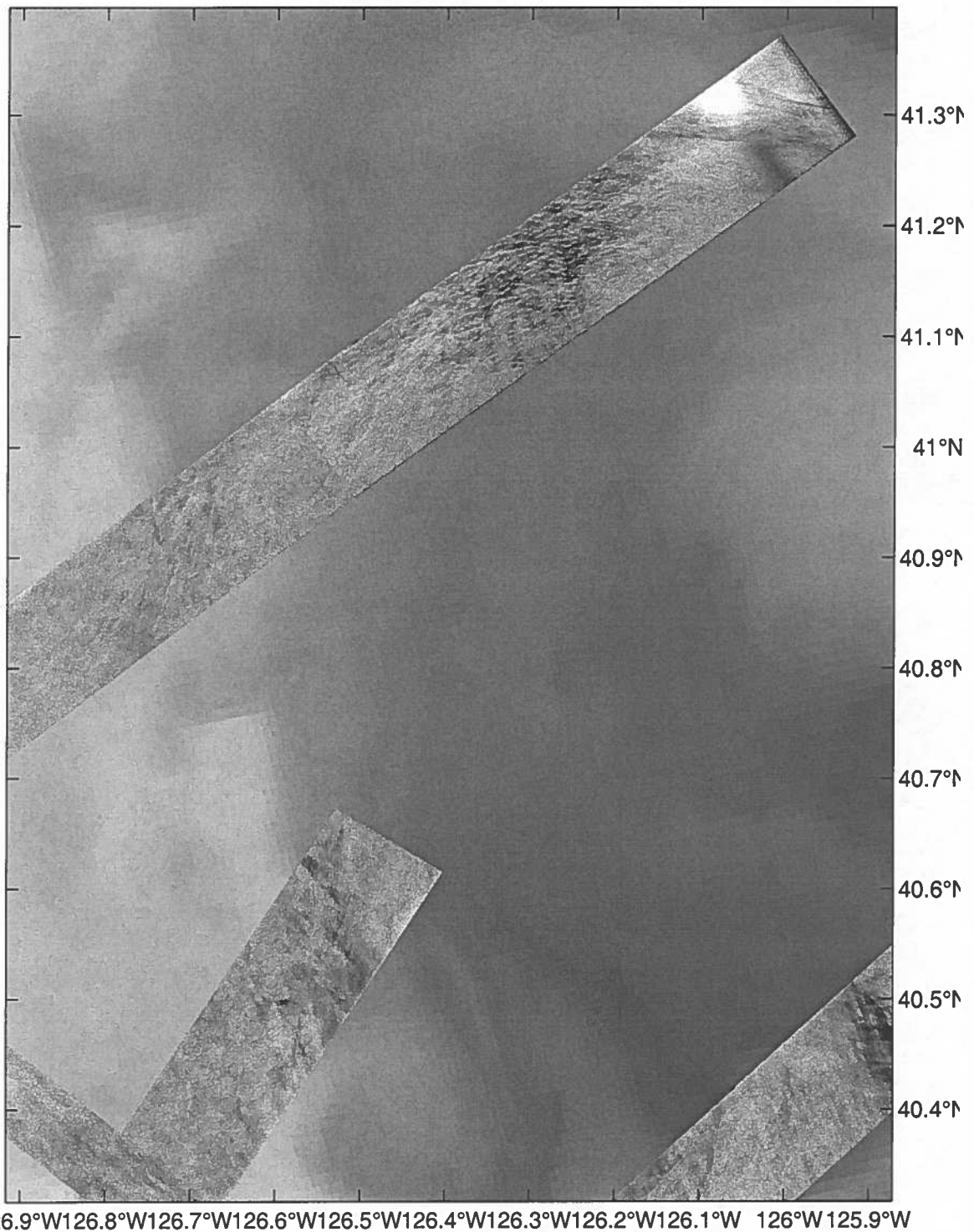


Figure 16. Northern branch and center of hammerhead front of the filament, AVHRR channel 4 at JD 250, GMT 03:22 / AIRSAR P band.

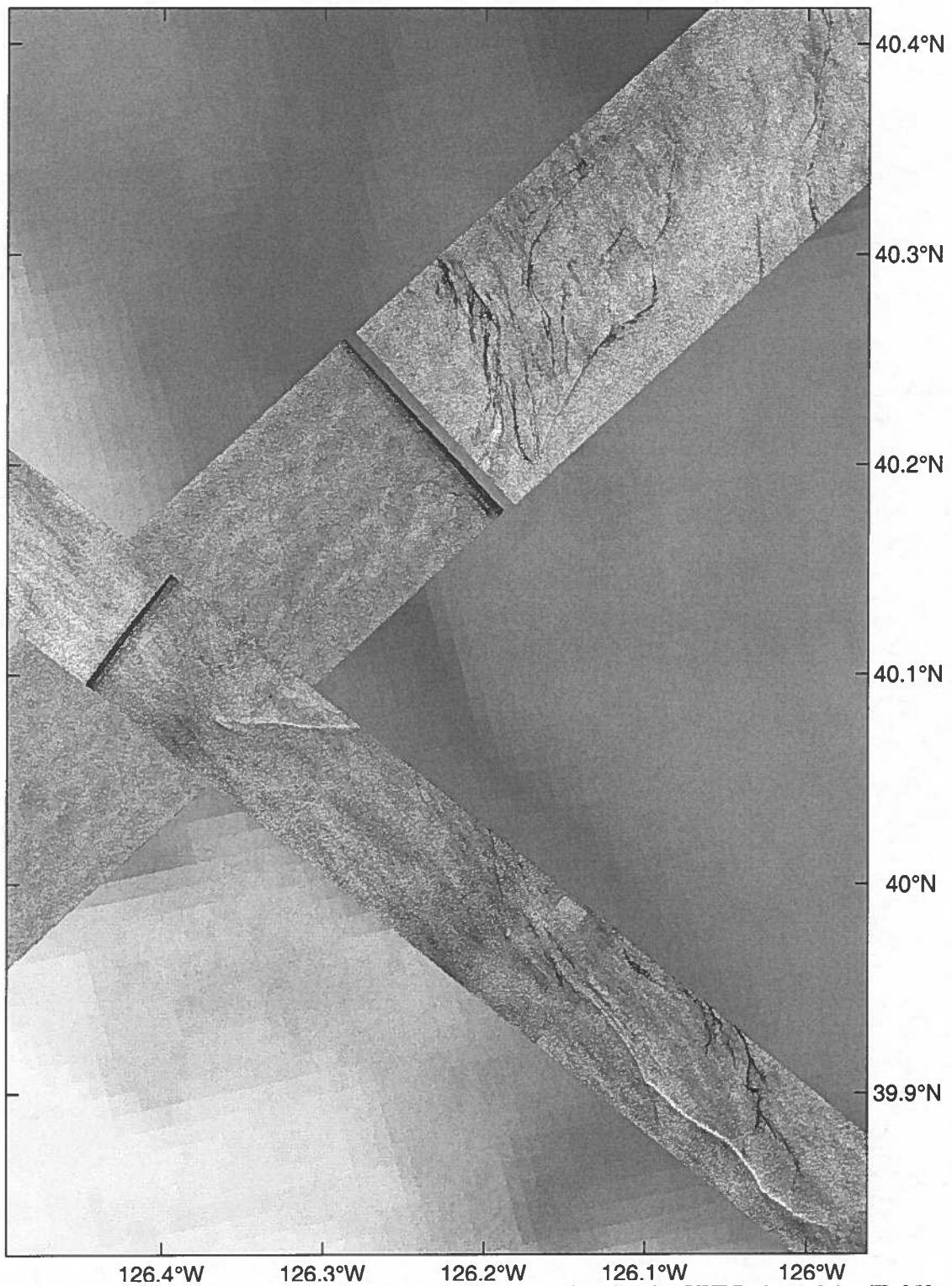


Figure 17. Northwestern part of southern branch of the filament in L band, AVHRR channel 4 at JD 250, GMT 03:22 / AIRSAR L band.

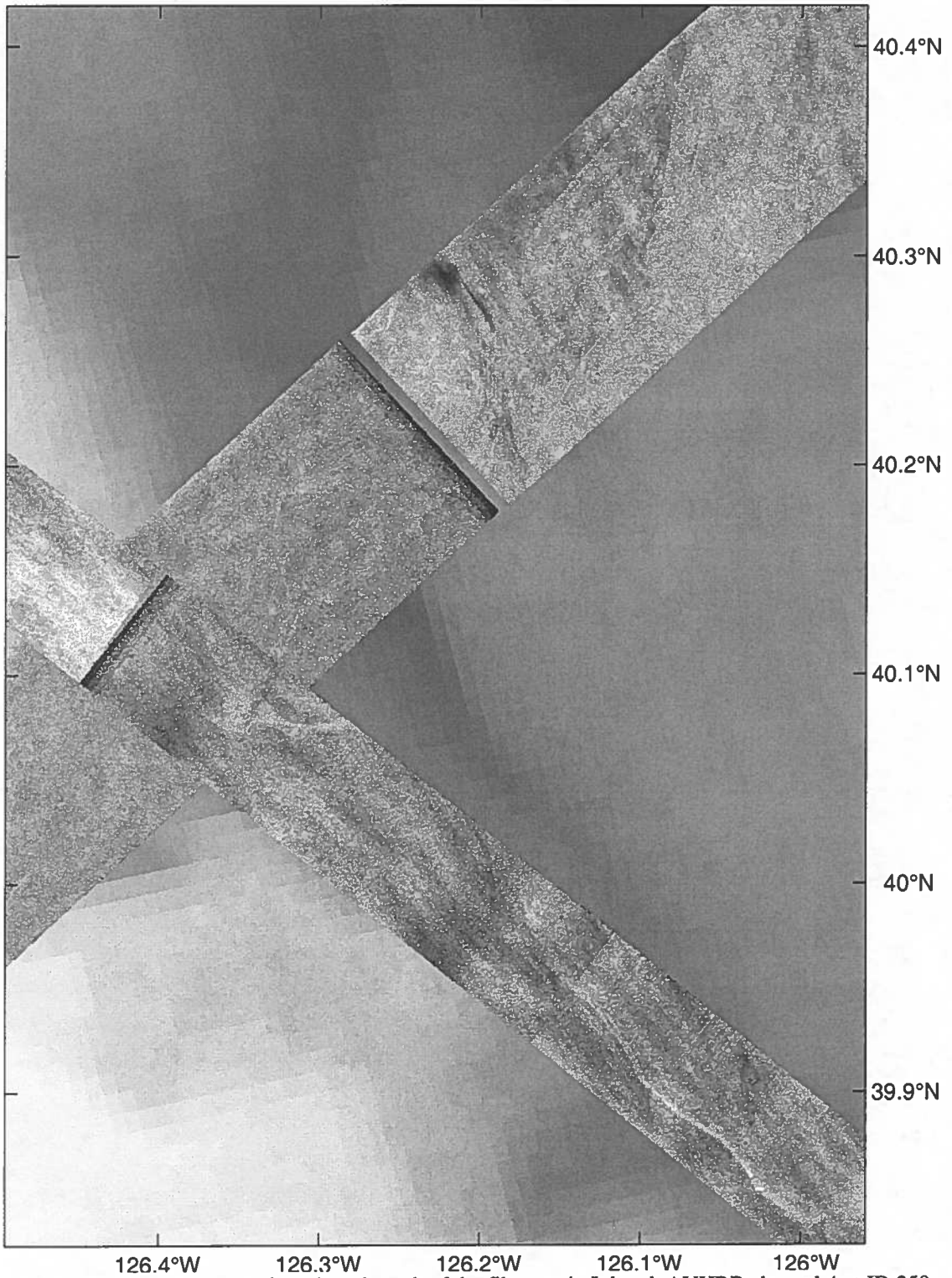


Figure 18. Northwestern part of southern branch of the filament in L band, AVHRR channel 4 at JD 250, GMT 03:22 / AIRSAR P band.

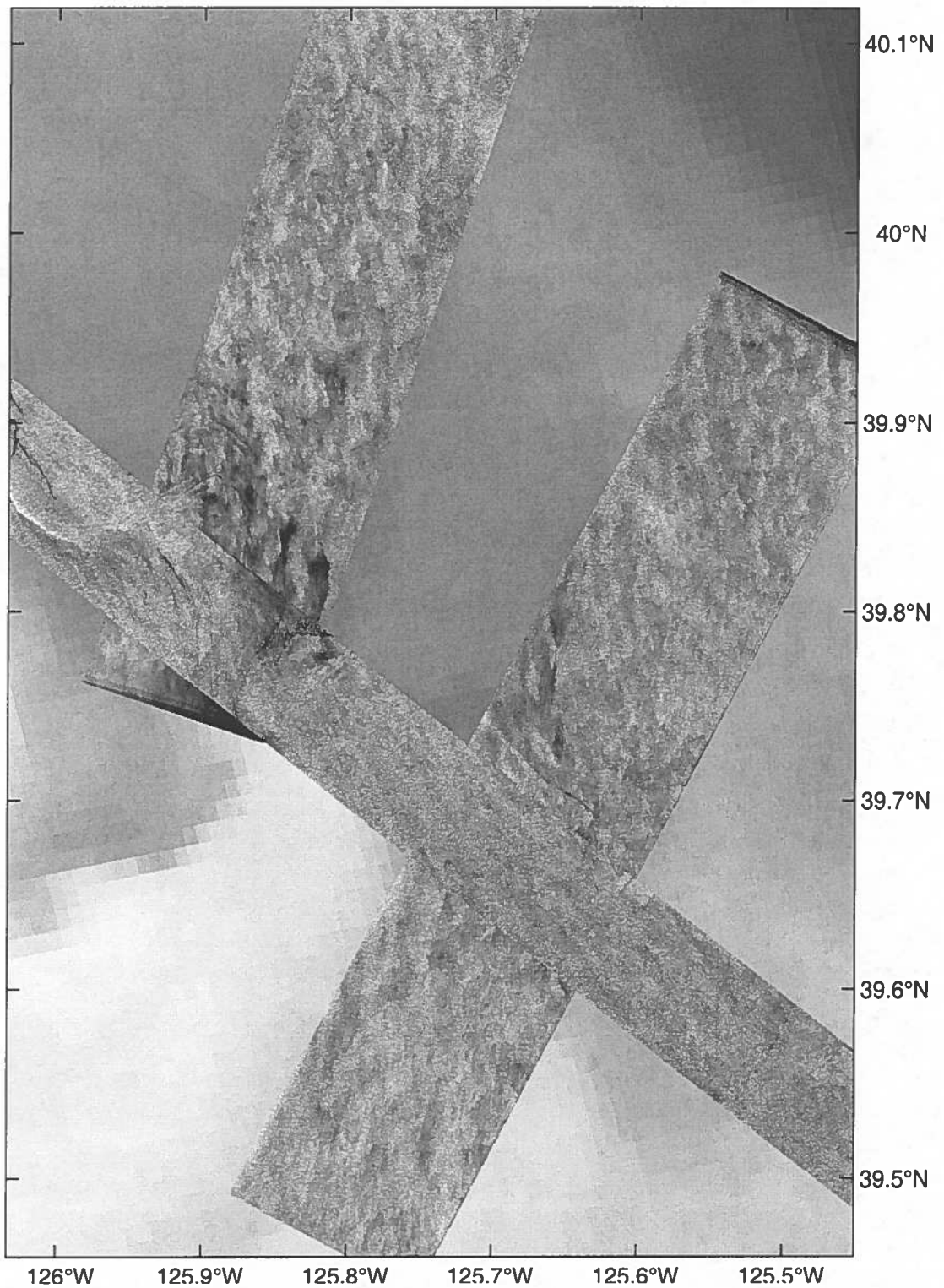


Figure 19. Southeastern part of southern branch of the filament in P band, AVHRR channel 4 at JD 250, GMT 03:22 / AIRSAR L band.

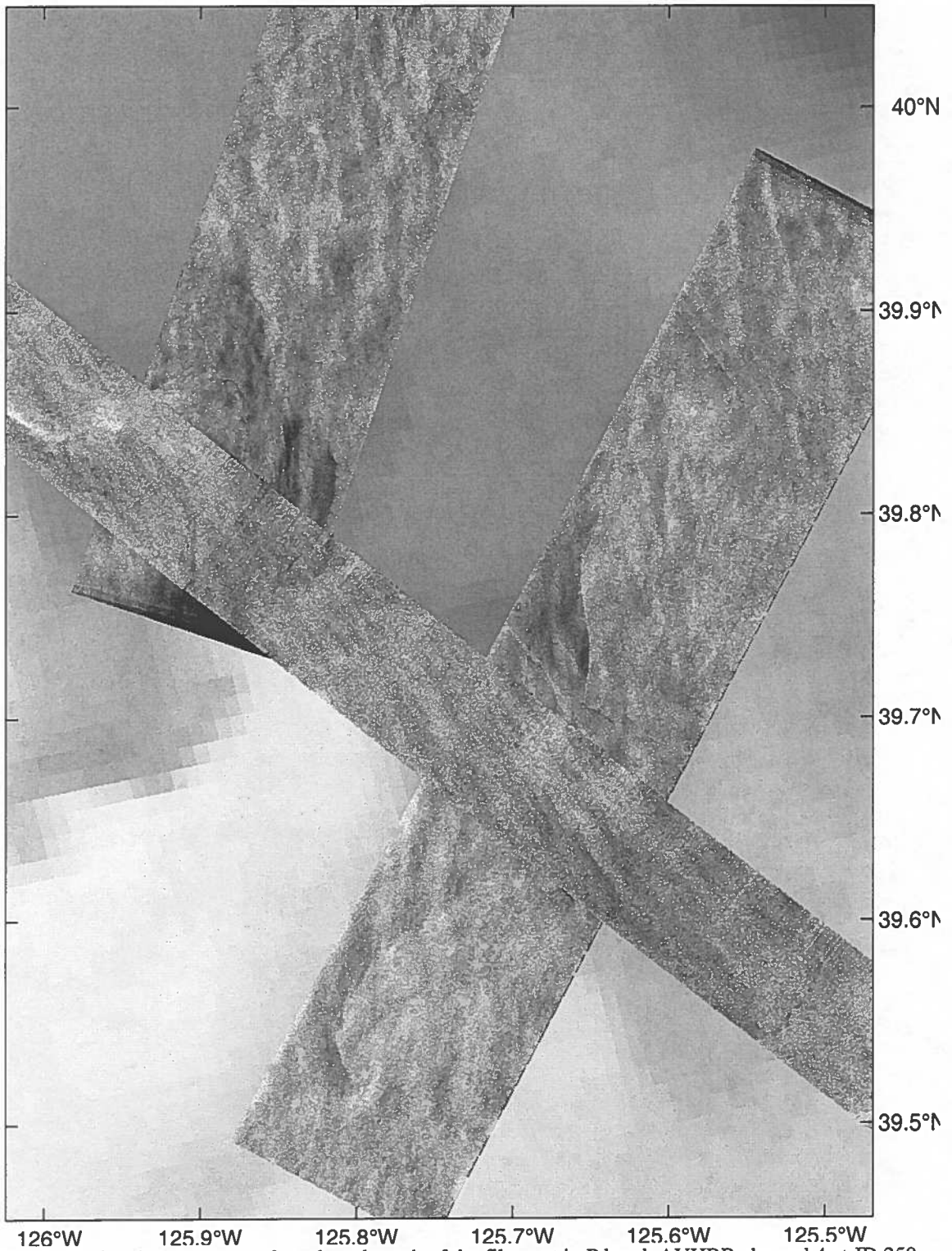


Figure 20. Southeastern part of southern branch of the filament in P band, AVHRR channel 4 at JD 250, GMT 03:22 / AIRSAR P band.



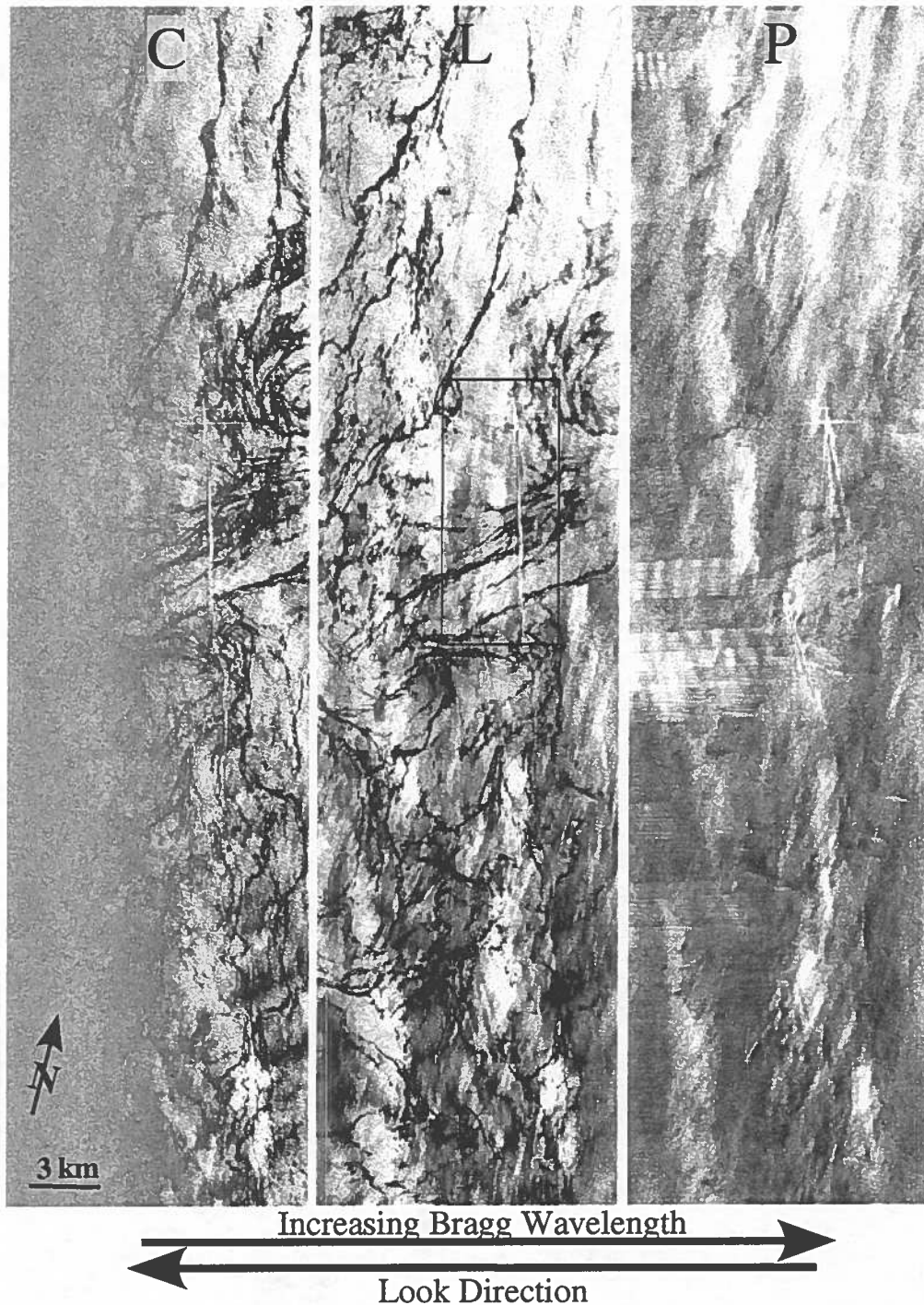


Figure 21. AIRSAR C, L, and P band images of southern region, centered at 39.2°N 124.0°W. Narrow dark lines are surfactant slicks, which are seen to be disrupted by the passage of a ship. The O(5 km) variations in backscatter seen in L and P bands are possibly an atmospheric signature manifested in the radar images through a variation in surface wind speed, suggesting the spatial scale of turbulent motion in the atmosphere. Loss of signal in the far range of the C band images is discussed in appendix B. Horizontal bands seen in P band here and also in L band in figure 23 are interference from land based microwave communications.

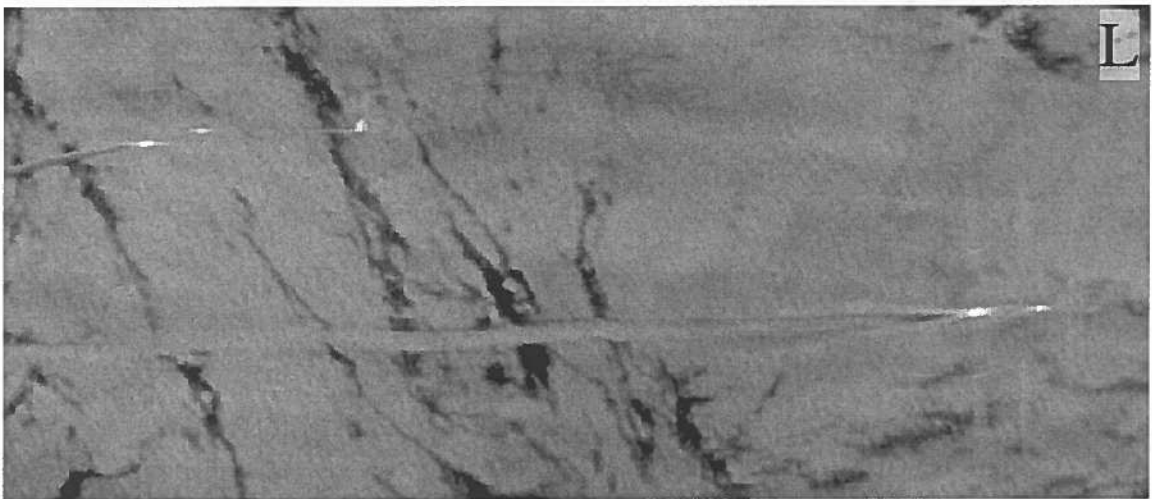
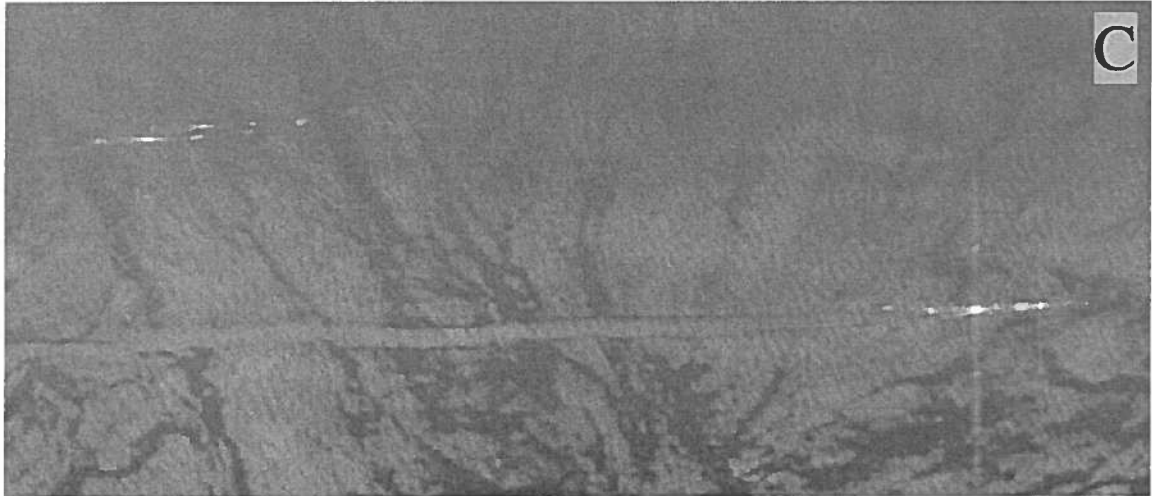


Figure 22. Detail of ships. Ghosts and bars about the ships likely result from the high radar cross-section of the ships combined with beam side-lobe and electronics effects. Bow and stern wakes are visible. The prominent disturbance of surfactants produced by the stern wake is 170 m wide.

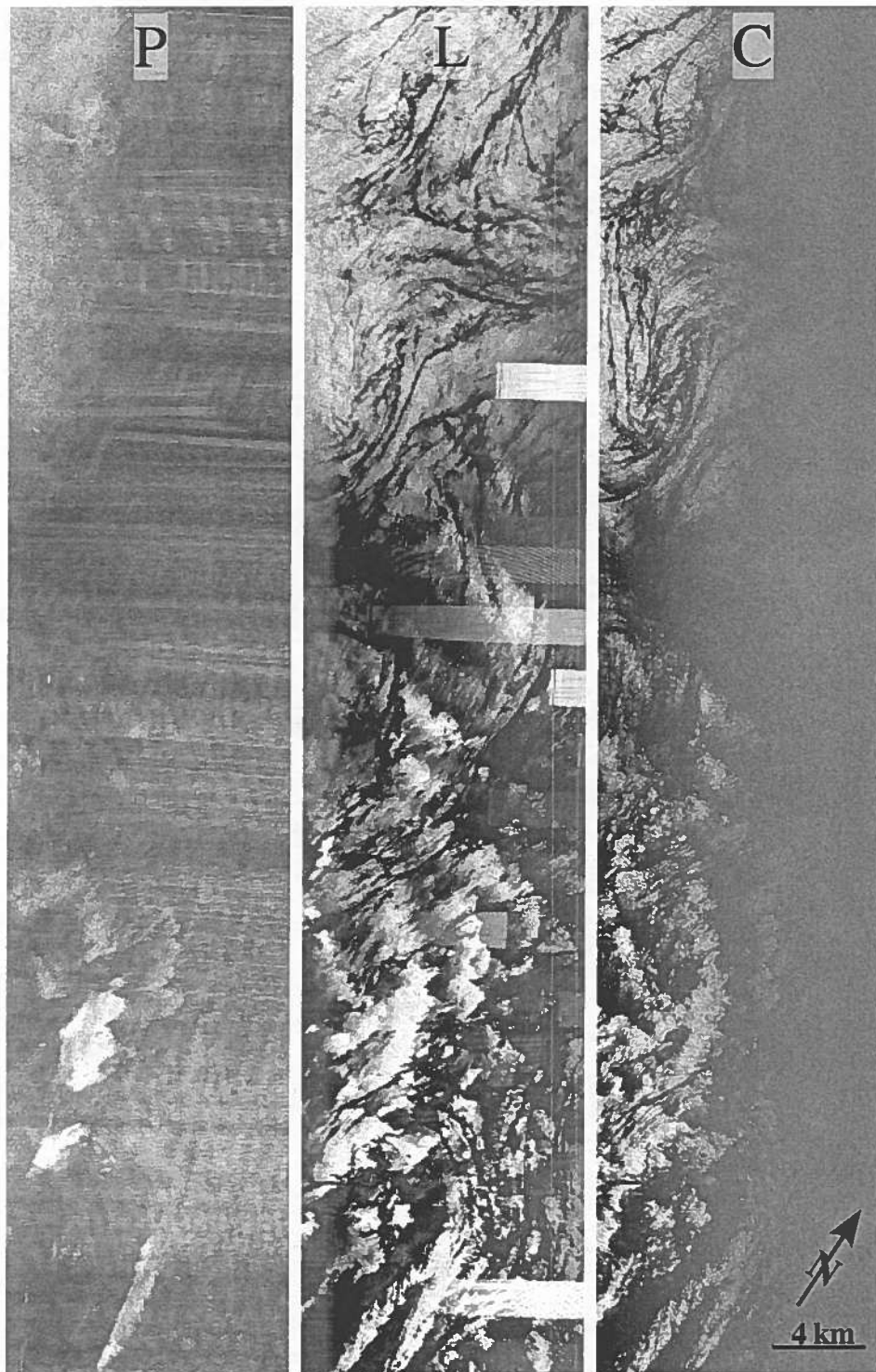


Figure 23. AIRSAR C, L, and P band images of southern region, centered at 38.7°N 124.5°W . Surfactant slicks, similar to those in figure 20, are seen near the top of these images, in the middle and toward the bottom, ~ 3 km periodic variations in backscatter are suggestive of the similarly scaled atmospheric internal waves visible in AVHRR thermal the previous day near this radar image location through cloud condensation.

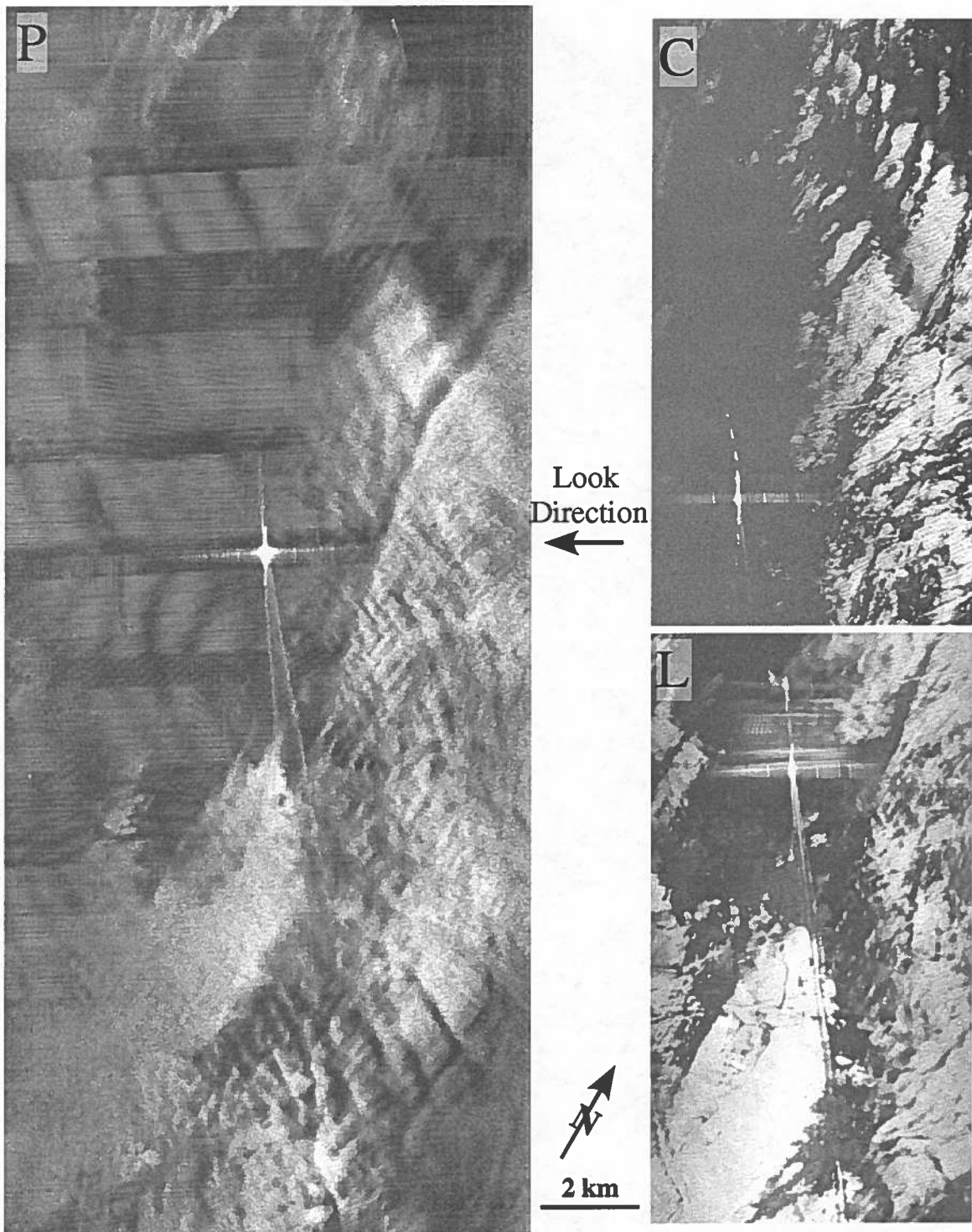


Figure 24. AIRSAR C, L, and P band images of southern region, centered at 38.2°N 123.3°W. Internal waves are visible on the left side of the P band image. A ship leaving a disturbance of surfactants 150 m in width is visible in L band. The azimuthally displaced ghosts (outward curved and dashed in C band) are consistent with side-lobes effects. The range displaced ghosts are likely due to electronic signal processing effects, though their exact nature is not clear.

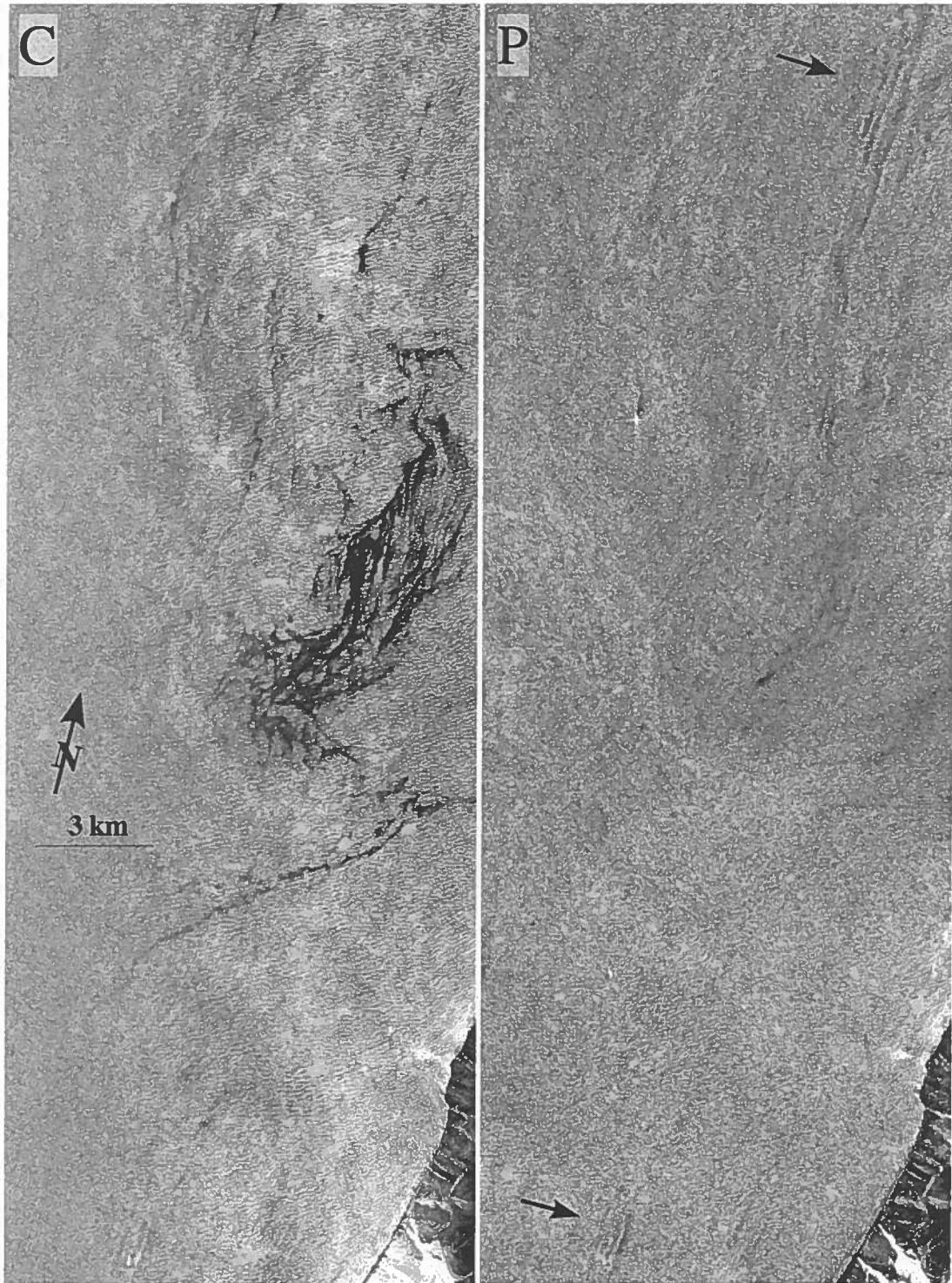


Figure 25. AIRSAR C and P band images of region nearshore of Cape Mendicino. Dark patches in C and P bands are slicks, some $O(1 \text{ km})$ variation in surface backscatter is visible in C band, internal waves are indicated by the arrows and are aligned with the coast.

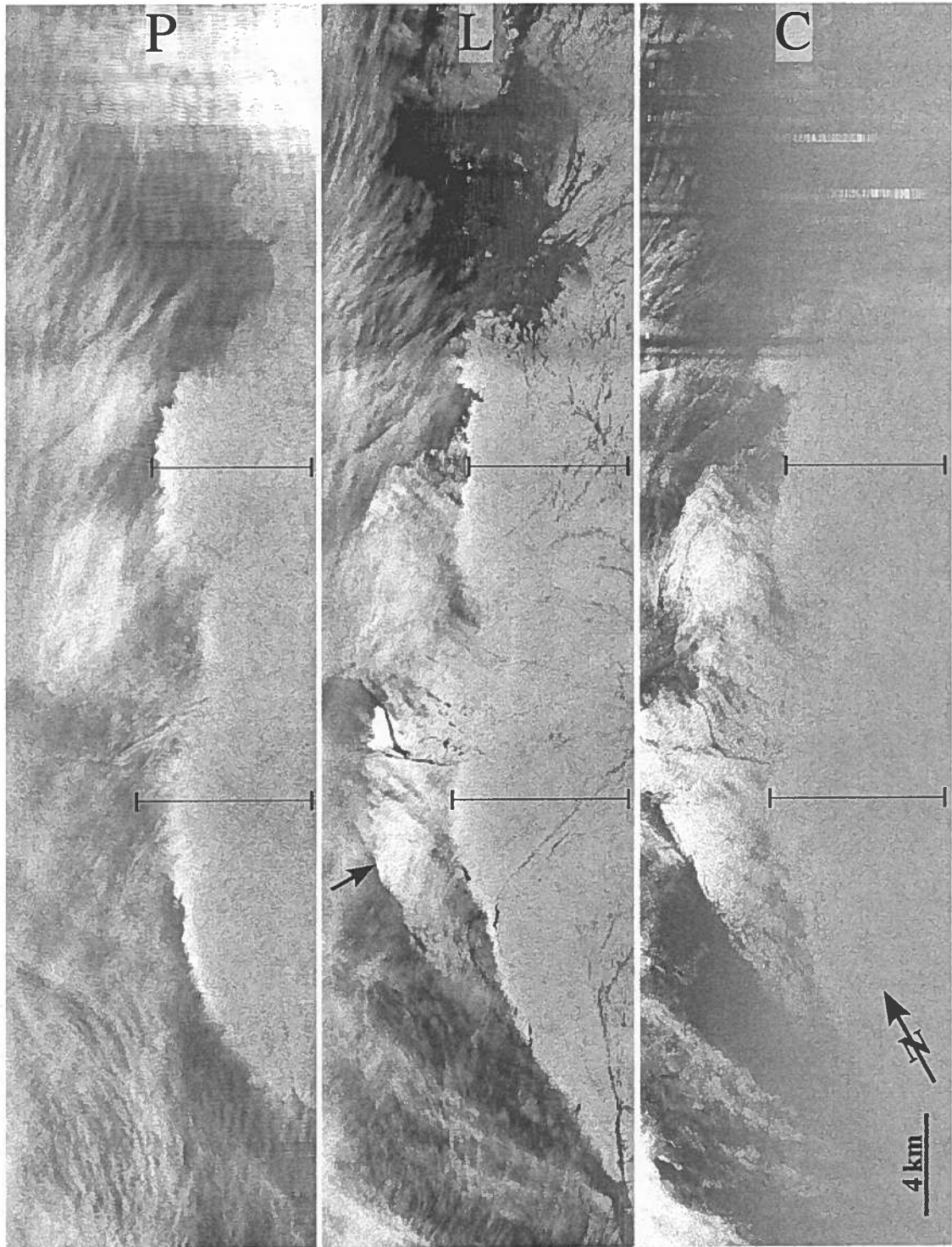


Figure 26. AIRSAR C, L, and P band images of core of filament, centered at 40.4°N 125.1°W. The transition from high backscatter and low variance to low backscatter and high variance. The brighter signal about the edge is suggestive of a gust front. The delayed transition of P band relative to C and L bands supports the hypothesis of an atmospheric front.

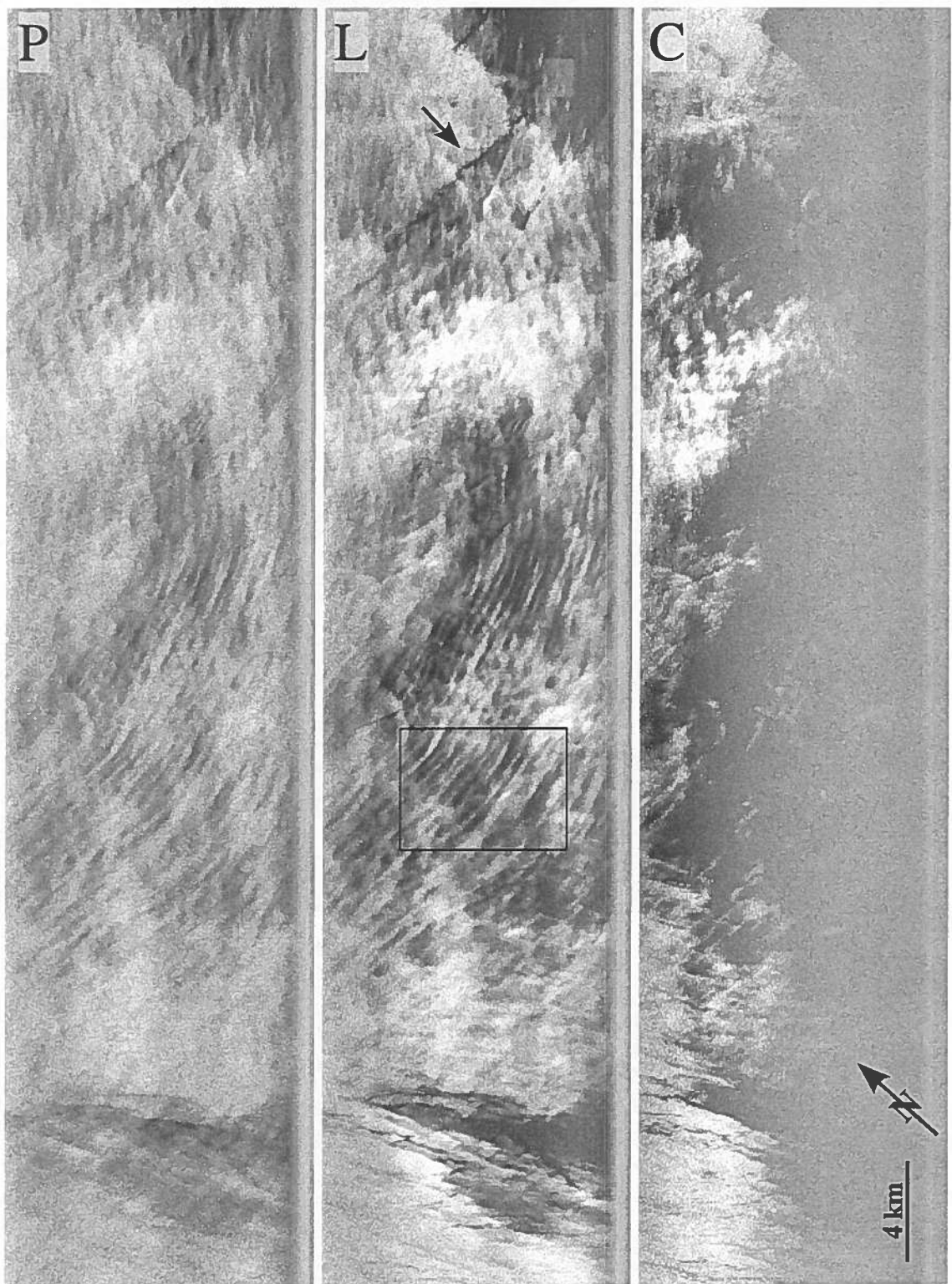


Figure 27. AIRSAR C, L, and P band images of core of filament, centered at 40.6°N 125.7°W . Prominent are the ~ 300 m periodic structures curving as though concentric with the anticyclone. A strange V shaped structure is indicated by the arrow.

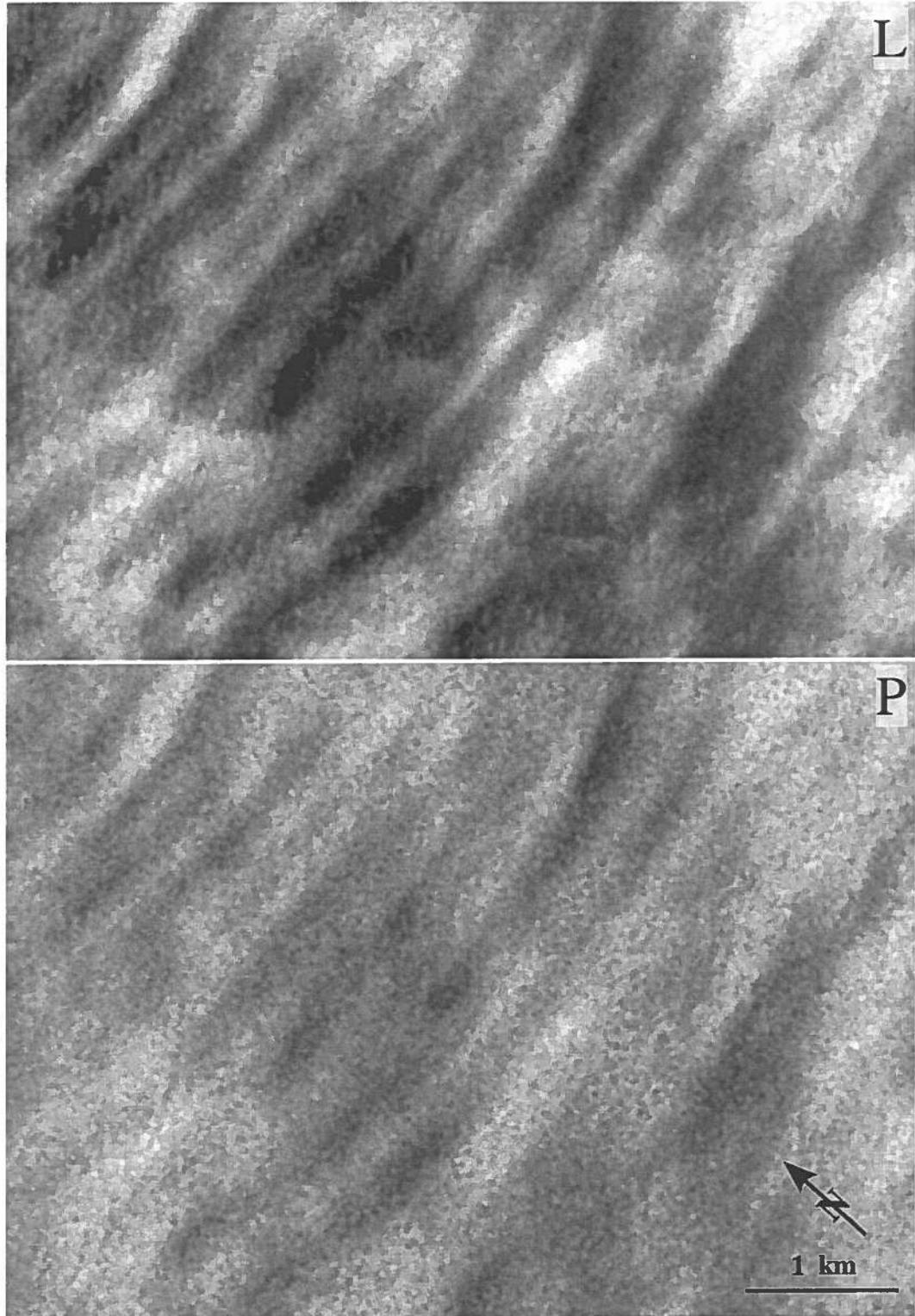


Figure 28. Detail (the region indicated by the box in figure 27) of L and P band images of ~300 m periodic structures.

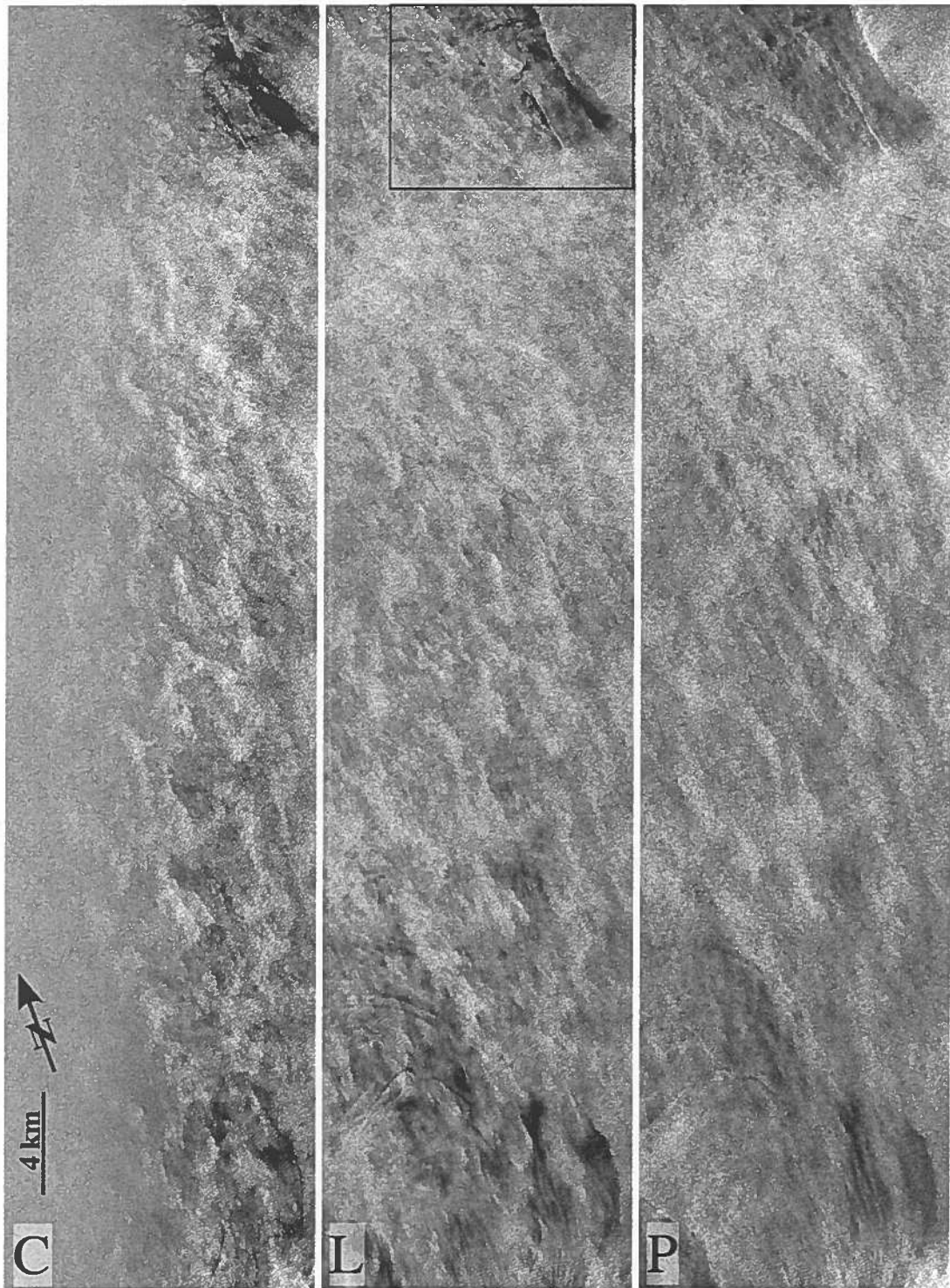


Figure 29. AIRSAR C, L, and P band images of the mesoscale cyclone, centered at 40.0°N 125.8°W. O(km) anisotropic variations in backscatter could be either atmospheric or oceanic flow traditionally described as turbulent.

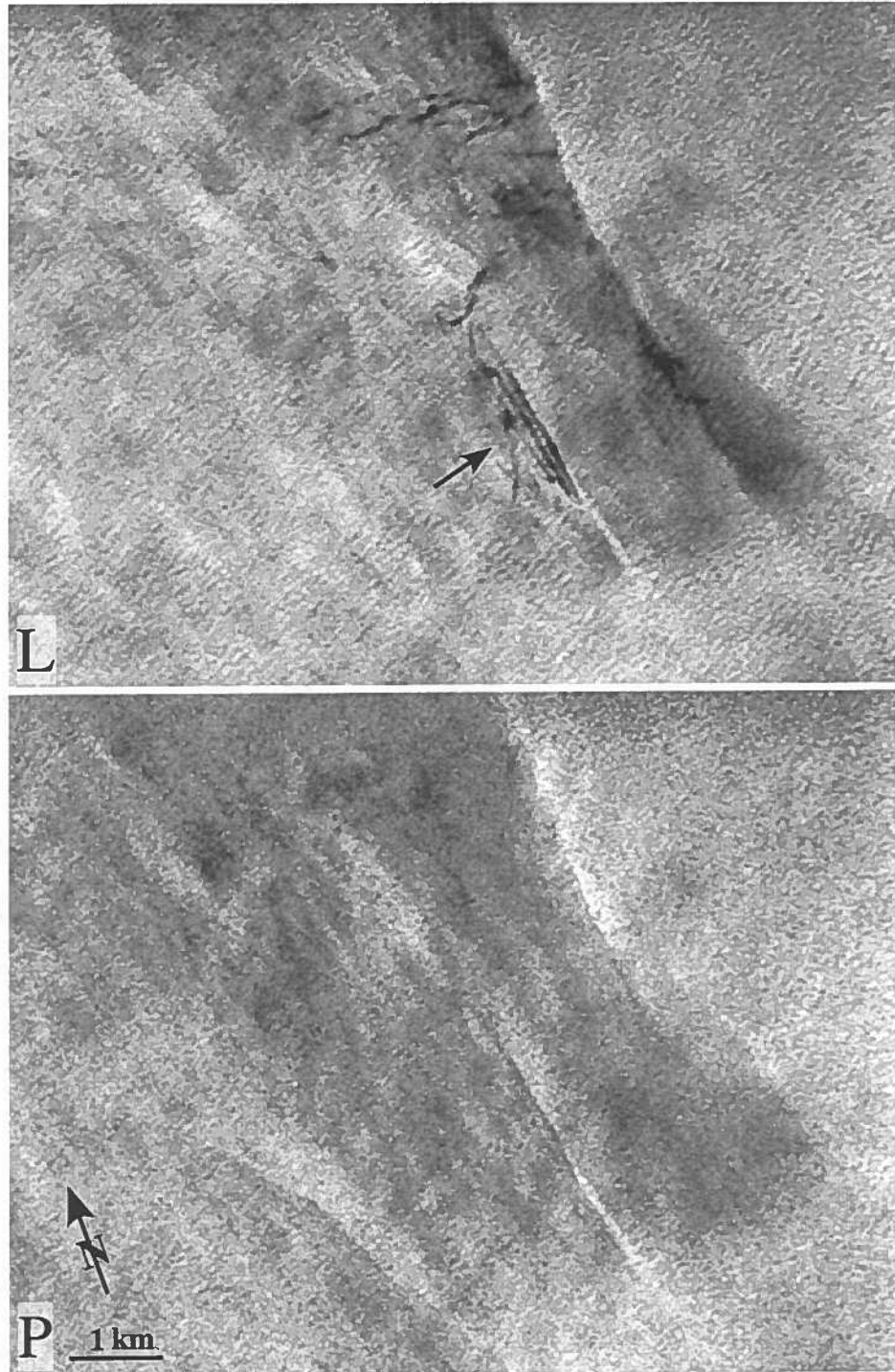


Figure 30. Detail of radar signature of front at the north of the cyclone. Subduction of the western water below the eastern water appears to be occurring here, evidenced by the termination of slick lines at the line of strong wave modulation (the right-most bright line). Periodic structure (indicated by the arrow) of ~100 m wavelength occur at a second parallel line of strong wave modulation. It is likely that the modulation is current induced. The periodic structure could be very short wavelength but high amplitude internal waves illuminated through the periodic concentration of surfactants.

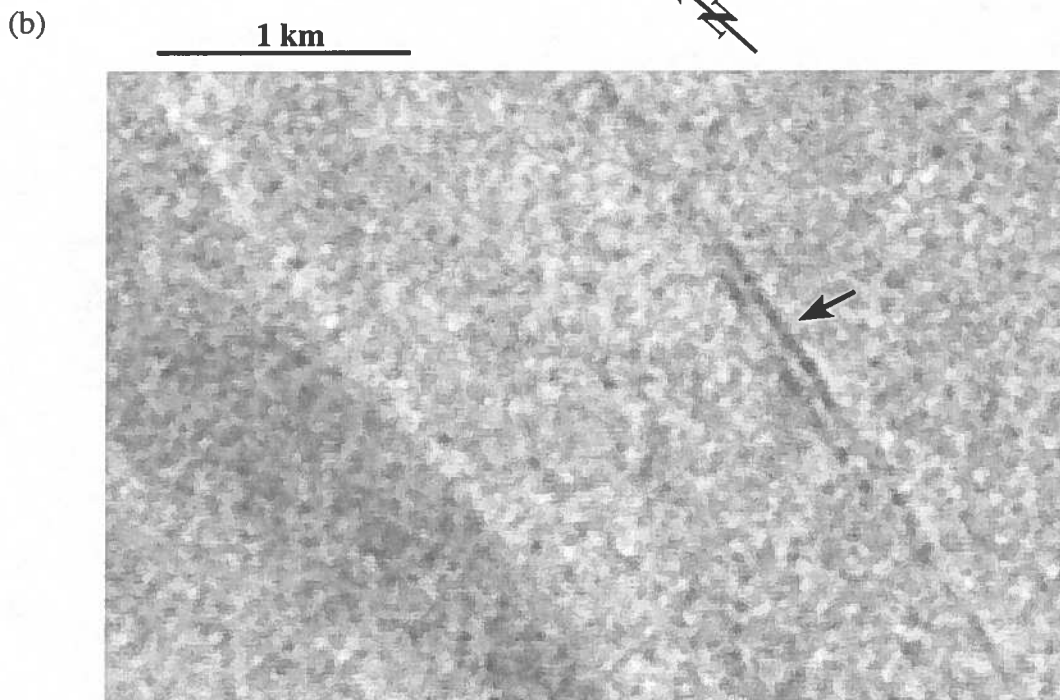
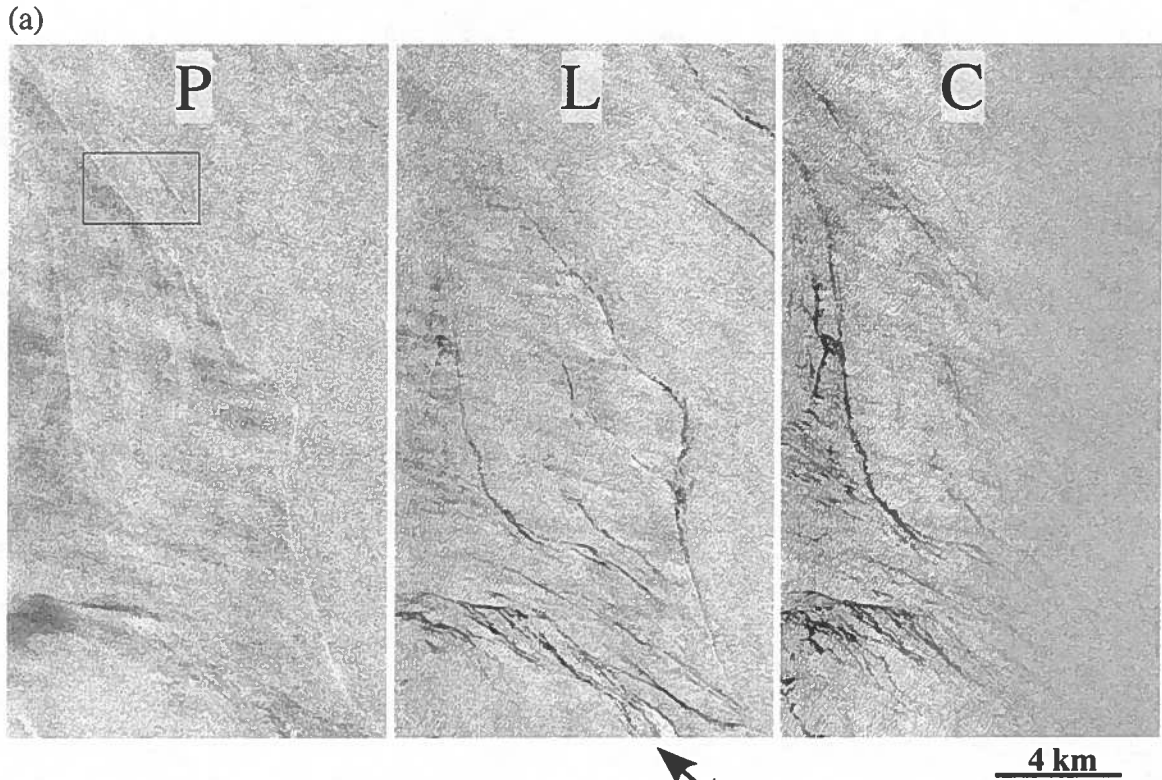


Figure 31. AIRSAR C, L, and P band images of V shaped part of cyclone, (a) P band shows lines of positive modulation co-located with lines of damping in C and L bands. Change in surface variance at the O(km) scale occurs abruptly at the bright line in P band. (b) Detail of P band bright structure showing a parallel ~100 m wavelength periodic structure (indicate by the arrow).

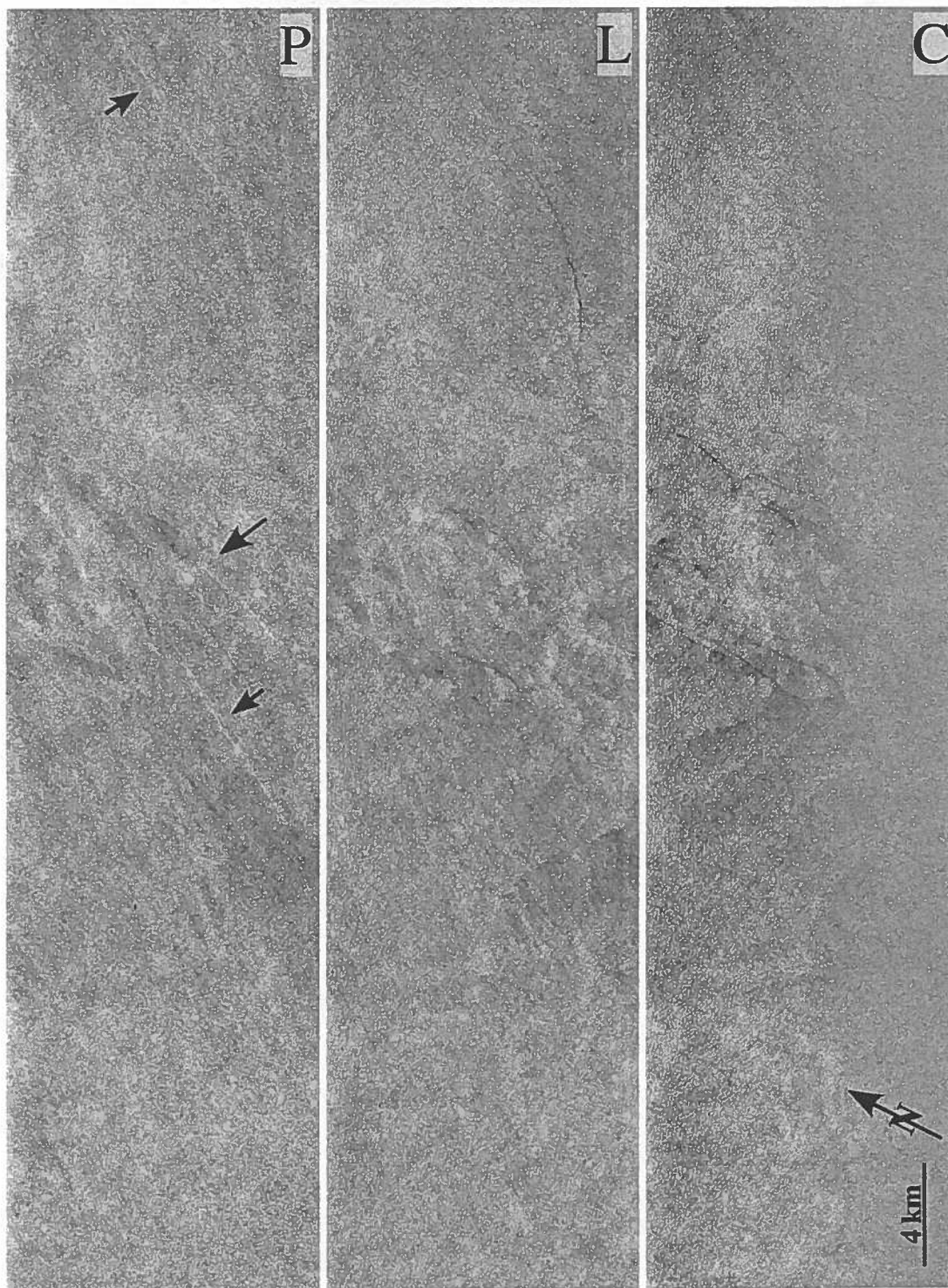


Figure 32. AIRSAR C, L, and P band images of the northern part of the hammerhead front, centered at 40.9°N 126.7°W. Several bright lines co-located and aligned with the surface thermal front are indicated by the arrows; the O(km) variation in backscatter increases to the west of the front indicated by the large arrow.

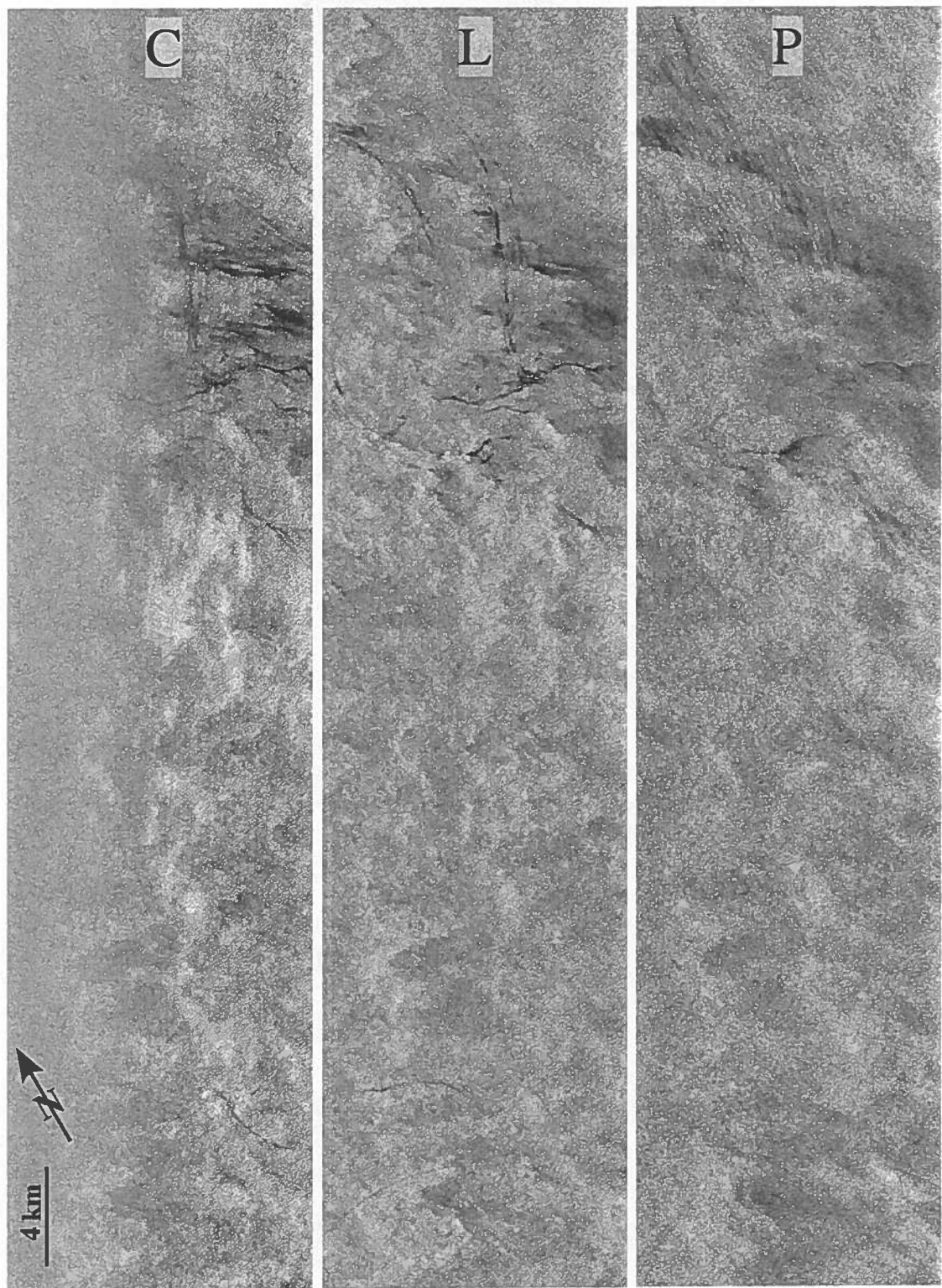


Figure 33. AIRSAR C, L, and P band images of the center part of the hammerhead front, centered at 40.4°N 126.7°W. Some periodic structure similar to that seen in figure 27, but of smaller wavelength, can be seen in P band.

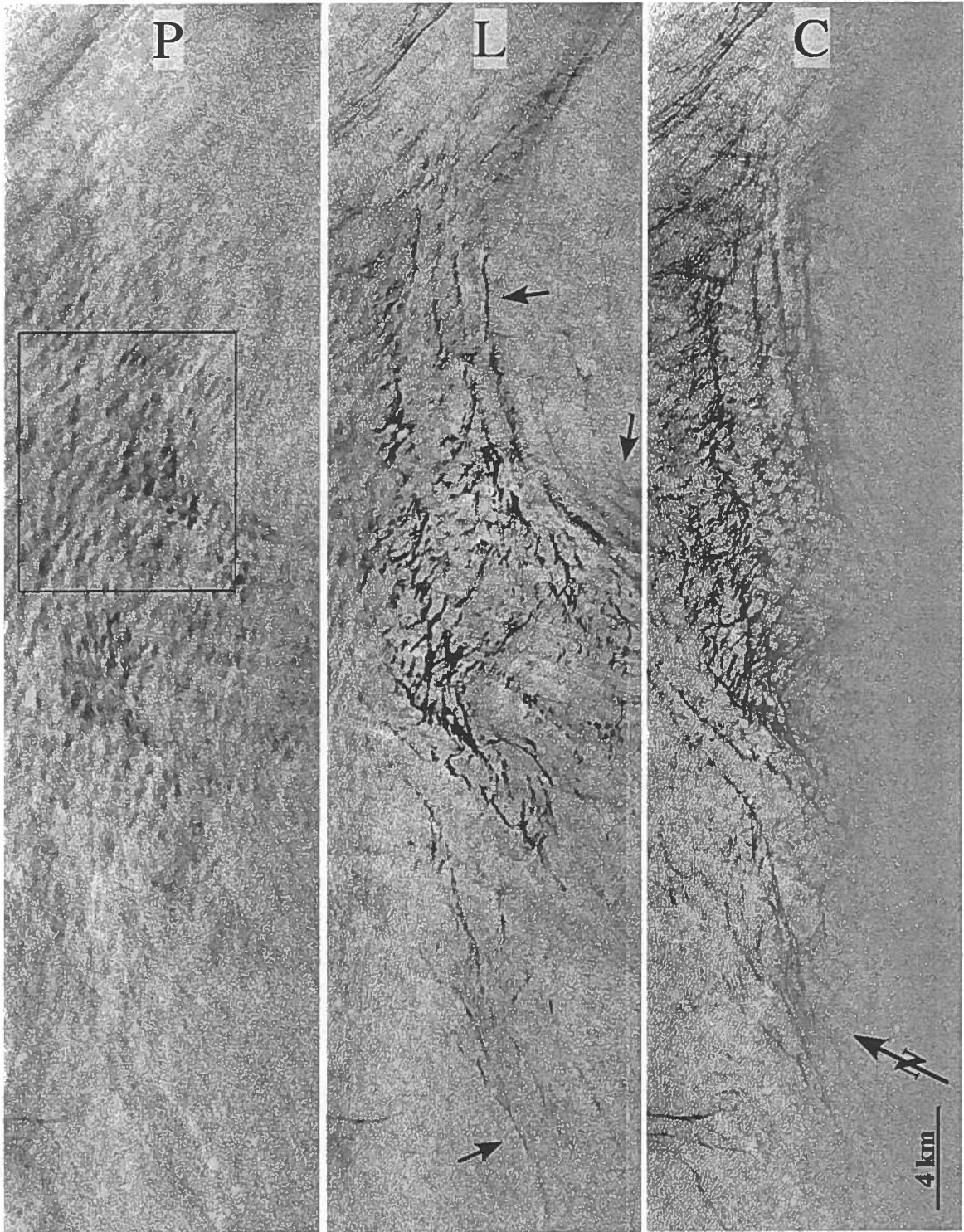
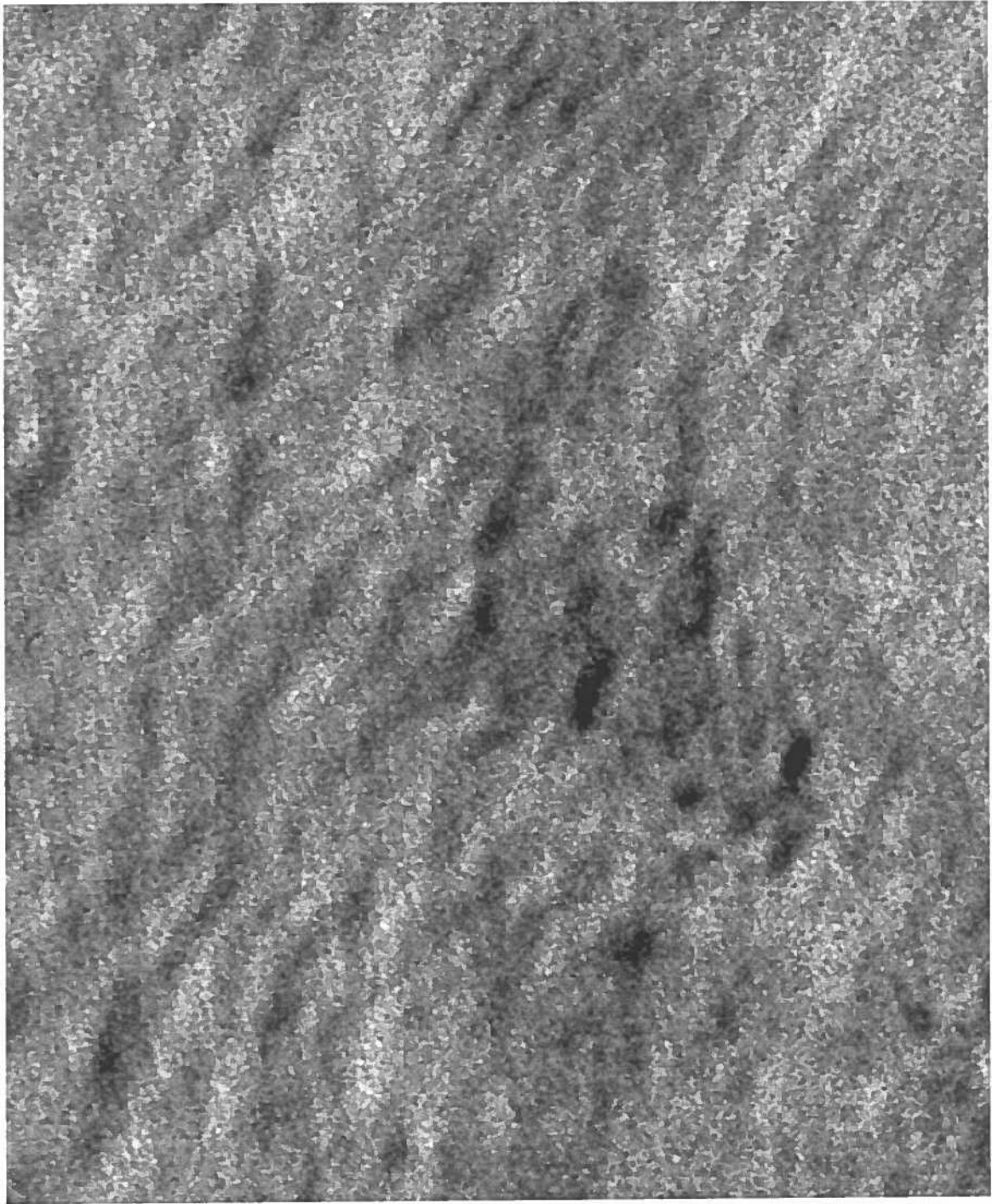


Figure 34. AIRSAR C, L, and P band images of northern branch of filament, centered at 41.1°N 126.3°W displaying $O(1\text{ km})$ periodic structure (indicated by arrows). Seven lines of regular spacing tend to indicate that this is internal wave generated as opposed to being slicks aligned by surface strain. The subtle N-S aligned variations are probably the signature of an atmospheric front seen in AVHRR visible images from the time of the SAR survey.



1 km



Figure 35. Detail of P band image of ~300 to ~500 m irregular periodic structure.

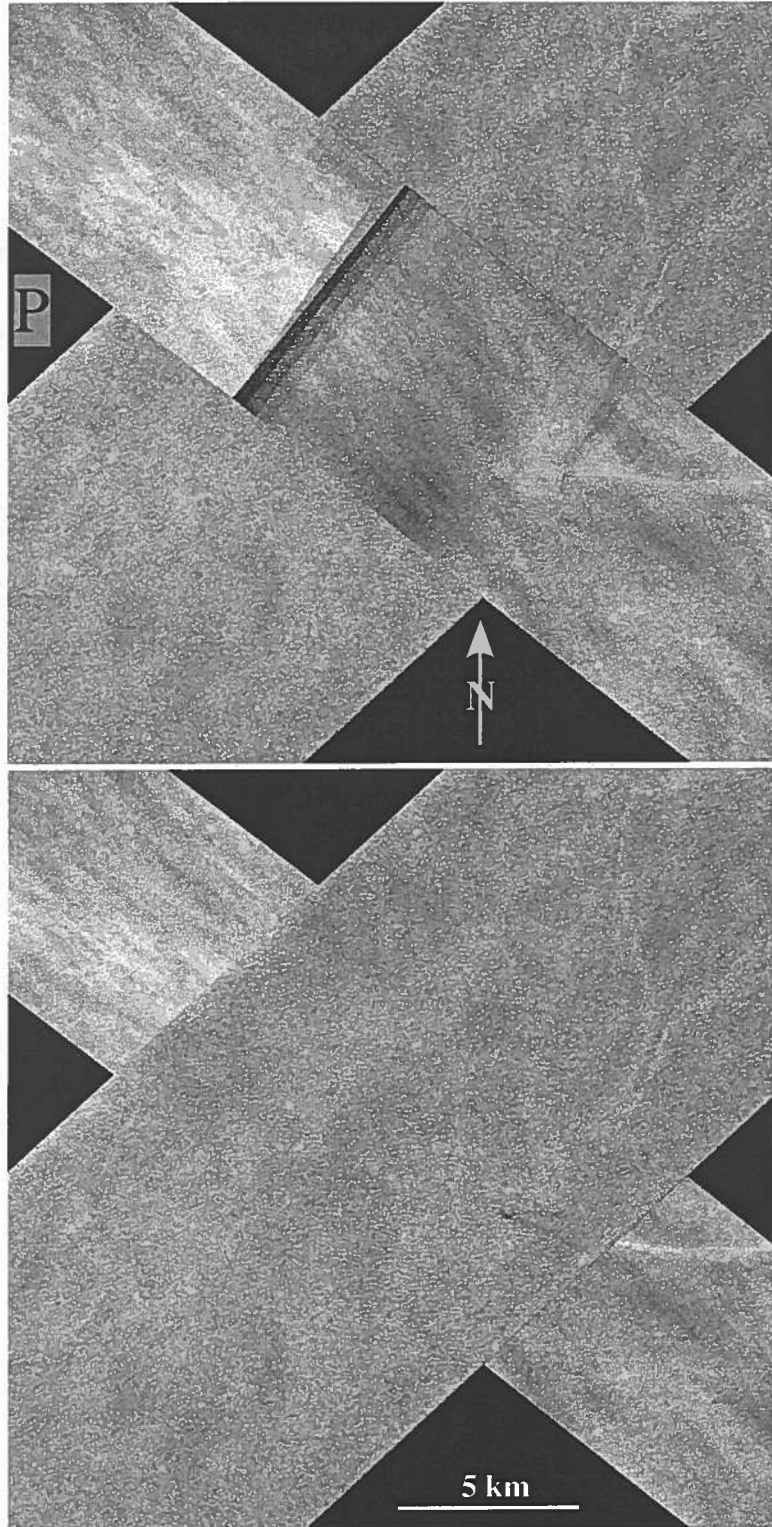
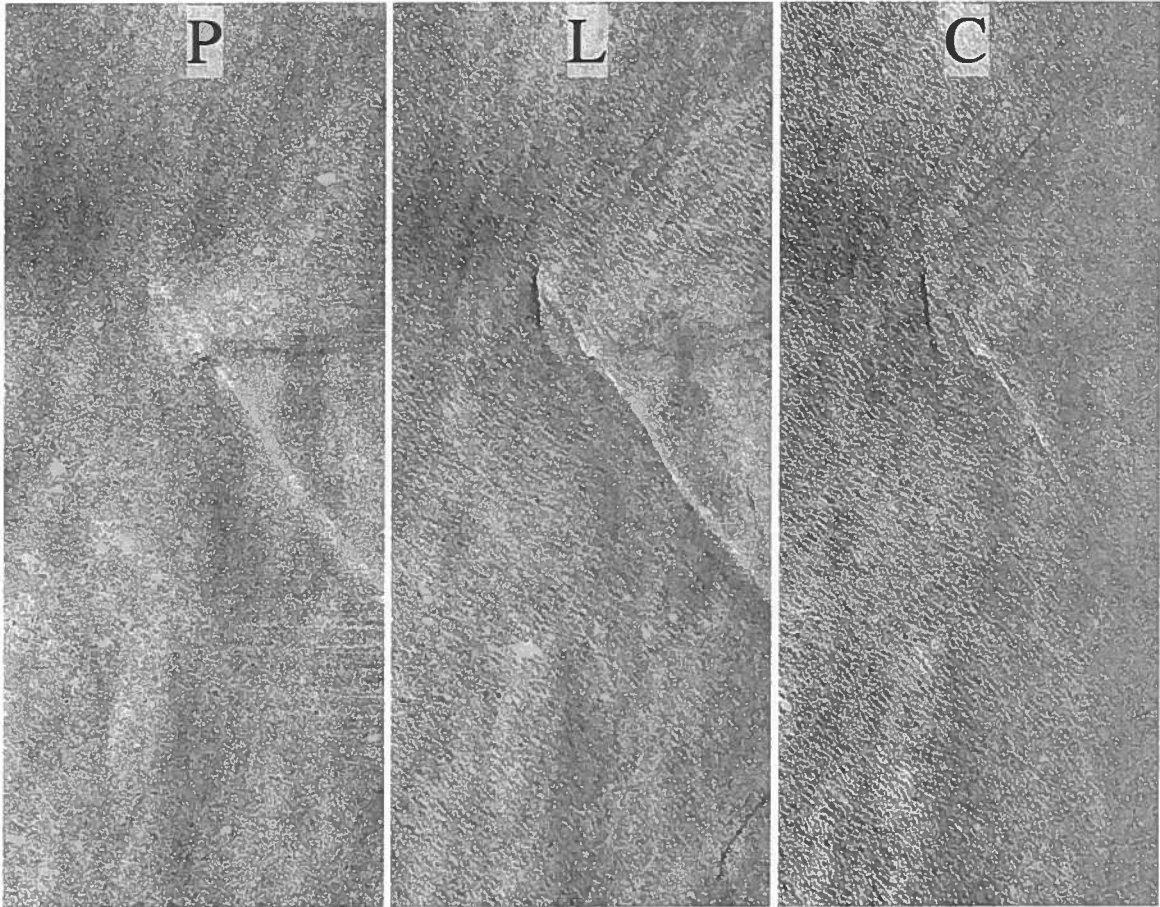


Figure 36. AIRSAR image crossing in P band showing a conjunction of linear structures. The angle dependence of the SAR imaging mechanism results in a change of sign in the illumination of image features for the two imaging angles.



2 km

Figure 37. The same conjunction of linear structures seen in figure 36, shown in all three bands.

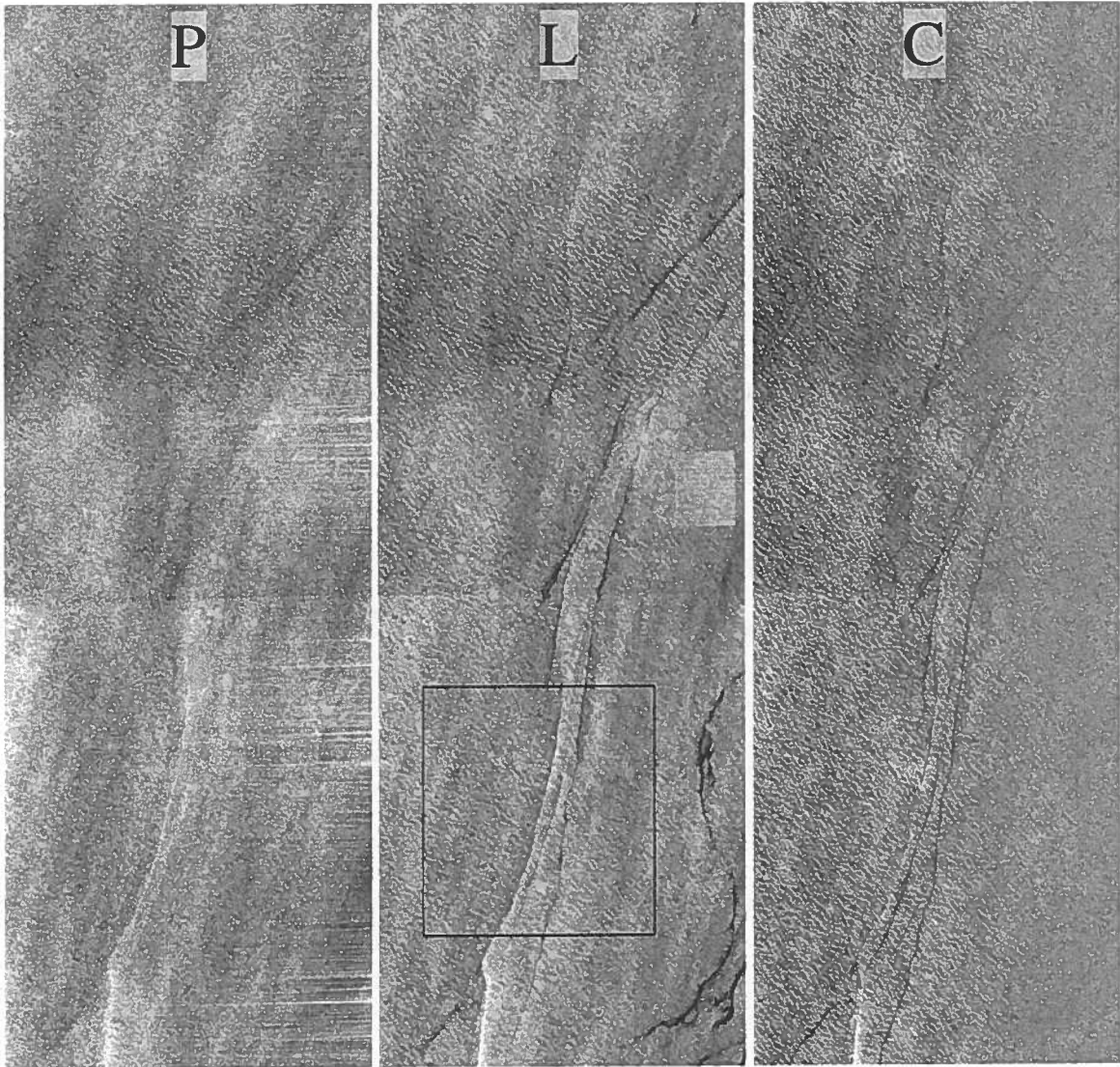


Figure 38. AIRSAR C, L, and P band images of beginning of the relatively continuous bright linear signature of core of the southern branch of the filament.

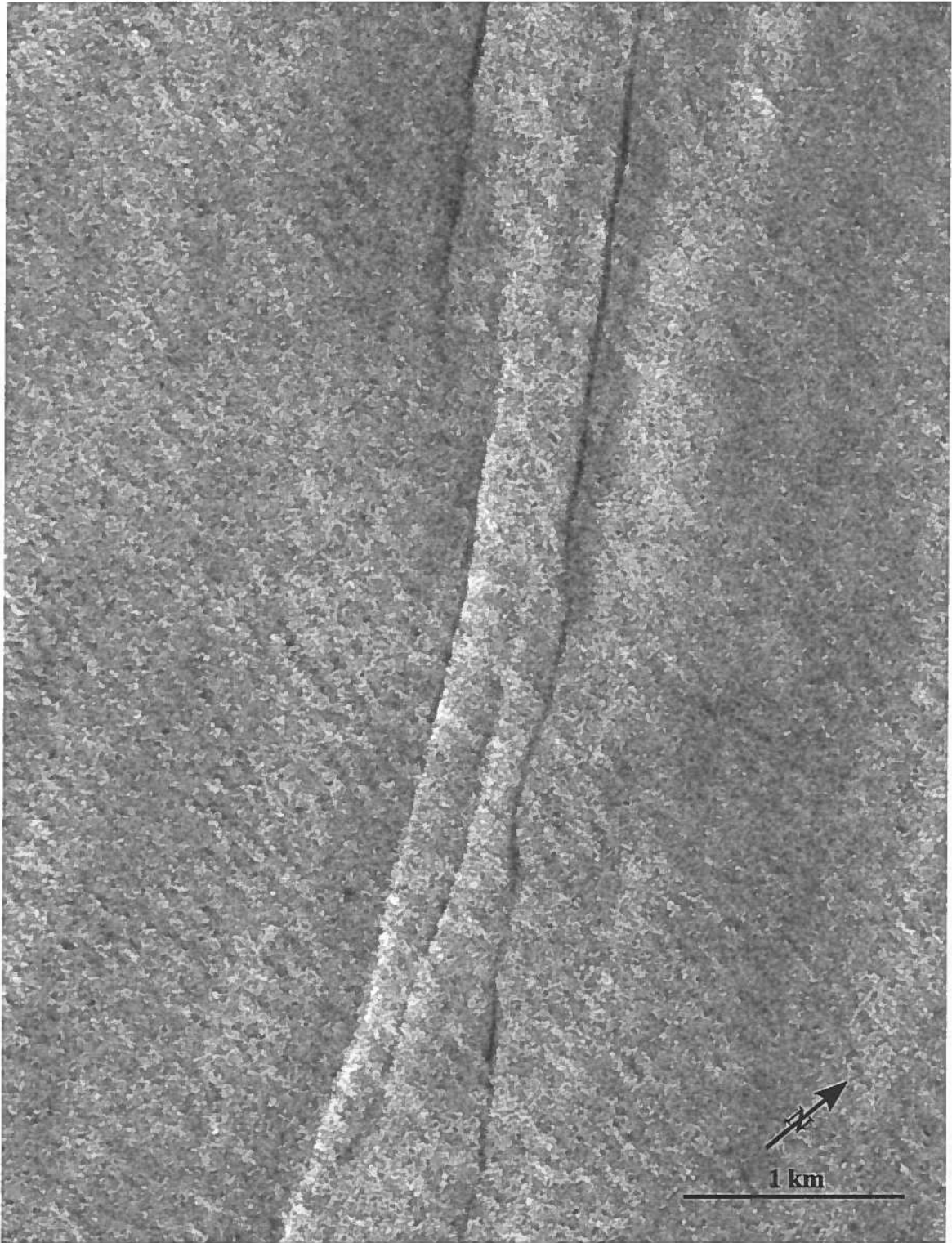


Figure 39. Detail of L band, figure 38, showing structure of parallel bright and dark lines, possibly indicating a succession of parallel fronts.

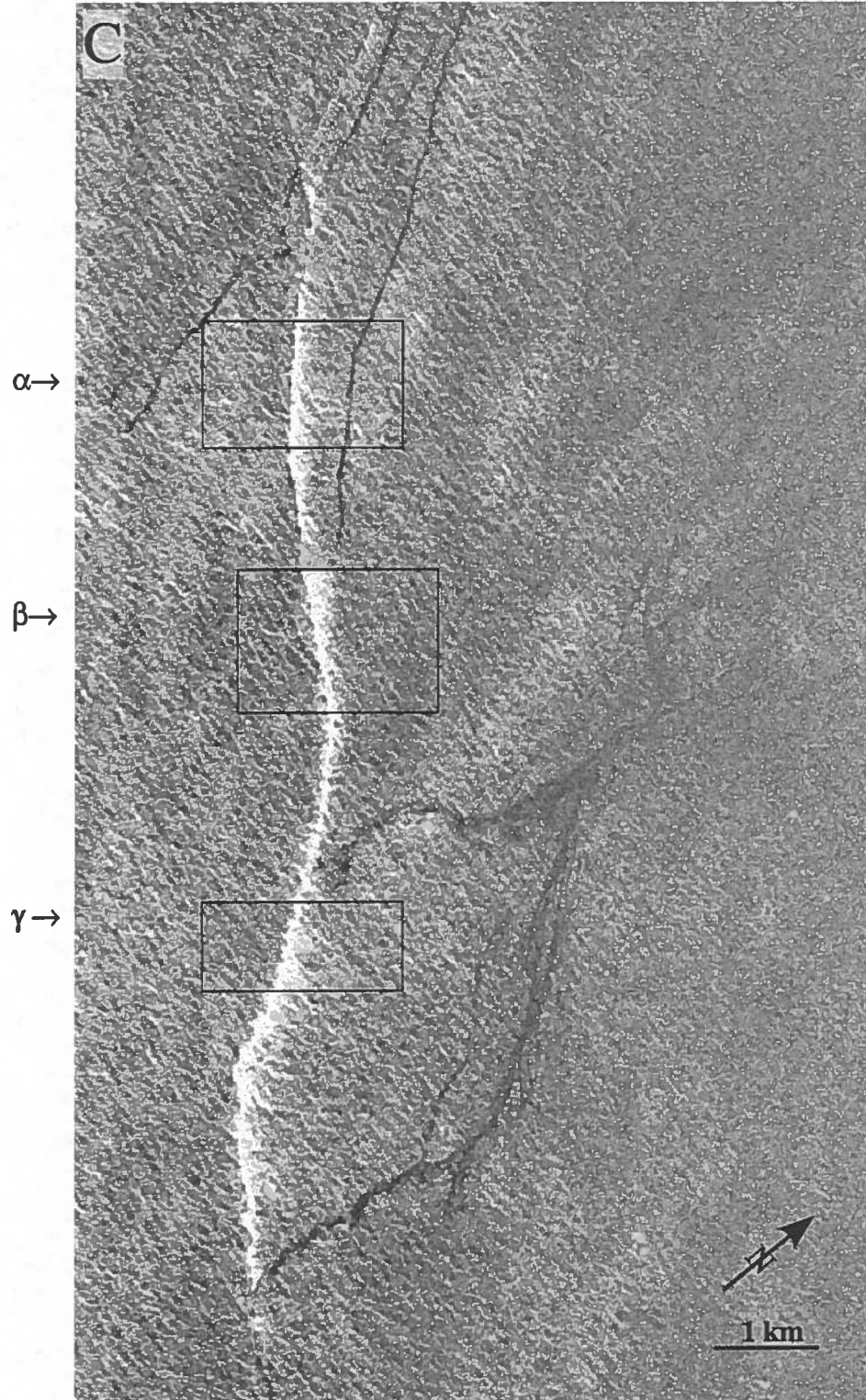


Figure 40. AIRSAR C-band image of southern branch of filament. Boxes indicate data used in computing the backscatter profiles shown in figures 51-53.

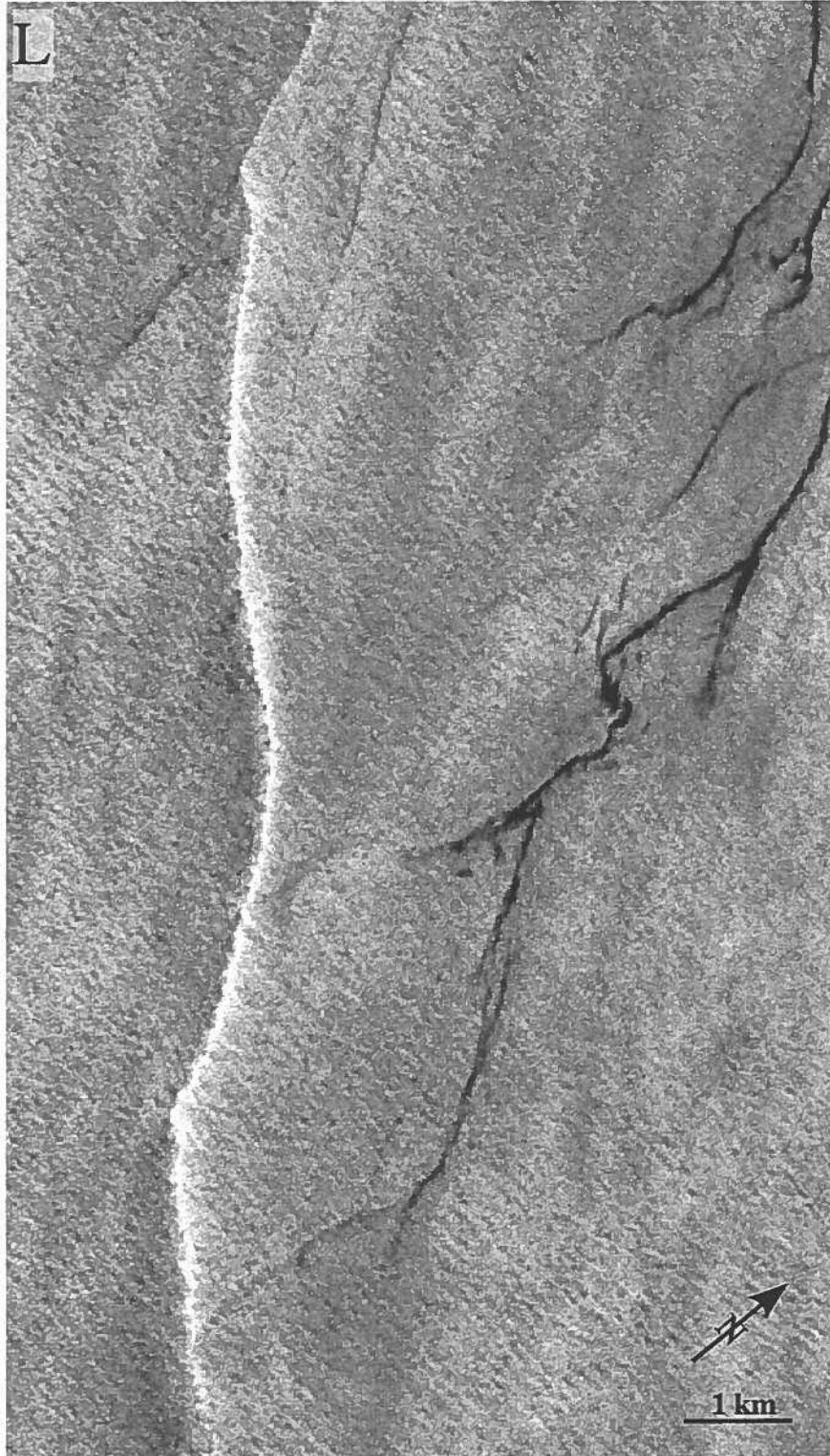


Figure 41. The associated L band image. The cell-like structure on the right hand side of this image, illuminated apparently through slicks, has two preferred orientations, the more north-west of which is shared by sections of the bright structure, suspected of being a geostrophic jet.

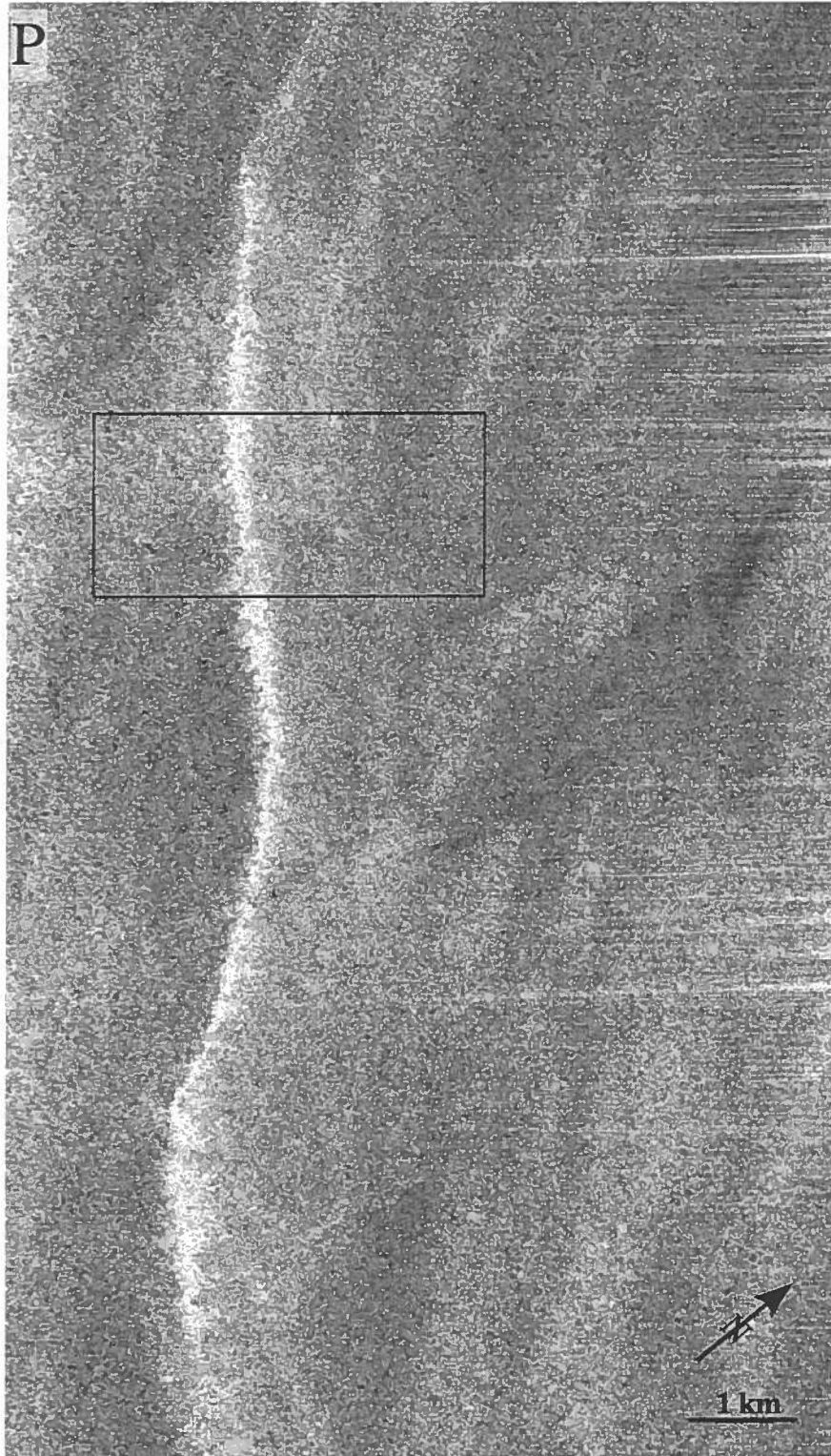
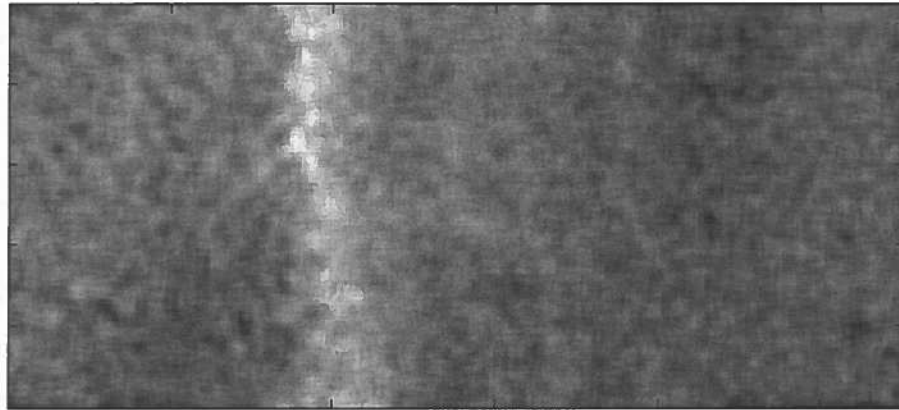


Figure 42. The associated P band image. The box indicates the region with periodic structure, detail shown in figure 43.

(a)



1 km

(b)

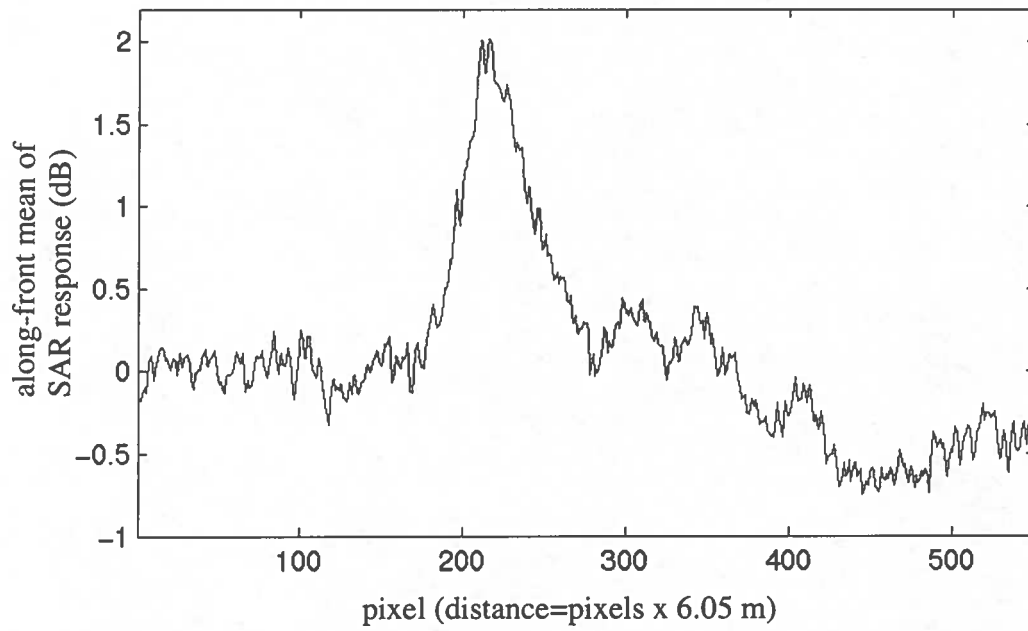


Figure 43. Jet associated periodic structure: detail of figure 42, (a) 9x9 boxcar filtered. (b) mean of raw data parallel to linear structure.

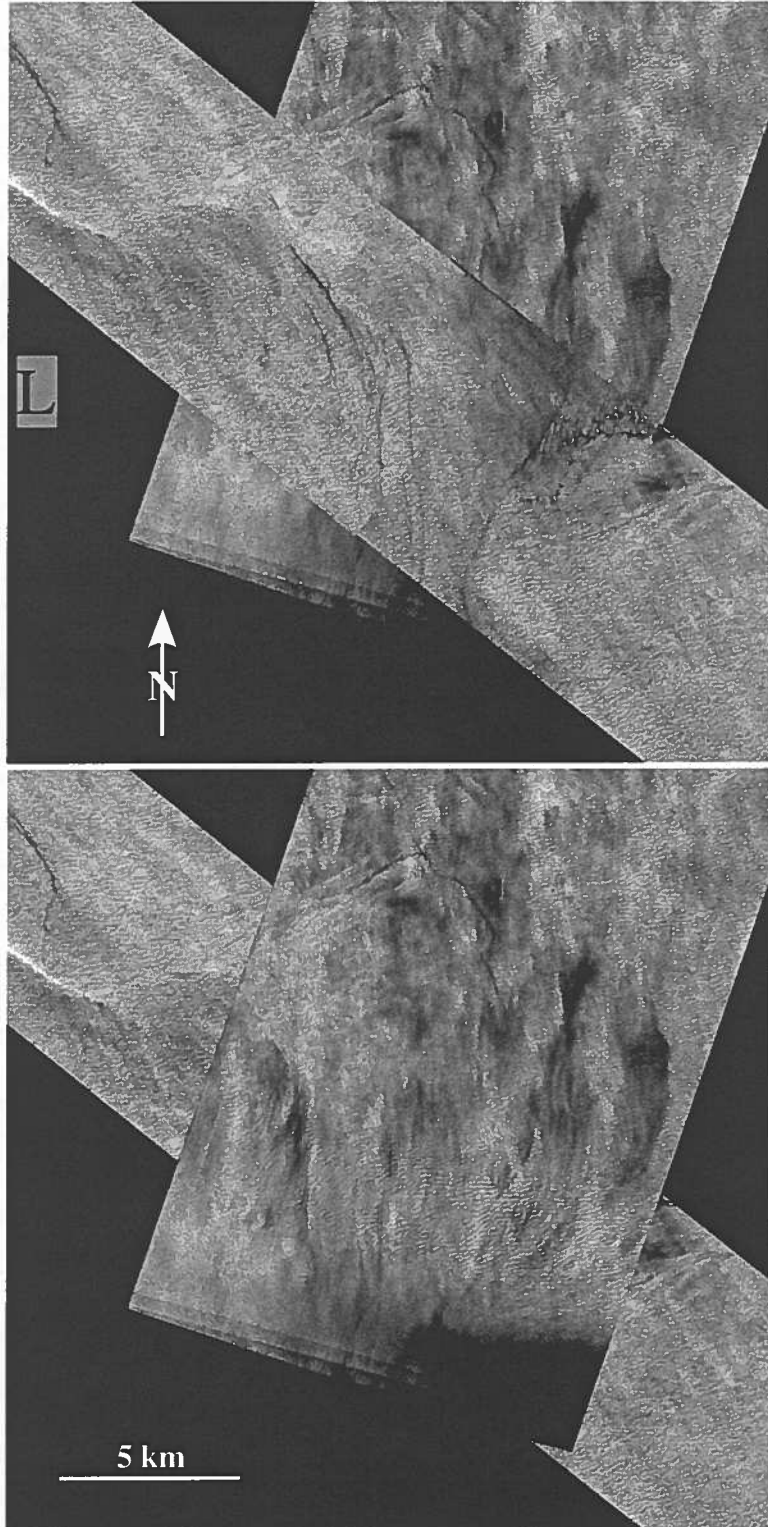


Figure 44. L band image crossing. In this and the following figure structures can be seen continuous across the two imaging angles. A curl shaped structure can be seen in the top image composite.

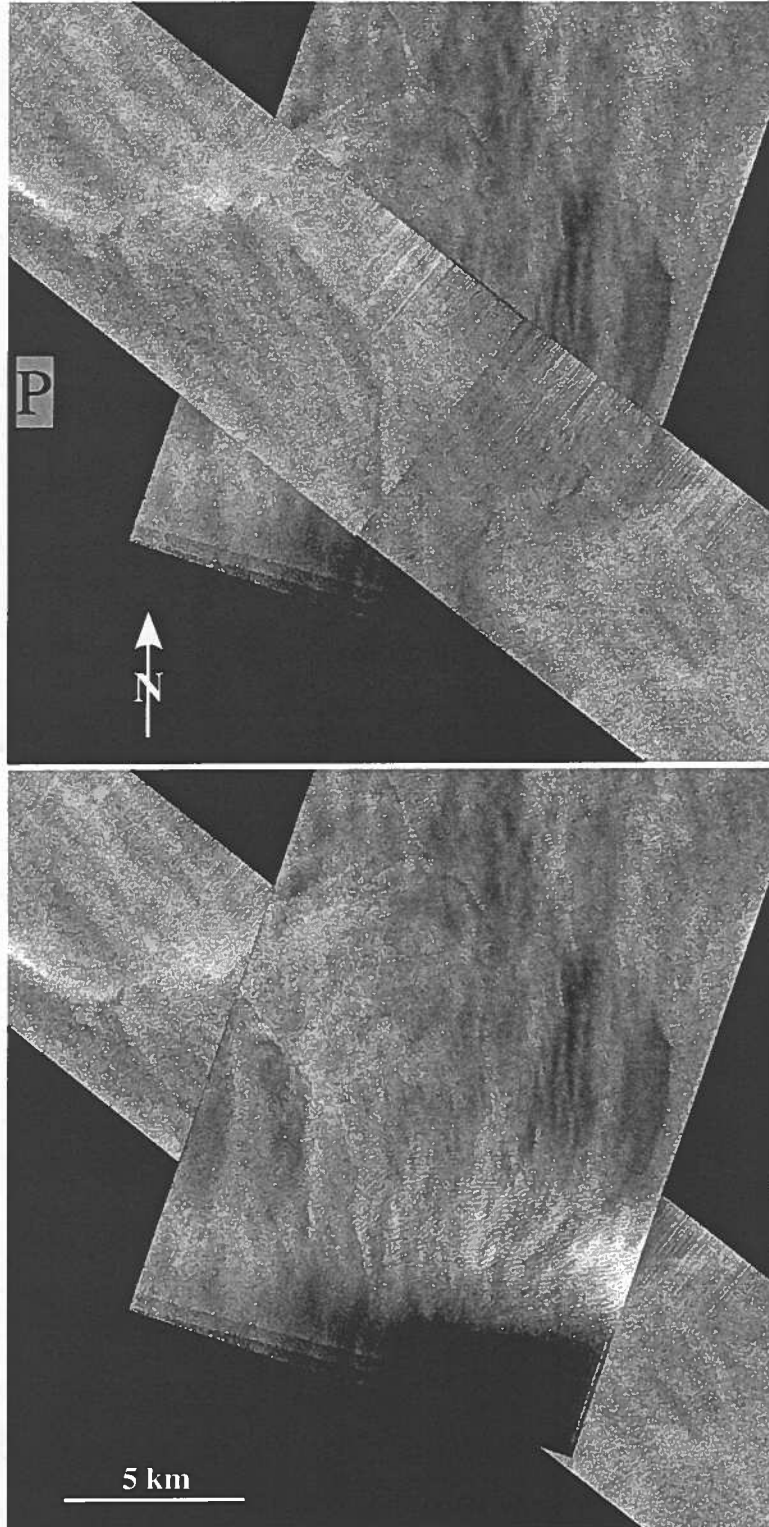


Figure 45. Same as in figure 44 except in P band. $O(d_{\text{mixed layer}})$ texture similar to that in the core near the suspected gust front (see figure 26) can be seen.

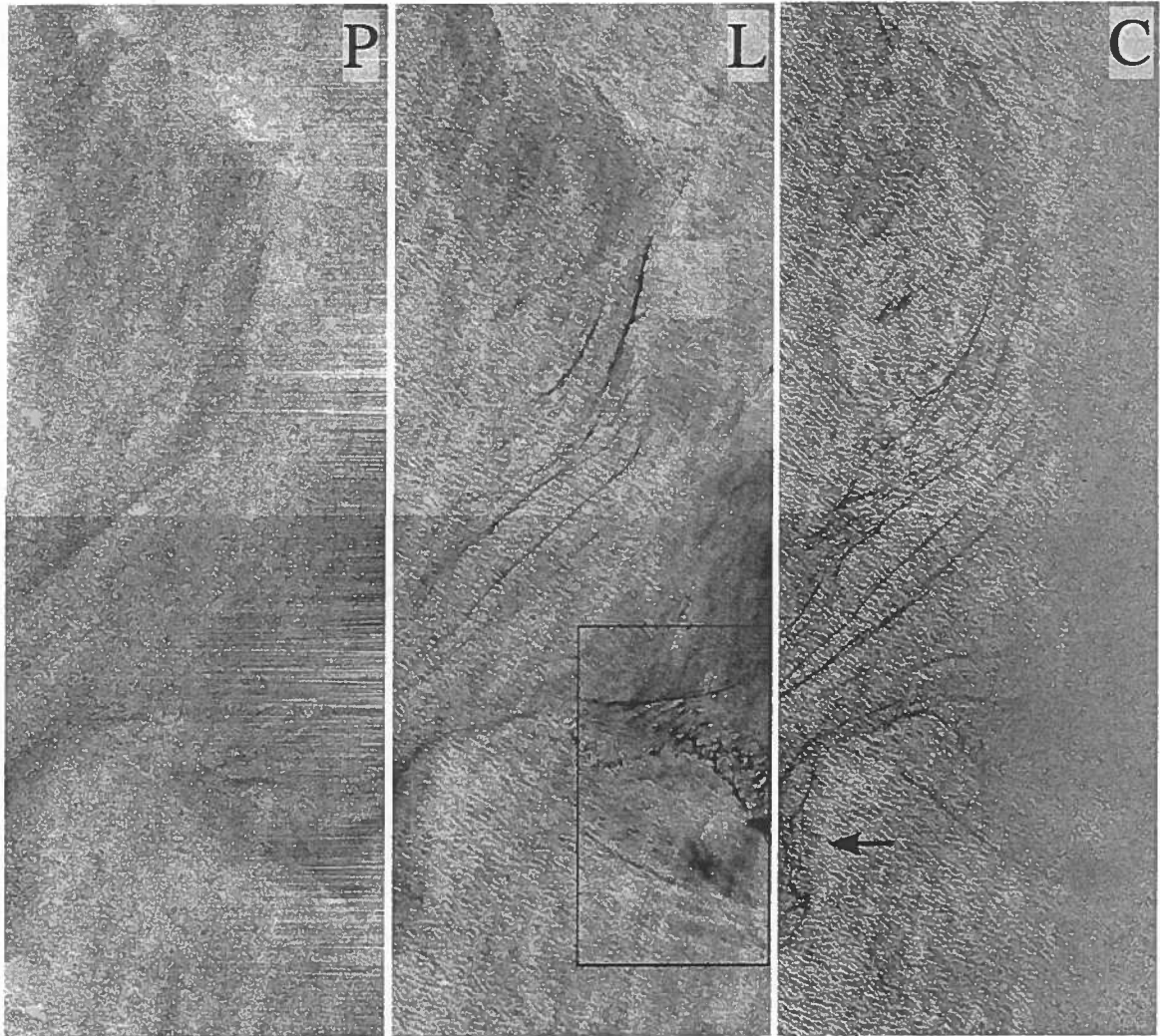


Figure 46. AIRSAR C, L, and P band images of the ending of the relatively continuous structure in the southern branch of the filament. The same curl shaped structure seen in figures 44 and 45 can be seen in all three bands. The arrow in the C band image points to a periodic structure ($\sim 3\lambda$) near the tip of the curl.

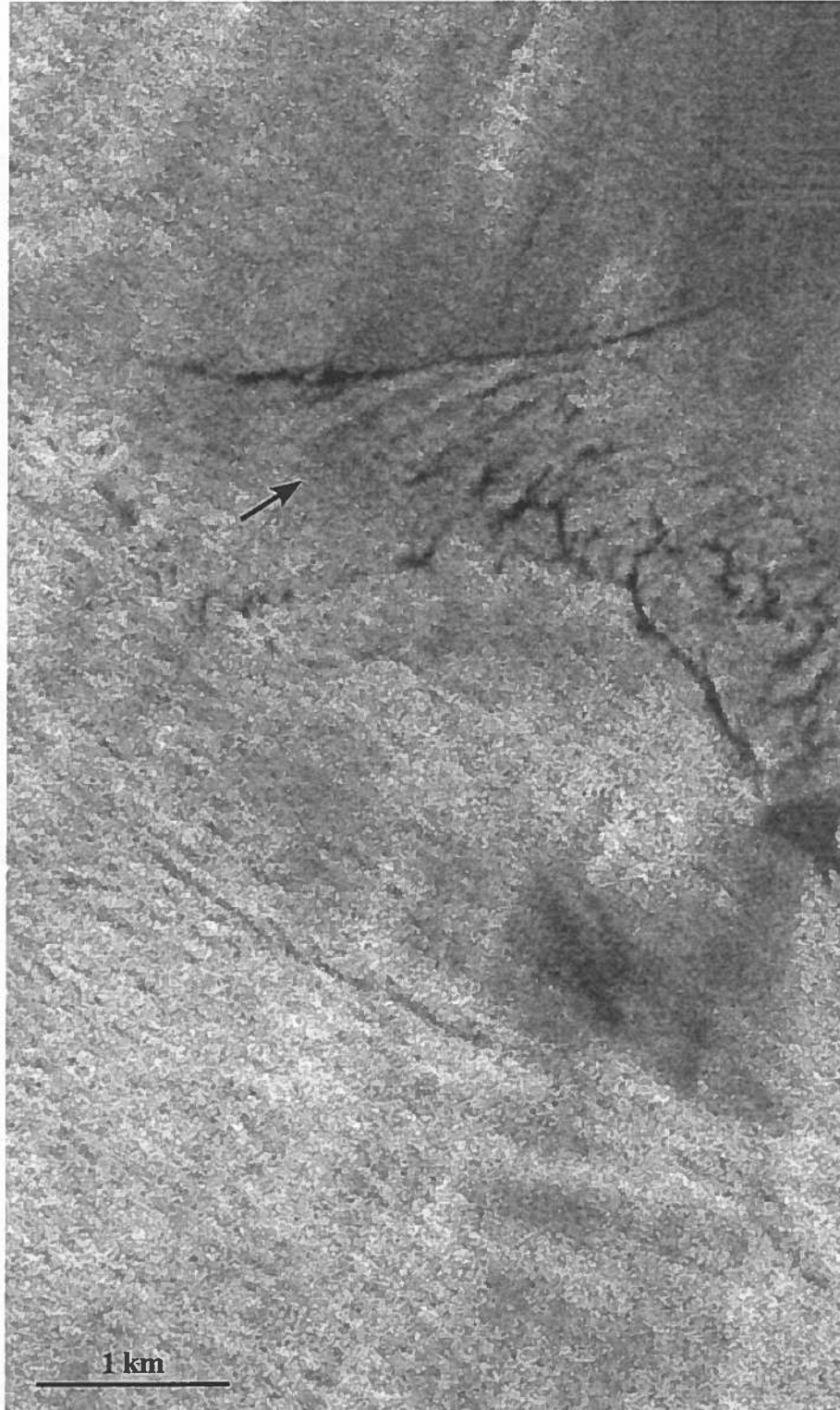


Figure 47. Detail of the curl structure in L-band. Periodic structures of ~ 220 m wavelength are indicated by the arrow.

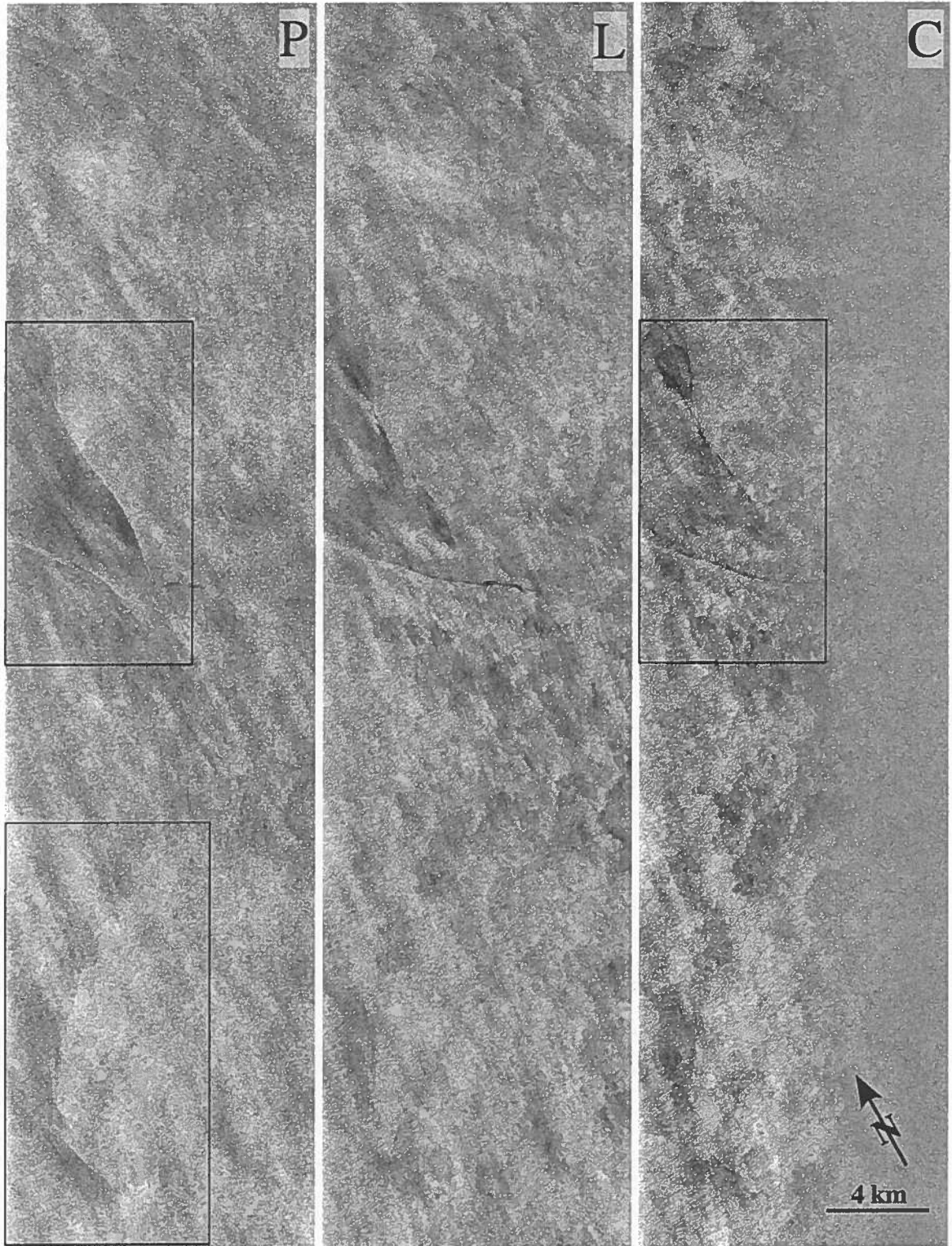


Figure 48. The region near the end of the southern branch, in C, L and P bands. A second curl can be seen in P band.

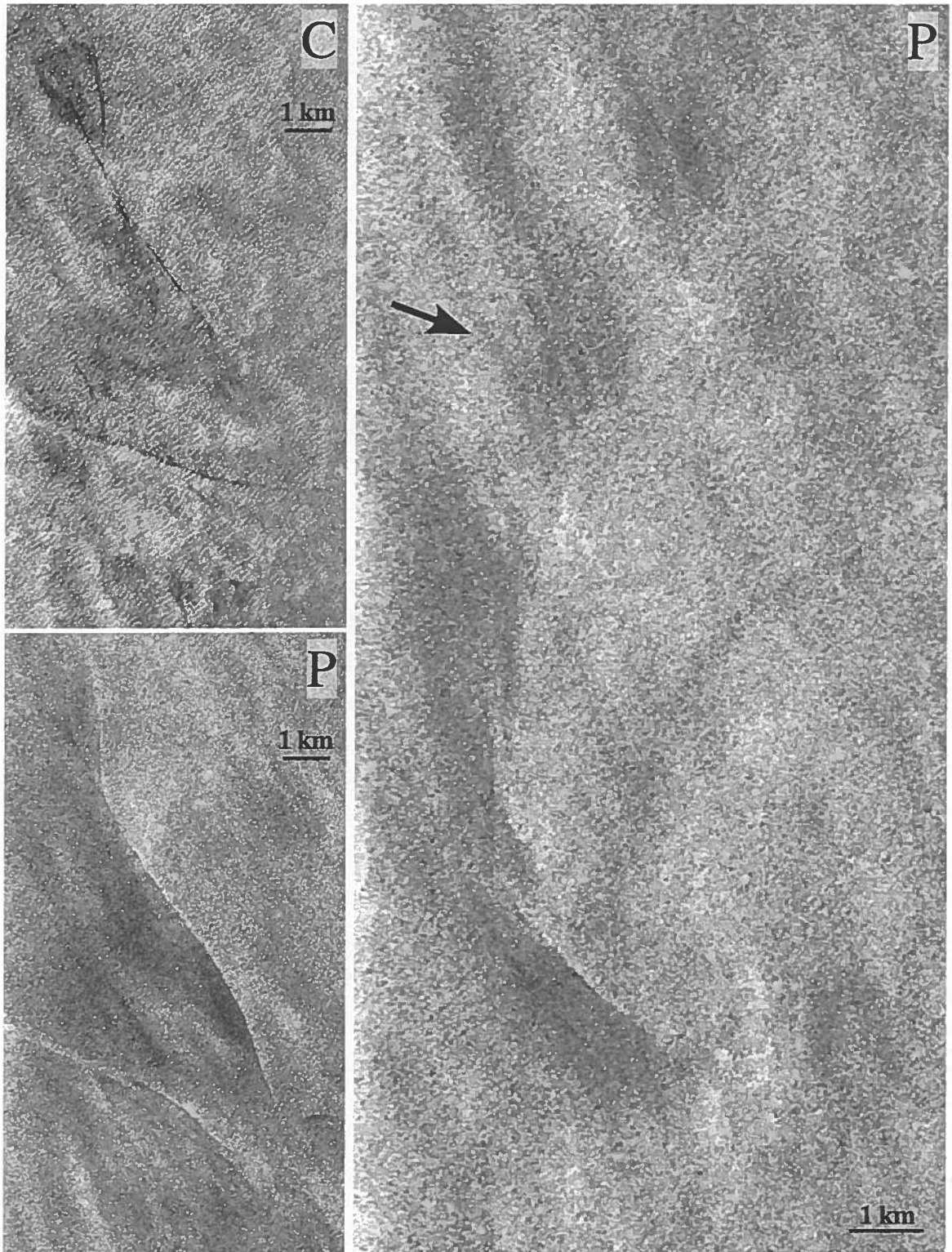


Figure 49. Details of second curl in C and P bands. The arrow points to a periodic structure ($\sim 4\lambda$) associated with the curl.

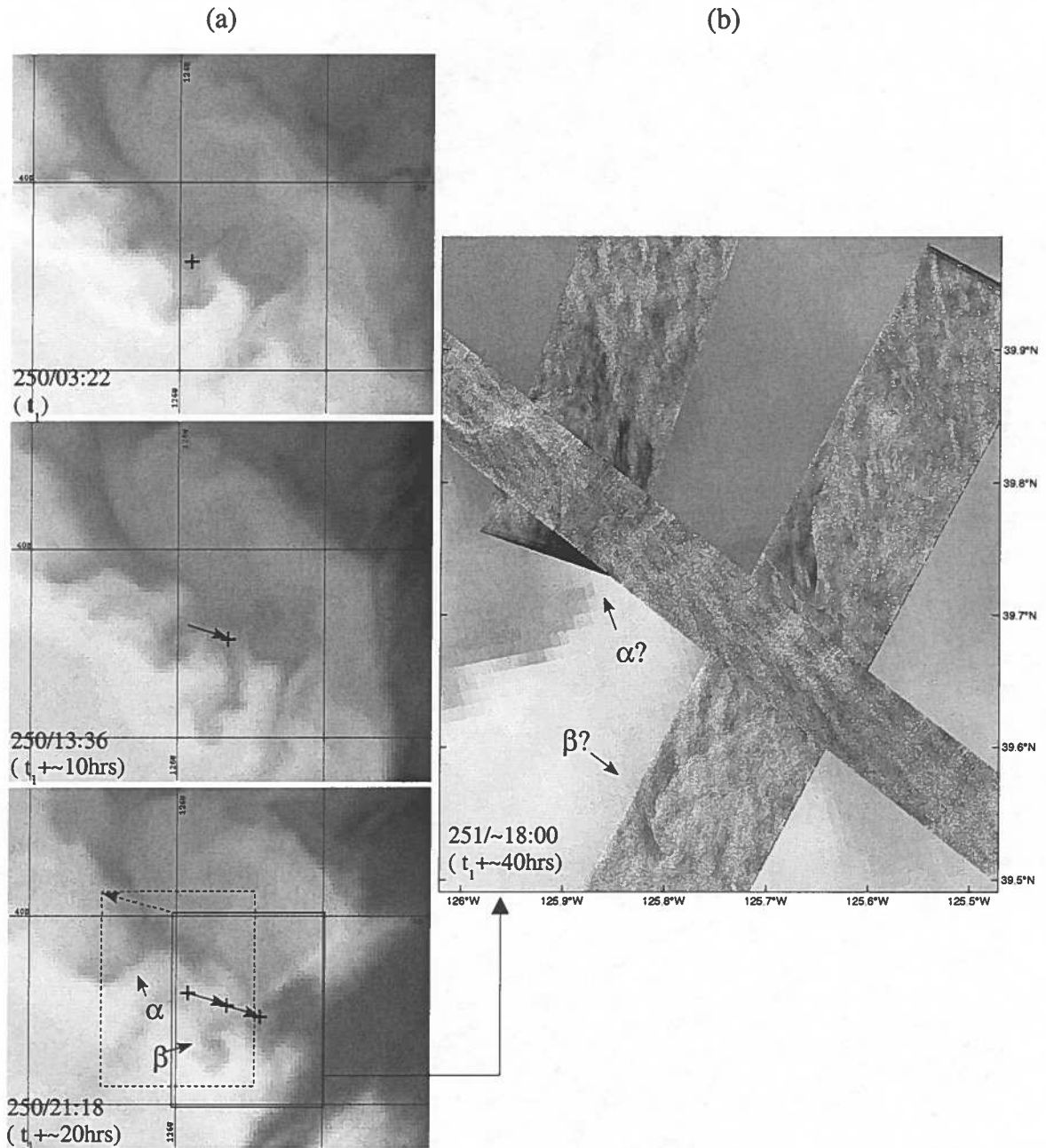


Figure 50. SAR images of curls. (a) AVHRR channel 4 time series showing curl propagation/advection. The "+" sign indicates the moving axis of the "Y" shaped region of cool water. The solid outline box represents the region imaged in (b). (b) P band image of curls, the dotted outline box in (a) represents the extrapolated region associated with this image.

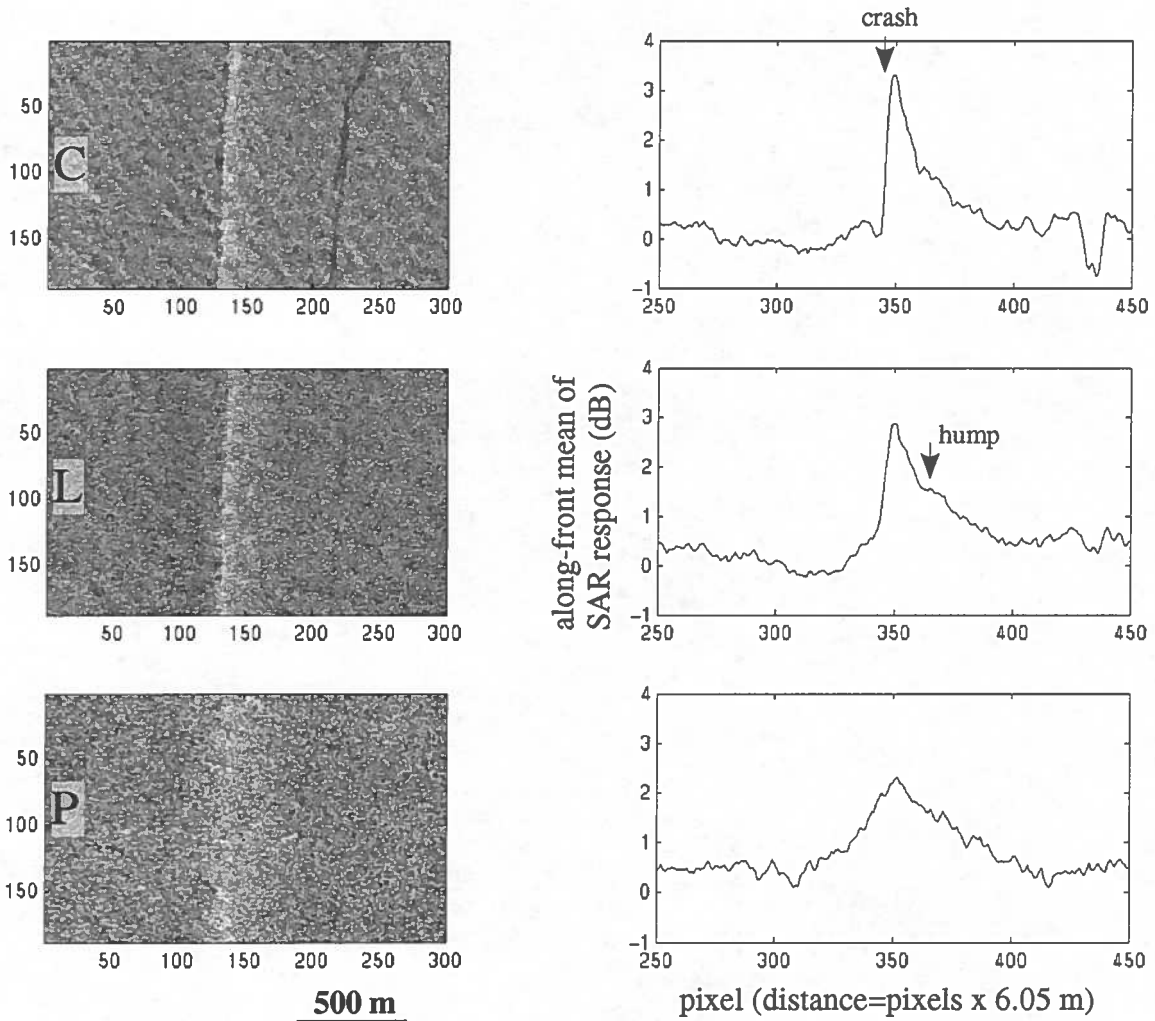


Figure 51. SAR jet profiles for region α .

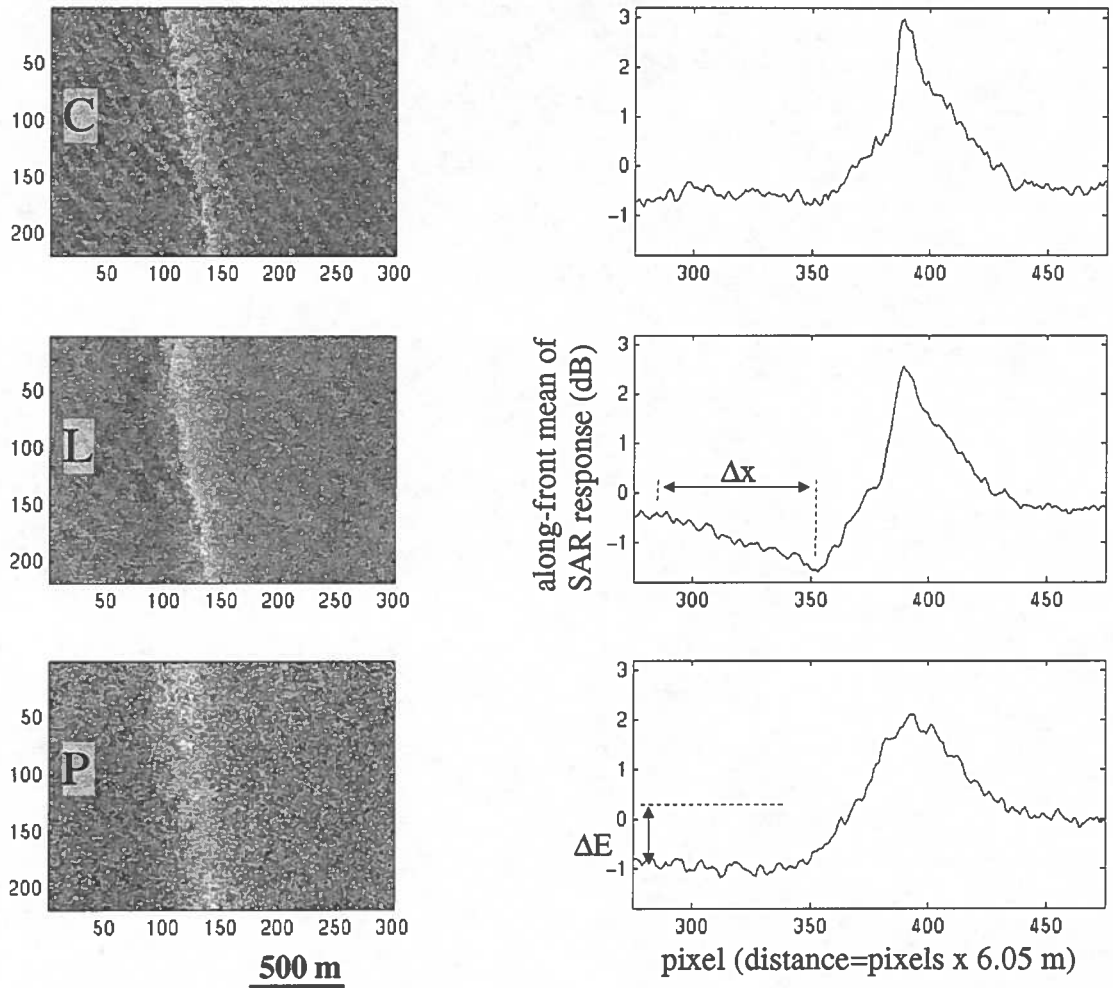


Figure 52. SAR jet profiles for region β . ΔE represents the leeward reduction in energy at the P band Bragg wavelength. Δx indicates the L band Bragg wavelength regeneration distance.

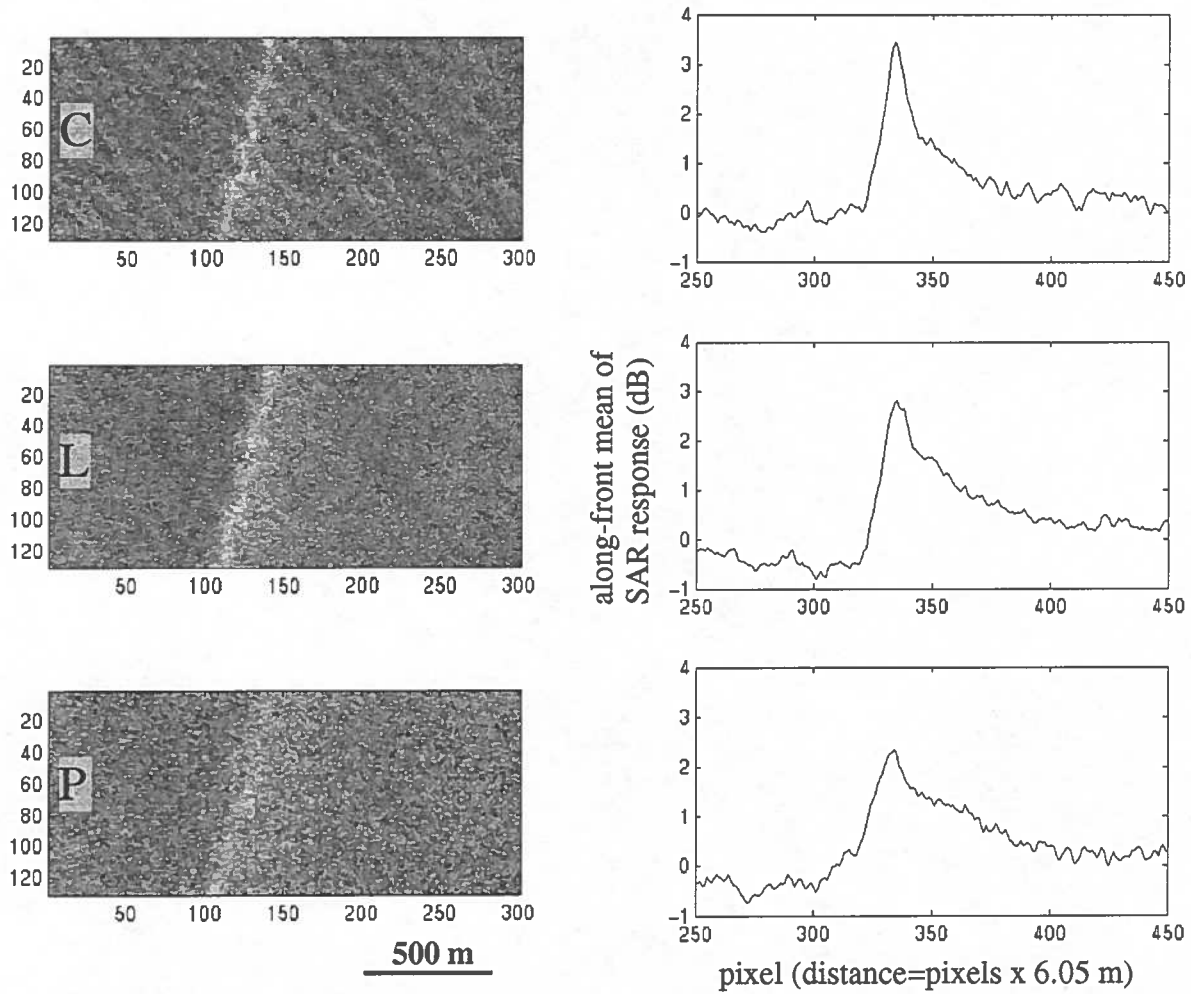


Figure 53. SAR jet profiles for region γ .

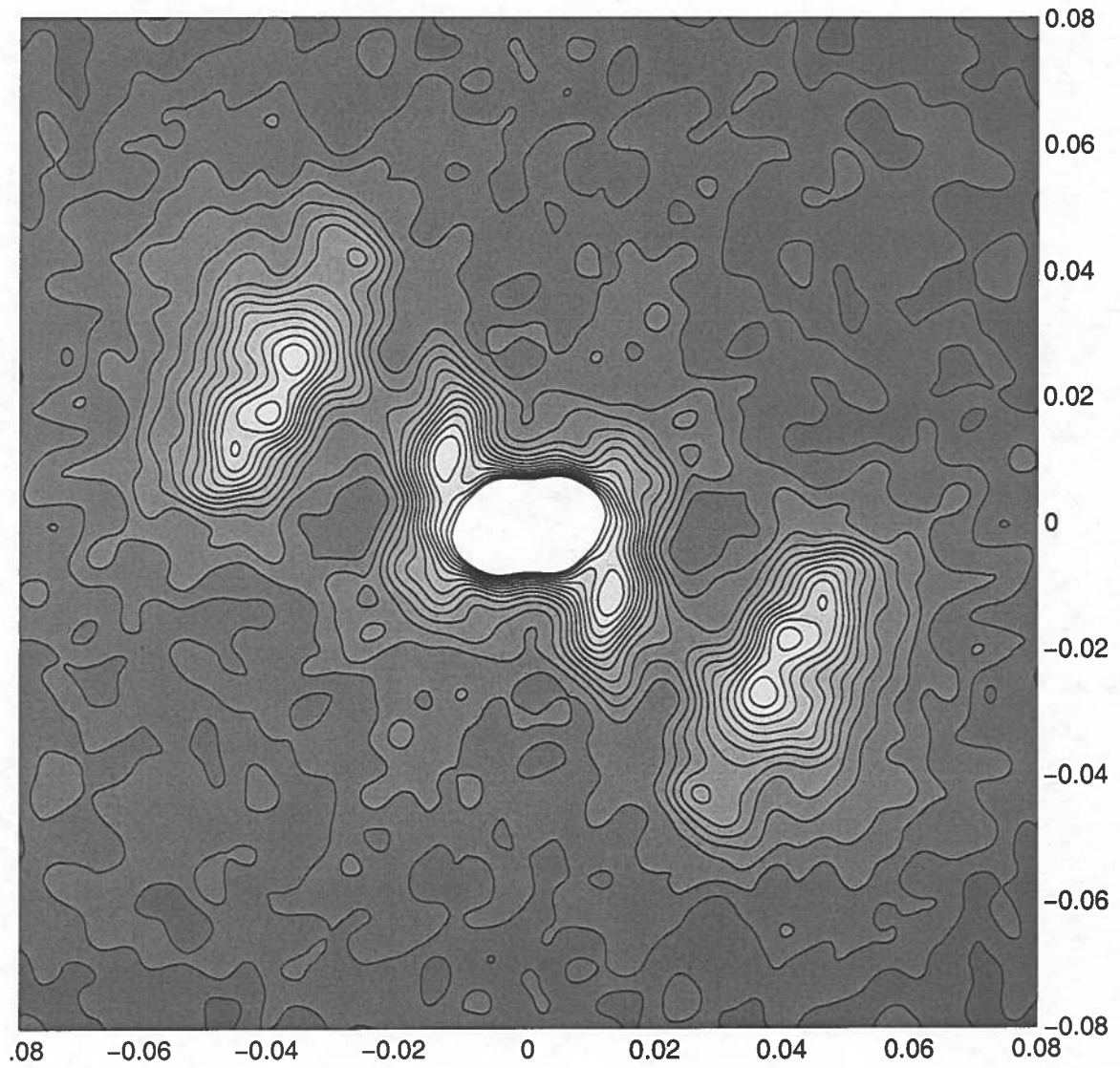


Figure 54. SAR L band derived long gravity wave spectrum. This spectrum was FFT derived using from an area of $\sim 12 \times 48 \text{ km}^2$ centered at $40.0^\circ\text{N } 126.5^\circ\text{W}$ and is representative of the swell signature of the entire northern region.

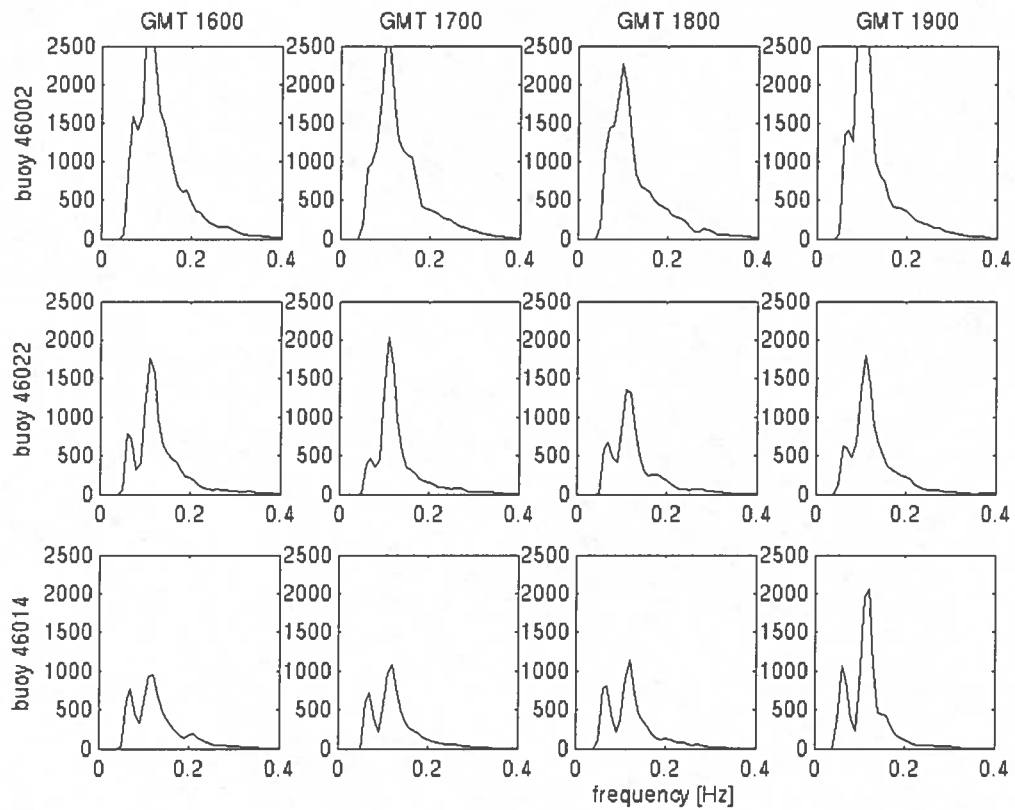


Figure 55. Wave energy from the time of the SAR survey GMT1600-1900. The ~ 9 s (~ 140 m) peak corresponds to swell generated through the ~ 10 m/s winds of the North Pacific Subtropical Gyre. The absence of a proper storm source for direct generation suggests that the ~ 15 s (~ 370 m) peak corresponds to infra-gravity waves arising from the spread in the ~ 9 s peak.

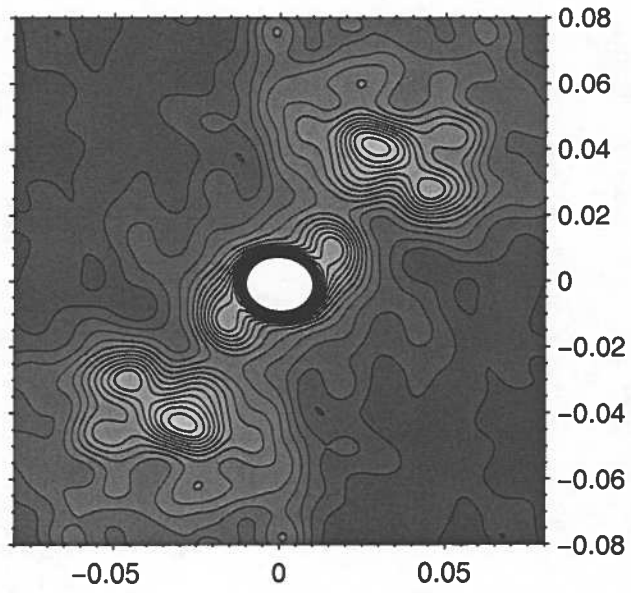
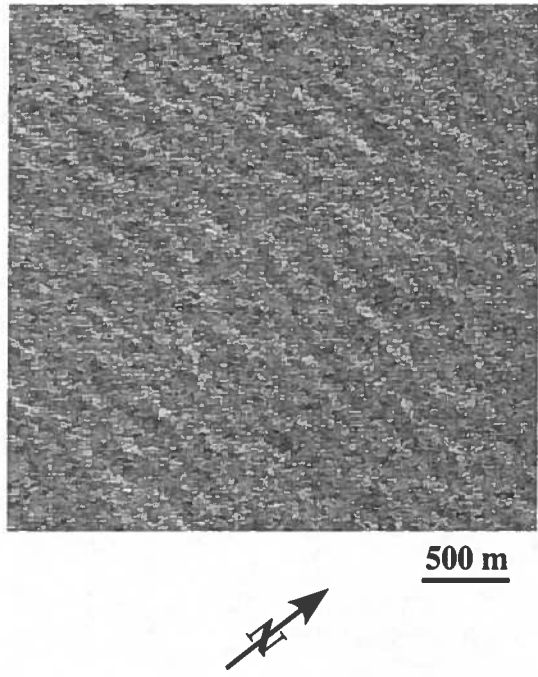
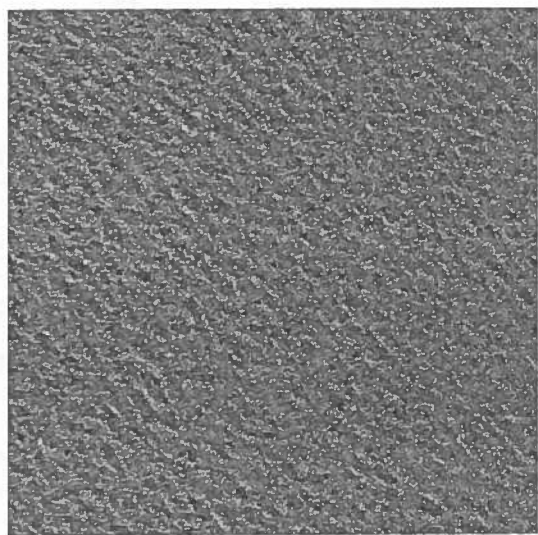
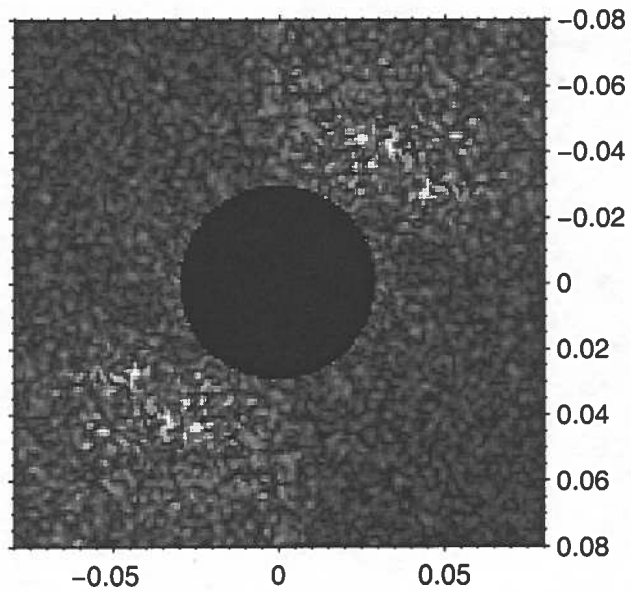
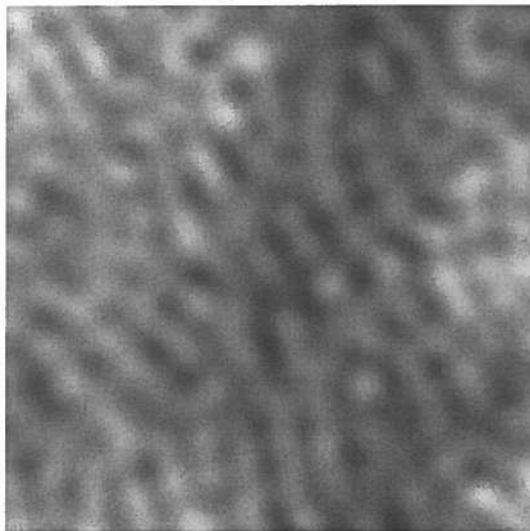
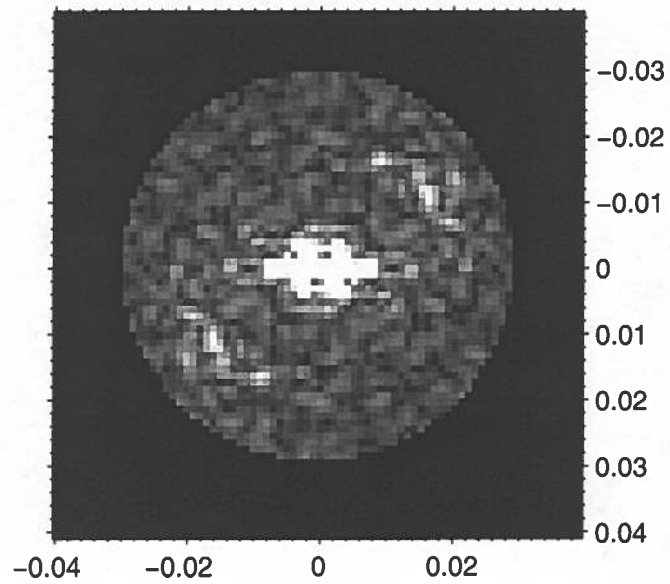


Figure 56. SAR L band derived long gravity wave spectrum. (a) Detail of SAR L band. (b) FFT of an area of $\sim 6.2 \times 6.2 \text{ km}^2$ centered at $39.6^\circ\text{N } 125.7^\circ\text{W}$; the SAR image in (a) shows one quarter of the region used to derive the spectrum in (b).



500 m

Figure 57. High-pass filtered SAR image. (a) FFT derived spectrum (used to create the contour plot in figure 56) with low wavenumber part negated and (b) filtered spectrum derived image. Gravity waves of wavelength ~140 m are visible.



500 m

Figure 58. Low-pass filtered SAR image. (a) FFT derived spectrum (used to create the contour plot in figure 56) with high wavenumber part negated and (b) filtered spectrum derived image. Gravity waves of wavelength ~ 370 m are visible.

CHAPTER 6

DISCUSSION: INFERRING JET STRUCTURE FROM MULTIBAND SAR PROFILES

Within the cold upwelled waters of a filament rooted near Point Sur California in 1985, lying between warm surface waters and waters of intermediate temperature, Flament and Armi (2000) observed a ~ 1000 m width jet and measured, using ship drift (80 meter resolution), a core velocity ~ 0.8 m/s, and cross-isotherm convergence associated velocity of ~ 0.075 m/s. Thus convergence was roughly one-tenth of the along-jet velocity. A line of debris was observed, indicating a change of sign in cross-jet velocity. The co-located jet velocity peak and debris line were approximately one kilometer from the sharpest measured anti-cyclonic surface temperature/density front (the horizontally offset surface manifestation of the integrated depth structure determined geopotential anomaly that this jet would be associated with). The imaged "jet" from which profiles were derived was of similar placement within a filament and had a similar inferred width with and inferred jet velocity peak associated convergence.

Assuming our study jet had a similar rate of convergence to that found by Flament and Armi (2000), then velocity imaging effects are small. From equation 10, with a range distance of 10 km, and aircraft velocity of 200 m/s, the influence of MTF_v will be an azimuthal smearing of ~ 3.75 m, or $\sim 1/2$ of the pixel scale. Even if the effect of MTF_v were significant due to an anomalously high rate of convergence, the resultant smearing would be along-jet, and would not significantly affect the interpretation of the SAR

profiles for the nearly azimuthal jet segments which the following study focuses on.

Smearing due to along-jet velocity is insignificant for region α , and small for regions β and γ . At region α the jet is oriented at about 2° from the image azimuth; from equation 10, assuming a 1 m/s core velocity for the jet, MTF_v produces ~ 1.7 m or $\sim 1/3$ pixel widths of smearing due to the along-jet velocity. For a jet of the same core velocity, at the $\sim 12^\circ$ angle of the profiles at regions β and γ , MTF_v produces ~ 10 m or ~ 2 pixel widths of smearing due to along-jet velocity. In contrast, for a jet with a 1 m/s core velocity flowing in the range direction for the same 10 km imaging distance, MTF_v would produce ~ 50 m or ~ 8 pixel widths of smearing.

The profile for region α is nearly parallel to the azimuth, and as discussed above, this orientation should result in negligible velocity effects. The cost of this orientation in terms of interpretation of image profiles is the potential range dependent normalization (image intensity) bias introduced by the incident angle dependent imaging mechanism, the instrument itself, or subsequent processing, so for any structures observed in such an orientation, an attempt should be made to confirm their existence at more significant imaging angles, as has been done here for regions β and γ .

CHAPTER 7

CONCLUSIONS

Correlation between SAR imaged structures and thermal fronts in the 1989 Cape Mendicino filament was found to be high. Geostrophic jets visible in AIRSAR images were confined to the thermal boundaries of mesoscale filament structures, and the associated convergent fronts acted to concentrate surfactants. Regular periodic structures associated with thermal fronts, or integrated with bright linear SAR features, were common; some at a scale implying internal waves, some small enough to suggest vertical circulations and secondary flows. The SAR signature of instability vortices was apparent and contained fine structures with periodic features embedded.

The SAR images of a roughly symmetric jet of width ~ 1 km within the southern branch of the filament imply convergence-driven concentration of surfactants. In some segments, the modulus of elasticity appears to exceed historically reported values. A significant hump in the SAR profile to the windward side of the peak was ubiquitous and suggests that either critical reflection was occurring and giving rise to the SAR signal through intermediate wave-induced modulation of the Bragg waves, or that the jet had a persistent and complex velocity profile.

Comparison of jet profiles to a simple model suggests either a net along-jet velocity change across the jet, significant convergence, significant cross-spectral energy transfer away from P band λ_{Bragg} , critical reflection of waves near P band λ_{Bragg} (which would

further imply a jet core velocity exceeding ~ 2 m/s), or critical reflection of a significant intermediate wave component.

SAR image derived spectra show, in addition to the wind swell, a signal whose wavenumber and direction are consistent with the width and direction of the swell peak, and thus suggestive of infra-gravity waves.

An attempt was made to explain some of the angle dependence of the images in terms of geophysical processes; since instrument effects important to these interpretations have not been quantified, these results are presented in appendix B.

In considering future surveys of this type, clearly in-situ surface measurements of velocity and surfactant concentration (with particular vigilance for evidence of anomalously high levels of elastic modulus) across the jet would be useful in the interpretation. In-situ surface wave spectrum measurements might also seem helpful, but one would first have to develop a technique and instrumentation. Any method, other than an electromagnetic technique over distances that would qualify it as remote sensing, will likely be prone to ship hull produced artifacts. Still, the usefulness of the comparisons between the simulation results and the actual jet profiles was severely limited by lack of information about the real surface directional wave spectra. It appears that future airborne SAR investigations would benefit from the addition of spectrum sampling runs, utilizing circular flights at strategic (e. g. relatively SAR featureless) locations, near the jet, where the same radar hardware (but a different algorithm) would be used to provide a direct measurement of the directional spectra. The algorithm seemingly could be developed without much difficulty, the problem being of complexity similar to that of the imaging

problem. Due to the wide look angle range of the instrument the wavenumber coverage could be made nearly gap free over a range of a few centimeters to over a meter. Waves longer than this need to be considered because of the intermediate wave contribution, but those measurements, at least could be made from the surface using conventional inertia sensing wave-rider buoys.

APPENDIX A

A NUMERICAL SIMULATION OF JET INDUCED WAVE FIELD MODULATION

AND THE PREDICTED SAR SIGNATURE

Numerical simulations of the modulation, across a jet, of the O(Bragg wavelength) wave fields, were run, and the "predicted" SAR image intensity profiles were extracted. Only two theories, the equilibrium wind wave spectrum theory of Pierson and Moskowitz (1964), and the wave/current interaction theory of Longuet-Higgins and Stewart (1960), were included in the model.

We showed in chapter 6, using equation 10, that the segments of the jet with a nearly azimuthal orientation are imaged with insignificant contribution from MTF_v ; this allows a legitimate comparison of this data to a simplified simulation considering only the MTF_h component of SAR imaging process.

The simulation does not incorporate the higher order processes of long and intermediate scale gravity waves whose effect on a SAR image comes through (1) the modulation of the wave field in the neighborhood of λ_{Bragg} by the intermediate scale waves which have been modulated directly by the current, and (2) the effect on surface tilt and consequential shift in which components of the surface spectrum correspond to λ_{Bragg} .

Lyzenga (1998) found through the use of similar but more complicated simulations

that the contribution of intermediate waves through the first of the above processes, referred to generally as second order modulation, to be most significant for small Bragg wavelengths, with X and C bands being strongly affected, and L band being only weakly affected. Thus, while the deviations in the results of our simulations for P band due to second-order modulation can safely be considered negligible, results for L band are expected to have minor deviations, and results for C band should be suspected of significant deviations. From figures 8 and 9 in Lyzenga 1998, one can confirm the expectation that these deviations are most pronounced toward the lee of the jet.

A jet with a defined time independent velocity profile is treated as a one dimensional structure, i. e. straight with no along-jet flow variation. A wave field is defined for all angles leeward of the jet.

Currents of up to O(1 m/s) are typical in the cores of strong jets in this region. Huyer, et al. (1987) measured a velocity of ~0.5 m/s for the 1981 Point Arena filament in a survey utilizing acoustic Doppler current measurements; Davis (1985) measured a surface current of 0.55 m/s with a surface drifter (1 m depth) in the same filament. Flament and Armi (2000) calculated a surface geostrophic velocity peak of ~1.2 m/s in the Point Arena filament in 1985. Huyer et al. (1991) measured a current of ~0.8 m/s (at 21 m depth) in an ADCP profile of the 1988 Point Arena filament.

After Pierce et al., 1991 we assume the flow field of the jet to be Gaussian in shape:

$$U = U_o e^{\frac{-(y - y_{center})^2}{L^2}} \quad (A1)$$

where U_o is the jet velocity maximum, y_o is the position of the center of the jet and

L is the Gaussian length scale. A value of $U_0 = 1$ m/s was used in these simulations. The simulation includes no net velocity change across the jet.

Each component of the wave field, defined on a fine grid, is modulated by angle, wavenumber, and energy, for the given change in velocity, according to Longuet-Higgins and Stewart's (1960) current-wave interaction model, equations A4-A7, at subsequent positions across the jet. To reduce numerical noise, the new wave field is determined by binning to a course grid of $1/4$ the component density. This field is then interpolated bilinearly once to restore the higher density field used for the next cross-jet segment of the iteration. All simulations were run on a course grid of 32 angles, 32 wavenumbers, and 21 positions within the hypothetical jet. The angle range covered the 180° region upwind of the jet, the wavenumber range being from $1/2 k_{\text{Bragg}}$ to $3/2 k_{\text{Bragg}}$. In the extraction of the "predicted" SAR response, only the first order Bragg component was considered and the MTF was taken to be linear.

The wave field theory proposed by Pierson and Moskowitz (1964), is an idealized empirical description based on similarity theory, i. e. an attempt through conversion to dimensionless variables, to find a scale-independent theory of equilibrium wave spectra consistent with observations. The resulting theoretical spectrum, commonly referred to as the P-M spectrum, equation A2, describes well most subsequent observations of fully developed seas and thus continues to be a common reference point for most research involving wind wave spectra.⁴

⁴ The first proposed use of a spectrum of the form now referred to as a PM spectrum, utilizing the Phillips saturation spectrum (1958) with an exponential high pass, was by Roll and Fischer (1956).

$$F(\omega) = \alpha g^2 \omega^{-5} e^{-\frac{5}{4}(\frac{\omega}{\omega_p})^{-x}} \quad (\text{A2})$$

This spectrum peaks at $\omega = \omega_p$ where ω_p is the angular frequency of waves with phase velocity equal to the surface wind speed, below which there can be no direct transfer of momentum from the wind field to the wave field.

The ω^{-5} factor is called the Phillips saturation spectrum and appears universal for super-capillary wind waves in fully developed wind seas. Spectra more blue than this are not stable at typical ocean energy levels ($u_* > \sim 1$ m/s) due to slope spectrum constraints, i. e. the onset wave breaking (Phillips, 1958). Spectra more red than this seem less likely considering the enhanced wind/sea momentum transfer at the lower phase velocities of smaller waves. The exponential term acts as a high pass filter, expected here since, again, once the phase velocity of a given component of the wave spectrum exceeds the wind speed at the surface, no momentum can be directly transferred from the wind field to that wave component.

Energy can reach lower frequency wave components only indirectly through the nonlinear transfer processes of non-resonant cubic interaction and resonant coupling (quartic and higher terms dominating at the super-capillary scale) as described in detail by Hasselmann, Janssen, and Komen, in Komen, et al. (1994). Given the faster group velocity, and thus inherent non-local nature, of the spectra of longer waves, this region of the spectrum, while likely on average blue (i. e. decreasing in energy with wavelength), probably exhibits a large variability. The measured values of the exponent of ω/ω_p in the literature thus vary depending on conditions from between ~ 1 to ~ 5 , presumably, lower

values describing older seas, as there has been more opportunity for spectral transfer.

A value of 4 is commonly used in the literature as descriptive of typical seas, and was used in these simulations. With regard to the simulations, further justification is superfluous as we are concerned with frequencies in the neighborhood of ω_{Bragg} which lie on the high frequency side of the spectral peak where the ω^{-5} term dominates.

No general theory is currently accepted as descriptive of the angular fall-off of spectral energy away from the wind direction, even assuming a steady wind field. After Donelan, in Komen, G. J., et al. (1994), we used a sech^2 falloff in our simulation. The exact form of the angular dependence was

$$F(\omega, \theta) = \frac{1}{2} F(\omega) \beta \text{sech}^2(\beta(\theta_{\text{wind}} - \theta)) \quad (\text{A3})$$

where Donelan found $\beta=1.24$ to hold for the regime of $\omega/\omega_p > 1.6$, followed by a narrowing of the angular distribution as ω continues to increase. All our simulations were run with the value of $\beta=1.24$. Compliance with the frequency ratio condition requires an associated minimum surface wind speed of $v_{\text{wind}} = g/\omega_p > 0.4 \text{ m/s}$, 0.9 m/s , and 1.5 m/s for C, L, and P bands, respectively.

The theory of Longuet-Higgins and Stewart (1960) includes contributions to the wave amplitude from the radiation stress term and thus differs from ray theory in that energy is exchanged between the current and wave fields. It must be noted that the theory of Longuet-Higgins and Stewart describes the modulation of a monochromatic field, whereas we have already specified a continuum spectrum. Whether the presence of

polychromatic and continuous spectrum compromises, the application of this theory will require a more detailed study of the theory's derivation than has been done here.

The equations describing this modulation of a wave component in a shear field with no convergence are not integral, that is, the change in wavenumber, wave-speed, angle, and amplitude are determined solely by the initial wave number, angle of incidence, and local velocity of the jet with respect to background ($v=0$). The simulation was none the less performed iteratively to account for any reflected component of the spectra, as discussed below.

At any position within the jet, the modulated values of these quantities are given by:

$$\frac{k}{k_o} = \left(1 - \frac{V}{c_o} \sin \theta_o\right)^2 \quad (\text{A4})$$

$$\sin \theta = \frac{\sin \theta_o}{\left(1 - \frac{V}{c_o} \sin \theta_o\right)^2} \quad (\text{A5})$$

$$\frac{F}{F_o} = \frac{\sin (2 \theta_o)}{\sin (2 \theta)} \quad (\text{A6})$$

which are valid for

$$\frac{V}{c_o} \leq \frac{1 - \sqrt{\sin \theta_o}}{\sin \theta_o} \quad (\text{A7})$$

The relevant geometry is shown in figure A1. For $V/c_o > (1 - \sqrt{\sin \theta_o}) / \sin \theta_o$ total reflection occurs and that component of the wave field is turned back.

Whether wave reflection in the jet occurs coherently or incoherently would depend on the scale of current variations in the jet relative to the wavelength of the reflected wave.

At the scale of wavelengths in the neighborhood of λ_{Bragg} , current variations would be small and thus coherent reflection is expected. The matter is now complicated because wave groups traveling in different directions (and of relevance here, opposite directions) will have zero phase correlation at even minute spatial scale. The statistical quantities governing speckle noise and mean radar backscatter now include this backward propagating component and the imaging process must be re-evaluated.

Incoherent reflection and the partial destructive interference of the reflected components would reduce the magnitude of the reflected wave field but not eliminate its relevance. Thus incoherent reflection is to be distinguished from the exclusion of reflection. The relevant spatial scales of the reflection process, presumably stochastic due to an assumed along-jet and cross-jet variance in the velocity field, might even be distinguishable through the statistical characteristics of SAR signal about the jet.

In addition, inclusion of reflection would require another layer to the simulation; namely wave components moving in both directions through the jet. Components of the wave field from the lee of the jet and the reflected components would be then added to the wave components from upwind of the jet to get the net spectral energy density. The complete simulated wave field would have to be determined by incremental modulation twice across the jet, first from the windward side to the leeward side, and then back from the leeward side to the windward side of the jet. The SAR response would then be derived from the sum of the spectral energy at angles 0° and 180° from the SAR look direction.

Ignoring these complications is inherently unsatisfying, but inclusion is beyond the scope of this investigation. In the spirit of the "simplest model", reflection is excluded from the simulation and evidence for its occurrence in the SAR images will be looked for in deviations from the simulation results.

In addition to the effects of intermediate scale waves, also neglected were the contributions to the radar backscatter from Bragg components higher than order one, including the evolution of the wave field due to the cross-spectral transfer that is expected to take place within regions of strong wave-field modulation and thus relatively high wave amplitude, the wave damping due to potential current shear generated turbulence, wave breaking and breaking generated turbulence induced damping, and the accumulation of surfactants and microlayer induced damping.

The results of nine simulation runs, one for each radar band for a geometry analogous to each of the regions α , β , and γ (figure 40), assuming a northerly peaked sech^2 wind wave field and a southeastward flowing Gaussian jet, are presented in figures A2-A10. SAR response is inferred from the wave field amplitude at the Bragg wavelength and the angle corresponding to the SAR azimuth, as indicated by the black circles in the spectrum plots.

We can see that the effect on the wave field due to reflection occurs about the boundaries of our simulated wave space. For cyclonic shear the wave field is negated near the right hand boundary of the simulated wave spectra, and for anticyclonic shear the negation occurs near the left hand boundary. The part of the wave field affected by reflection changes sides after passing the velocity maximum of the jet. The maximum

wavelength (minimum wave number) for which reflection occurs, for a given angle, can be seen in these plots. The effect of vacuation, due to refraction away from the wave space boundaries, as we assumed no waves propagating from the lee of the jet, is likewise seen about the boundaries of the simulated wave space. In this case, for cyclonic shear the wave field is negated near the left hand boundary of the simulated wave spectra, and for anticyclonic shear the negation occurs near the right hand boundary, opposite that of the case for reflection. Again, the part of the wave field affected by reflection changes sides after passing the velocity maximum of the jet. The central part of the simulated wave space, containing the position corresponding to λ_{Bragg} , is isolated from these effects. Thus, the geometry of the problem, in addition to negating the velocity bunching contribution to the SAR image, also legitimizes the application of a simulation neglecting reflection and the wave components propagating from the opposite side of the jet, to the modeling of a SAR imaged jet profile.

The presence of a minima to the lee of the maxima in C and P bands, and the absence of a minimum in the intermediate wavelength L band, for the region α simulation, is indicative of the non-scaleable nature of the simulation. The competing effects of simulated refraction, wavenumber modulation, and amplification imply at least a cubic complexity in band dependence and give rise to this unexpected result.

The negative modulation results of the simulation for region γ suggest that the input wave field may deviate strongly from the unidirectional peaked form simulated here.

For angular wave distributions of narrower than $\sim \text{sech}^3\theta$ simulation results

corresponding to region α begin to deviate significantly from the data, having a pronounced minimum windward of the peak. The simulations corresponding to region β were not as sensitive to this narrowing and produced results relatively indistinguishable in form for angular distributions as narrow as $\text{sech}^4\theta$. For wider angular wave distributions, even as extreme as having no angle dependence, simulation results for both regions α and β remained relatively consistent with the $\text{sech}^2\theta$ results. Results of simulations corresponding to region γ exhibit a gradual dependence on angular wave distribution with a wider distribution, again out to no angle dependence, but remain inconsistent with the data.

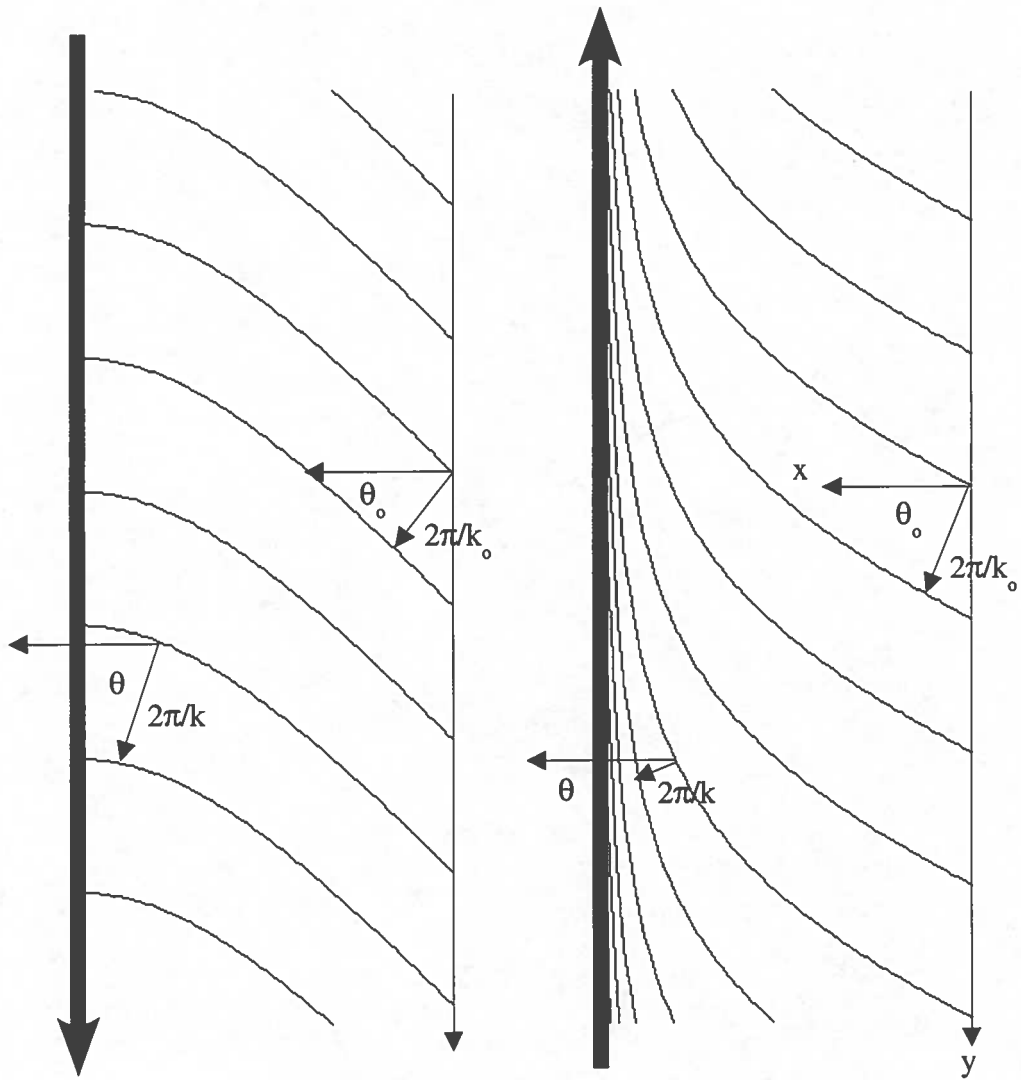


Figure A1. Wave modulation geometry for equations A4 through A7. The large arrow represents the jet velocity.

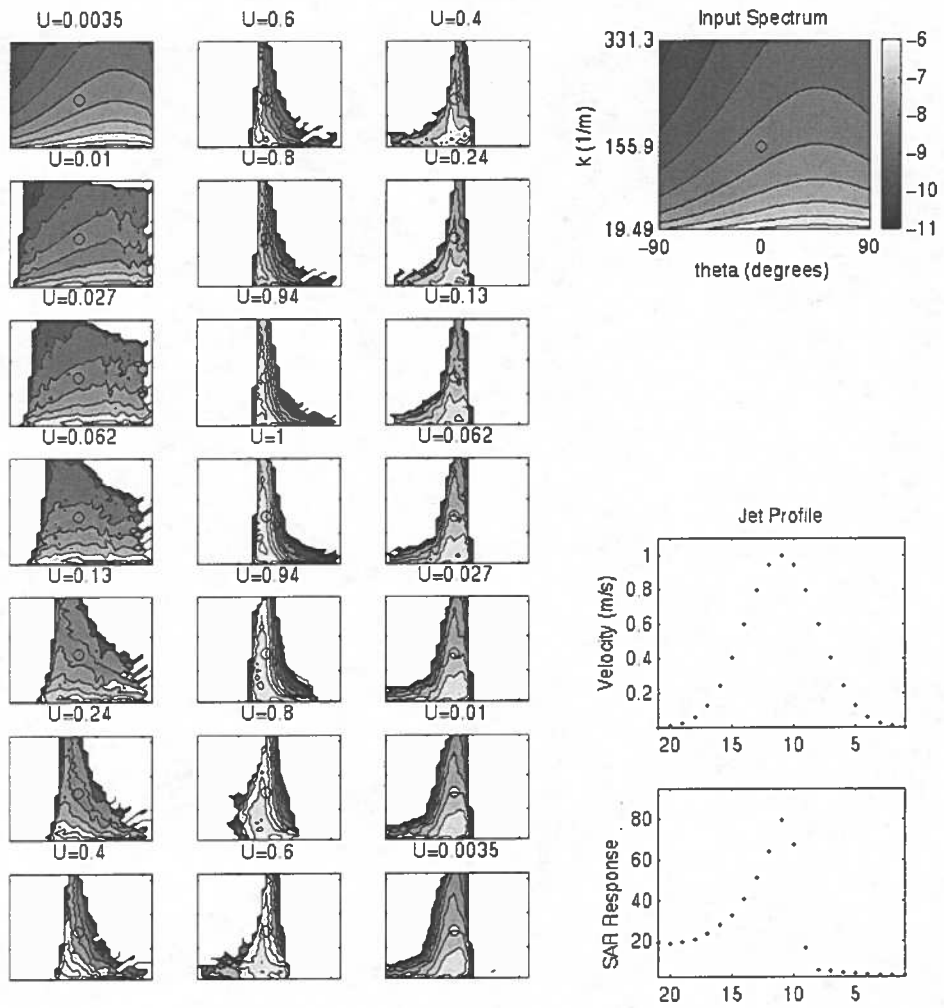


Figure A2. Simulation results for region α / C band.

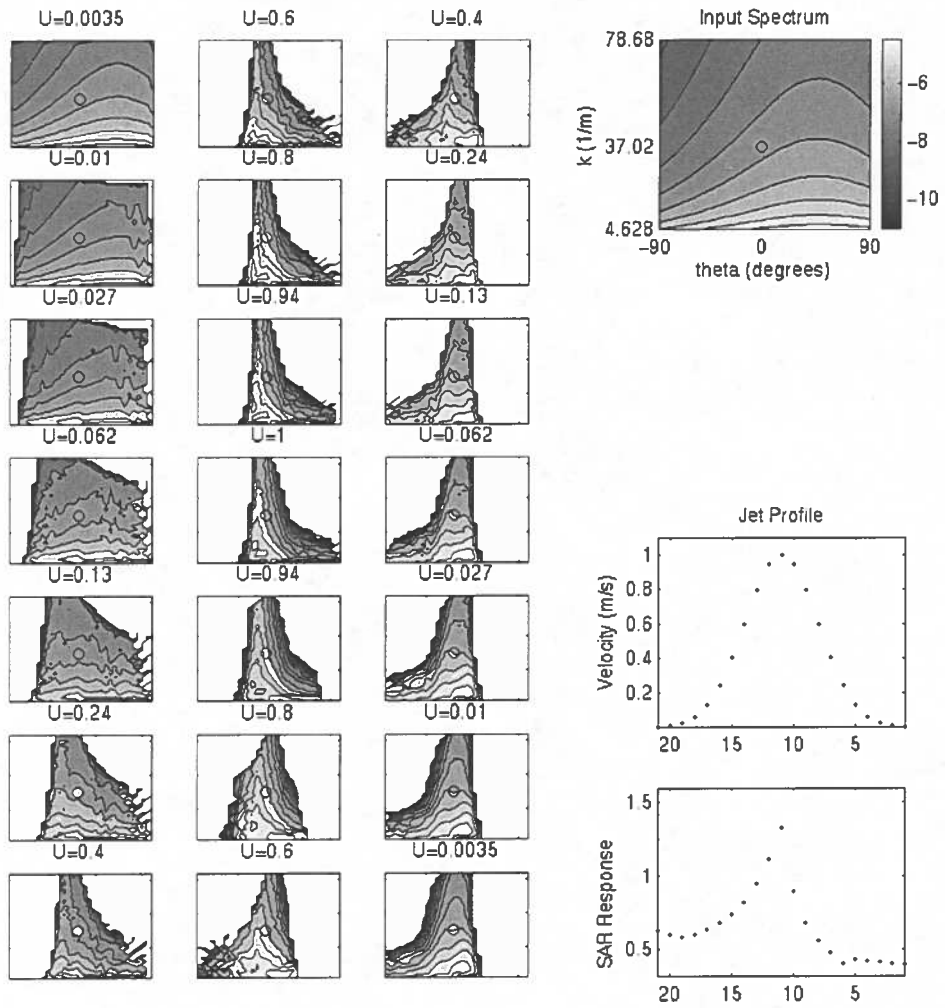


Figure A3. Simulation results for region α / L band.

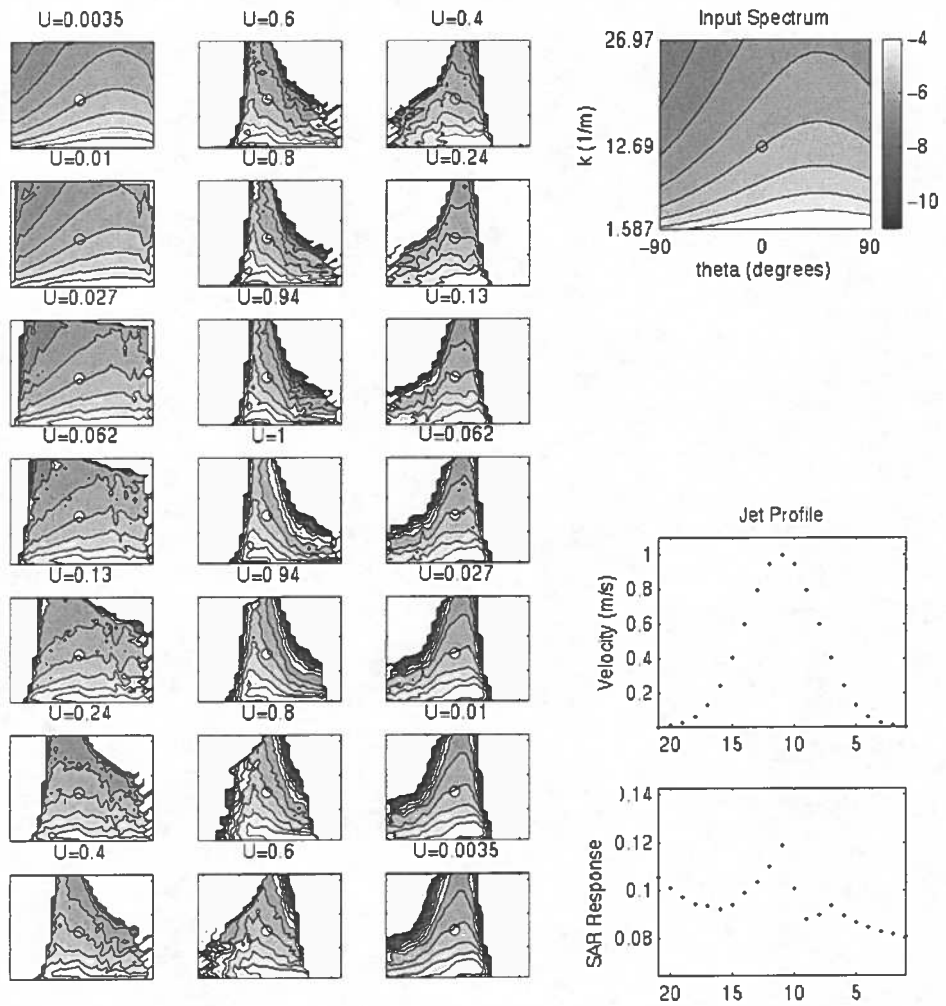


Figure A4. Simulation results for region α / P band.

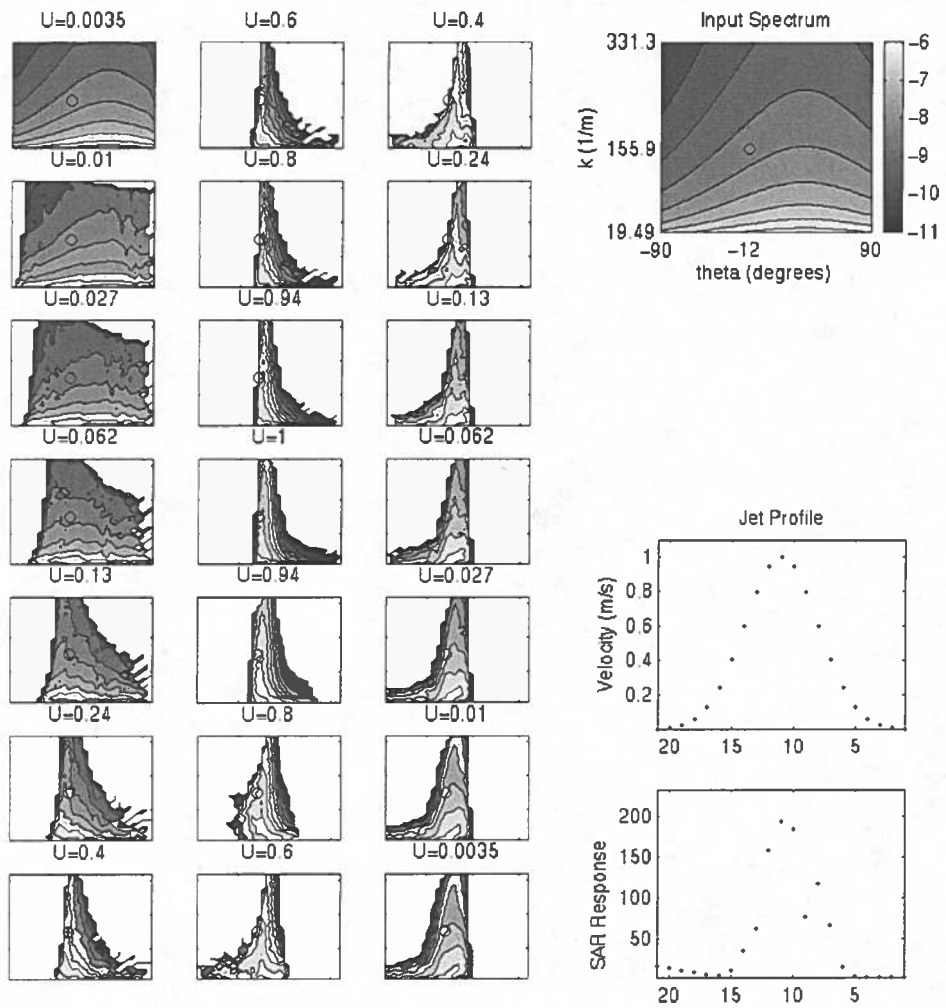


Figure A5. Simulation results for region β / C band.

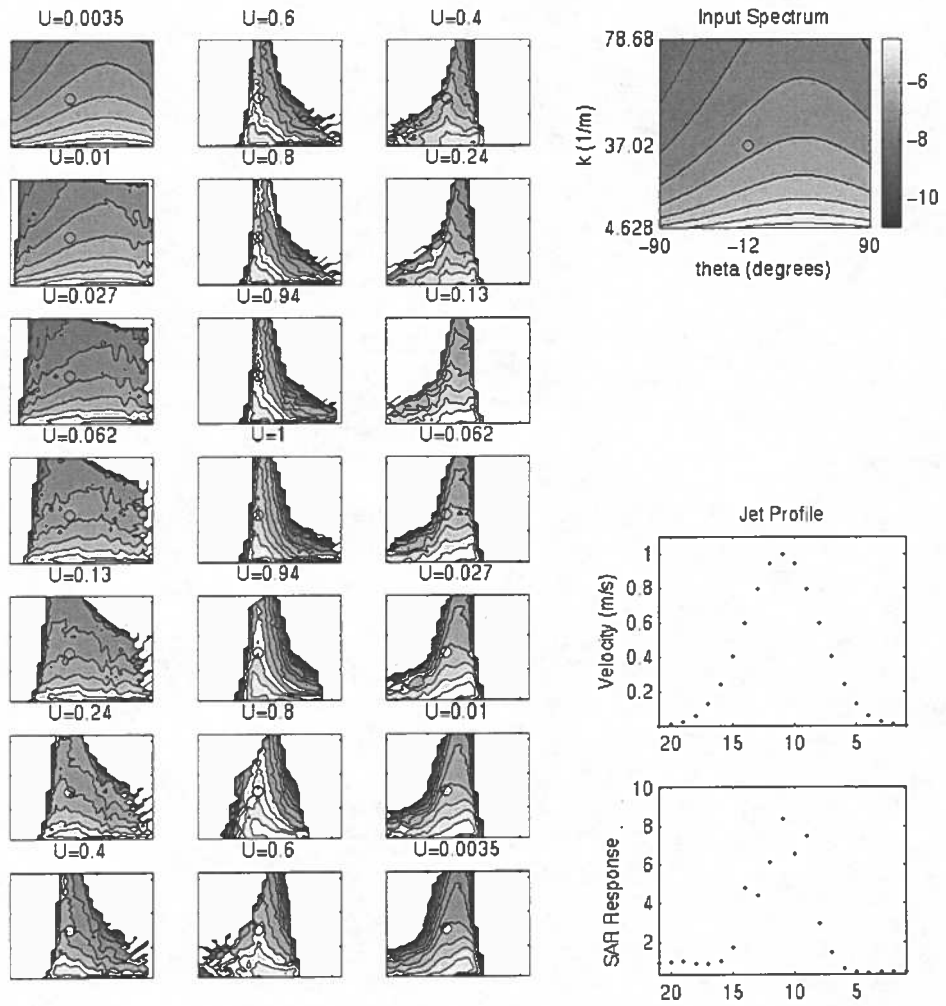


Figure A6. Simulation results for region β / L band.

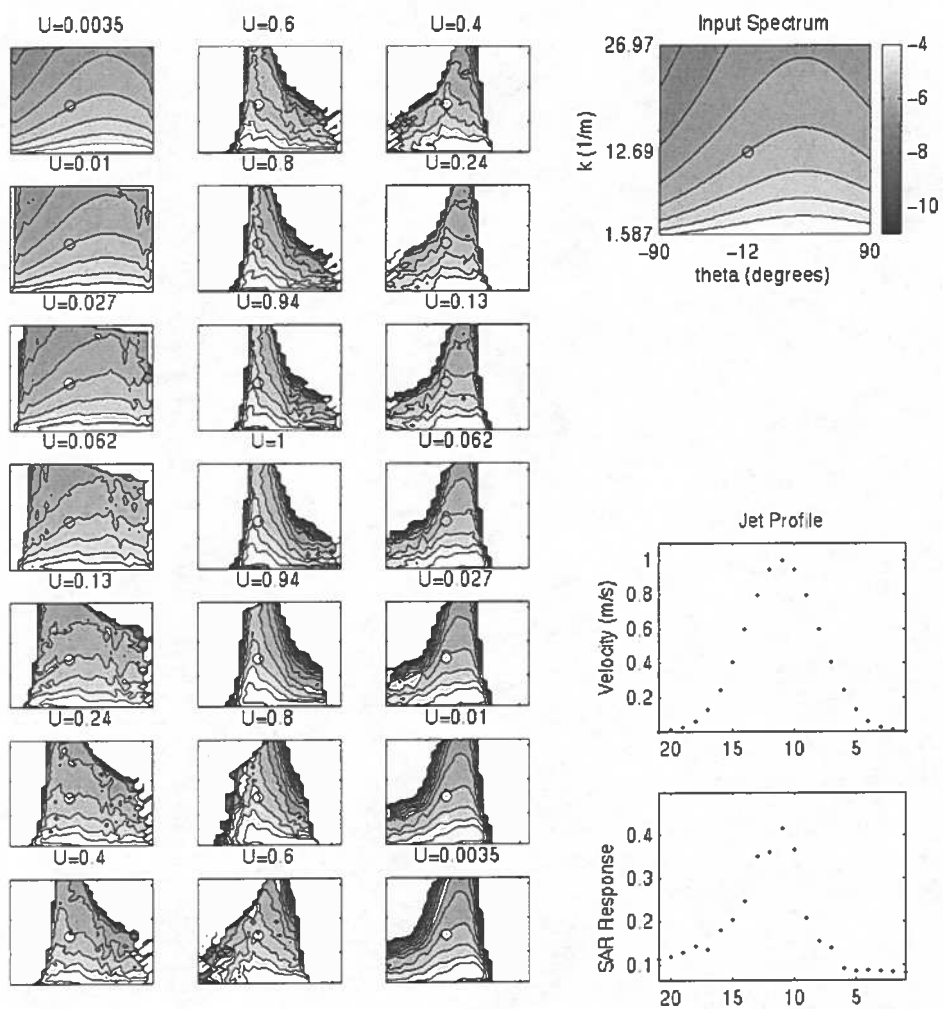


Figure A7. Simulation results for region β / P band.

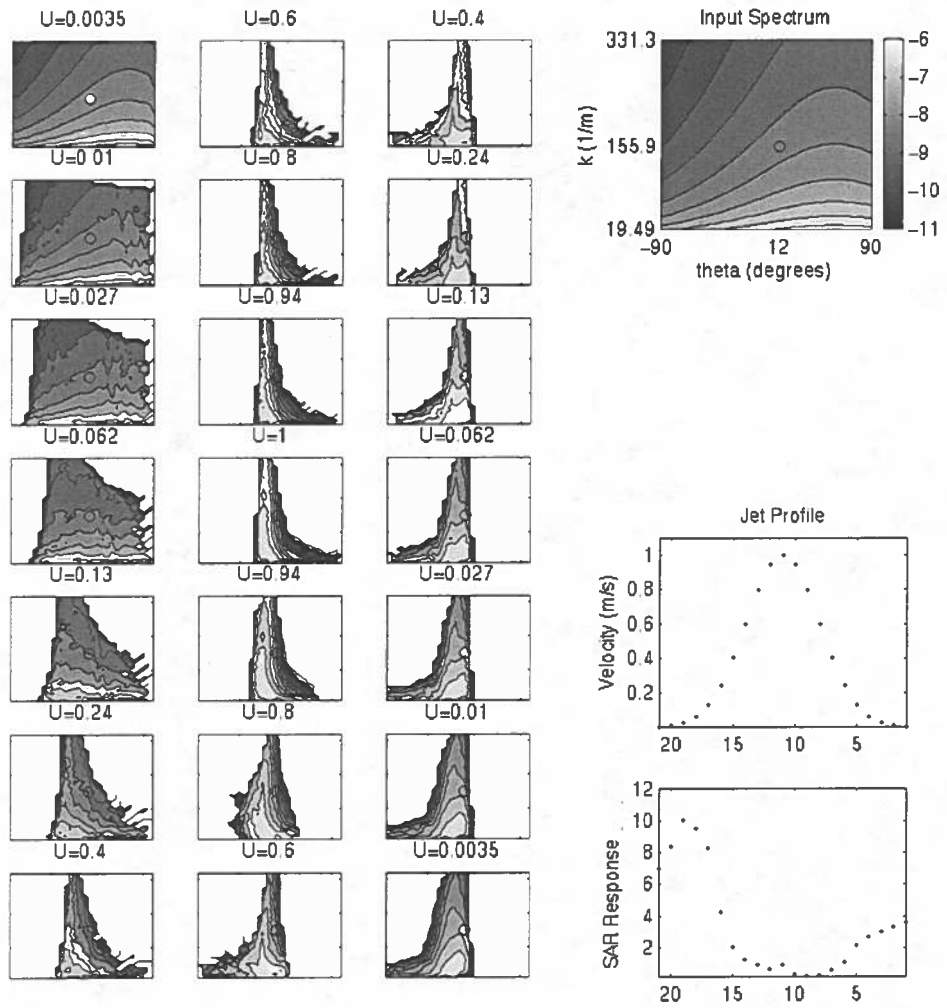


Figure A8. Simulation results for region γ / C band.

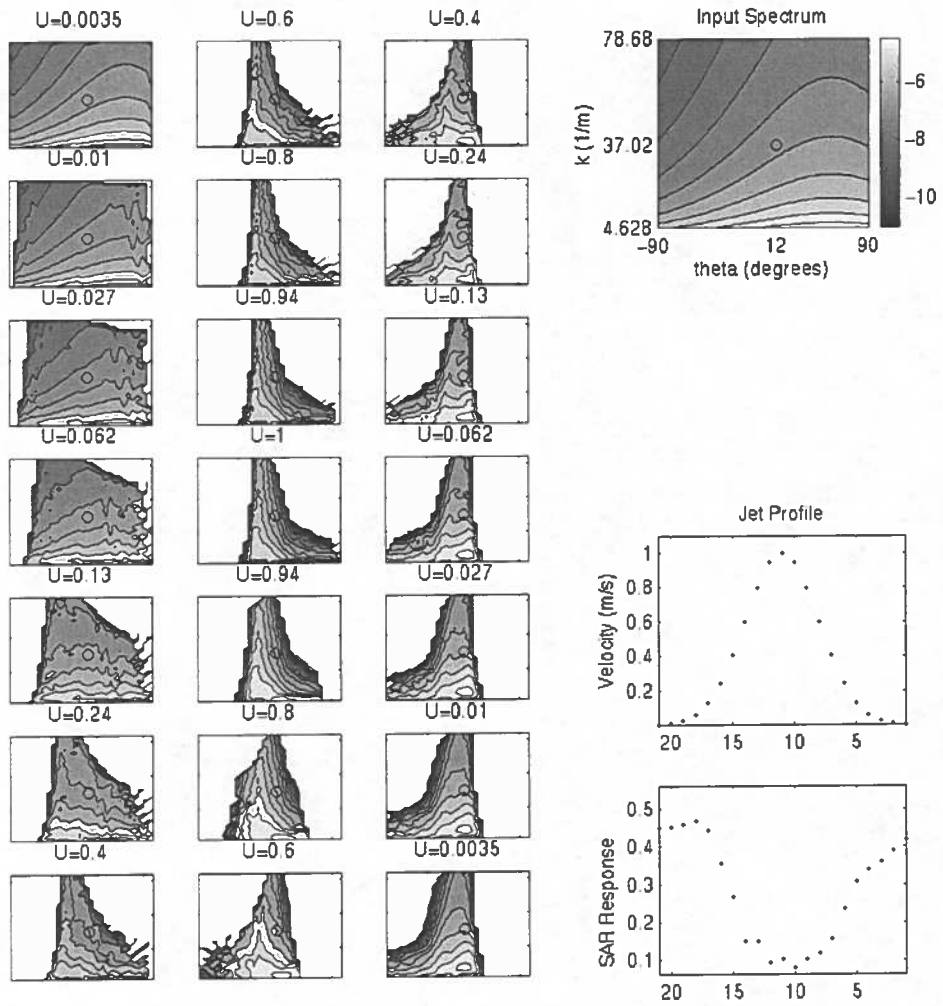


Figure A9. Simulation results for region γ/L band.

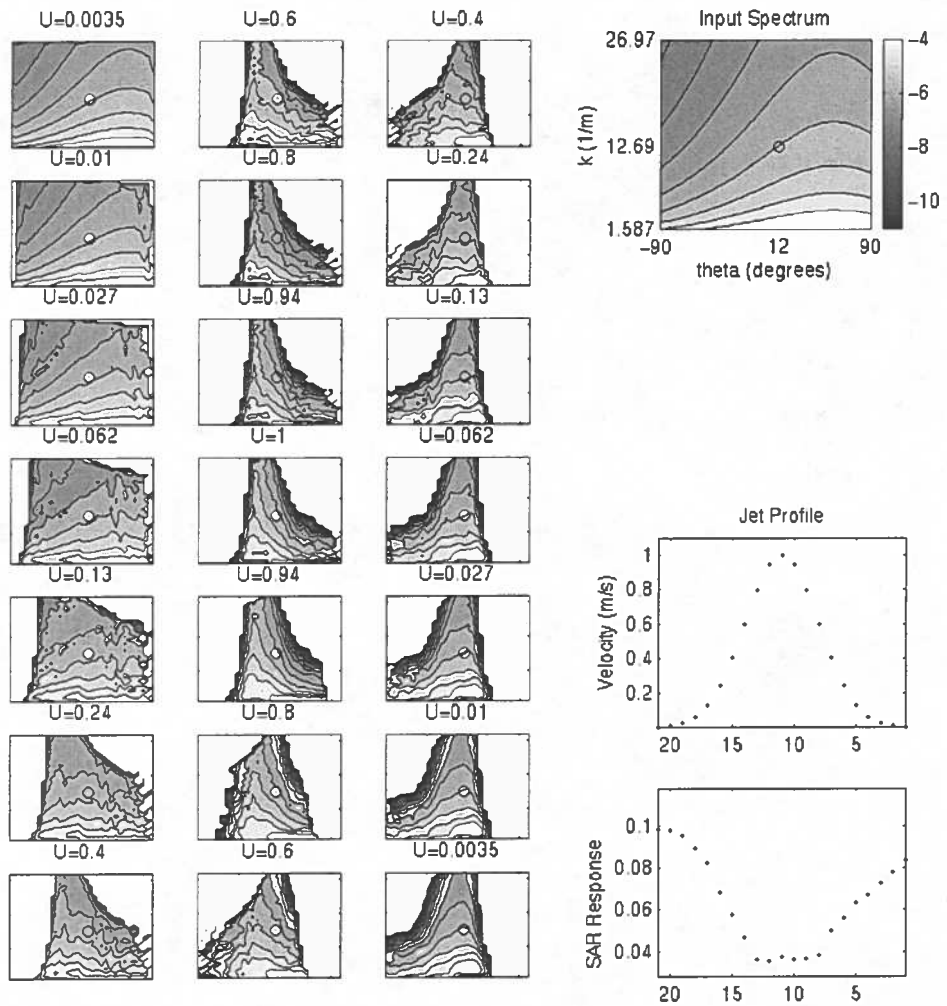


Figure A10. Simulation results for region γ / P band.

APPENDIX B

SUBRESOLUTION INFERENCES

Two classes of geophysical information can be inferred from this type of SAR data set: the imaged processes of the type discussed in the bulk of this thesis, whose scales are larger than the pixel resolution, and subresolution processes (the validity of which depends on the non-dominance of the gain control characteristics of the SAR instrument, which has yet to be accessed for this case), derived from the incidence angle dependent characteristics of the images.

Of the second class of processes, several wave and current properties are implied by the loss of ocean features toward the far range of the C band images:

(1) The lack of signal response to structures clearly imaged in the longer wavelength bands indicates a surface wave spectrum which is not being affected by those structures through the direct or intermediate wave hydrodynamic modulation assumed to be responsible for much of the signal in the other bands. Assuming that this is not an instrument effect (the amplitude recorded by the instrument actually begins to increase near the end of the far range while the speckle signal remains nearly constant) this implies a surface wave spectrum which is being held at saturation at the far range C band Bragg wavelength (~4 cm), presumably via a wind to wave energy source, and a wave to wave and wave to turbulence energy sink.

(2) Furthermore, given (1), the lack of a velocity bunching signal, which is

independent of the Bragg wavelength, indicates that MTF_v did not make a significant contribution to the overall MTF for any of the structures imaged in this survey; furthermore, from equation 10 this implies a surface current field where the magnitude of shear and convergence (at least in the range direction) did not exceed $\sim 0.01 \text{ s}^{-1}$. For comparison, the historical $\sim 1 \text{ m/s}$ core velocity of filament associated jets and the SAR data inferred $\sim 300 \text{ m}$ half-width of the suspected jet within the southern branch, the vorticity of this structure would be $\sim 0.003 \text{ s}^{-1}$. Note that this does nothing to negate the fact that a $\sim 1 \text{ m/s}$ jet aligned with the range direction would result in a 85 m , or 14 pixel, displacement of the signature of the jet core, it simply demonstrates that unless the shear within the jet is highly localized, that there will be no abrupt changes in azimuthal displacement; loss of signal due to a small azimuthal displacements of the expected surface patch will also be compensated by the signal from the adjacent patches, the result being no net signal.

(3) Finally, the spectrum at the far range C band Bragg wavelength appears to be flat (rather proportional to the inverse of the radar scattering dependence on wavelength) to the extent that tilt modulation, often assumed to be important in the imaging of swell (e. g. Melsheimer et al, 1998), fails to give rise to a signal at this swell amplitude. In addition, the lack of a range bunching signal naturally results from a surface of unprodigious amplitude. Taken together with result (2), this implies that for this data set $MTF \approx MTF_h$, all other components are negligible.

Also of the second class of processes, the lack of a significant reduction in speckle

noise toward the near range of the P band images implies a spatially white spectrum at the near range P band Bragg wavelength (~ 1.2 m) over an area defined by the imaging resolution of the instrument (probably $\sim 15.2 \times 7.5$ m²). In other words, at this wavelength (and similarly for all Bragg wavelengths covered by this instrument, nearly continuous from 3 cm to 1.2 m) the surface wave spectra are smooth (featureless) at a wavelength resolution corresponding to the radar bandwidth, and there is no correlation of phases (coherence). I emphasize the long wavelength limit for which this appears to be true, as, though seemingly obvious for the shortest wavelengths where the ratio of the spatial resolution length scale to the Bragg wavelength is ~ 500 , this same ratio is only ~ 10 for the near range P band Bragg waves, and phase correlation might be expected.

REFERENCES

- Abbot, M. R. and Barksdale, B., Phytoplankton pigment patterns and wind forcing off central California, *J. Geophys. Res.*, 96, 14,649-14,667, 1991.
- Allen, J. S., et al., Dynamics of the coastal transition zone jet, 2, Nonlinear finite amplitude behavior, *J. Geophys. Res.*, 96, 14,995-15,016, 1991.
- Beardsley, R. C., et al., Local atmospheric forcing during the Coastal Ocean Dynamics Experiment, Part 1. A description of the marine boundary layer and atmospheric conditions over a northern California upwelling region, *J. Geophys. Res.*, 92, 1467-1488, 1987.
- Davis, R. E., Drifter observations of coastal surface currents during CODE: the method and descriptive view, *J. Geophys. Res.*, 90, 4741-4755, 1985.
- Flament, P., et al. Evolving structure of an upwelling filament, *J. Geophys. Res.*, 90, No. C6, 11,765-11,778, 1985.
- Flament, P., and Armi, L., The shear, convergence, and thermohaline structure of a front. *J. Phys. Ocn.*, 30, 51-66, 2000.
- Frew, N. M., and Nelson, R. K., Isolation of marine microlayer film surfactants for ex situ study of the surface physical and chemical properties, *J. Geophys. Res.*, 97, 5281-5290, 1992.
- Fu, L., and Holt, B., Seasat views oceans and sea ice with synthetic-aperture radar, JPL Publication 81-120, 1982.

- Haidvogel, D. B., et al., Dynamical simulations of a filament formation and evolution in the coastal transition zone, *J. Geophys. Res.*, 96, 15,017-15,040, 1991.
- Hasselmann, K., et al., Theory of synthetic aperture radar ocean imaging: a MARZEN view, *J. Geophys. Res.*, 90, 4659-4686, 1985.
- Huyer A., Hydrographic observations along the CODE central line off northern California, *J. Phys. Ocn.*, 14, 1647-1658, 1984.
- Huyer A., et al., Currents and water masses of the coastal transition zone off northern California, June to august 1988, *J. Geophys. Res.*, 96, 14809-14831, 1991.
- Korso, P. M. and Huyer, A., CTD and velocity surveys of seaward jets off northern California, July 1981 and 1982. *J. Geophys. Res.*, 91, 7680-7690, 1986.
- Komen, G. J., et al., Dynamics and modeling of ocean waves, Cambridge University Press, 1994.
- Lapeyre, G. et al., Does the tracer gradient vector align with the strain eigenvectors in 2D turbulence?, *Physics of Fluids*, 11, 3729-3737, December 1999.
- Longuet-Higgins, M. S., and R. W. Stewart, Short gravity waves on non-uniform currents, *Fluid Mech.*, 10, 529-549, 1960.
- Lucassen, J., Effect of surface-active material on the damping of gravity waves: a reappraisal, *Journal of Colloid and Interface Science*, Vol.85, No.1, Jan 1982.
- Lyzenga, D. R., Effects of intermediate-scale waves on radar signatures of ocean fronts and internal waves, *J. Geophys. Res.*, 103, 18,759-18,768, 1998.

- Mass, J. T., and Milgram, J. H., Dynamic behavior of natural sea surfactant films, *J. Geophys. Res.*, 103, 15695-15715, 1998.
- Melcheimer, C., et al., Imaging of ocean waves on both sides of an atmospheric front by the SIR-C/X-SAR multifrequency synthetic aperture radar, *J. Geophys. Res.*, 103, 18839-18849, 1998[1].
- Pierce, S. D, et al., Dynamics of the coastal transition zone jet 1. Linear stability analysis, *J. Geophys. Res.*, 96, 14979-14993, 1991.
- Pierson, W. J. and Moskowitz, L., A proposed spectral form for fully developed wind seas based on the similarity theory of S. A. Kitaigorodskii, *J. Geophys. Res.* 69, 5181-5190, 1964.
- Ramp S. R., et al., The physical structure of cold filaments near Point Arena, California, during June 1987, *J. Geophys. Res.*, 96, 14,859-14,883, 1991.
- Strub, T., et al., The nature of the cold filaments in the California current system, *J. Geophys. Res.*, 96, 14,743-14,768, 1991.
- Wei, Yi and Wu, Jin, In situ measurements of surface tension, wave damping, and wind properties modified by natural films, *J. Geophys. Res.*, 97, 5307-5313, 1992.
- Winant, C. D., et al., The marine layer off northern California: an example of supercritical channel flow, *J. Atm. Sci.*, 45, 1988.